Title

Study of the Electrochemical System of Antimony-Tellurium in Dimethyl Sulfoxide for Growth of Nanowire Arrays, and an Innovative Method for Single Nanowire Measurements

Author

Kalisman, Philip Taubman

Publication Date

2012

Study of the Electrochemical System of Antimony-Tellurium in Dimethyl Sulfoxide for Growth of Nanowire Arrays, and an Innovative Method for Single Nanowire Measurements

by

Philip Taubman Kalisman

A dissertation submitted in partial satisfaction of the

requirements for the degree of

Doctor in Philosophy

in

Chemistry

in the

Graduate Division

of the

University of California, Berkeley

Committee in charge:

Professor Angelica M. Stacy, chair
Professor Alexander Pines
Professer Rachel Segalman

Fall 2012

Study of the Electrochemical System of Antimony-Tellurium in Dimethyl Sulfoxide for Growth of Nanowire Arrays, and an Innovative Method for Single Nanowire Measurements

by Philip Taubman Kalisman

Abstract

Study of the Electrochemical System of Antimony-Tellurium in Dimethyl Sulfoxide for Growth of Nanowire Arrays, and an Innovative Method for Single Nanowire Measurements

by

Philip Taubman Kalisman

Doctor of Philosohphy in Chemistry

University of California, Berkeley

Professor Angelica M. Stacy, chair

There is a strong interest in thermoelectric materials for energy production and savings. The properties which are integral to thermoelectric performance are typically linked, typically changing one of these properties for the better will change another for the worse. The intertwined nature of these properties has limited bulk thermoelectrics to low efficiencies, which has curbed their use to only niche applications. There has been theoretical and experimental work which has shown that limiting these materials in one or more dimensions will result in deconvolution of properties. Nanowires of well established thermoelectrics should show impressively high performance.

Tellurium is attractive in many fields, including thermoelectrics. Nanowires of tellurium have been grown, but with limited success and with out the ability to dope the tellurium. Working on previous work with other systems, tellurium was studied in dimethyl sulfoxide (DMSO). The electrochemical system of tellurium was found to be quite different from its aqueous analog, but through comprehensive cyclic voltammetric study, all events were identified and explained. The binary antimony-tellurium system was also studied, as doping of tellurium is integral for many applications. Cyclic voltammograms of this system were studied, and the insight from these studies was used to grow nanowire arrays. Arrays of tellurium were grown and analysis showed that by using DMSO antimony doped tellurium nanowire arrays could be grown. Furthermore, analysis showed that the antimony doped tellurium interstitially, resulting in a n-type material.

Measurements were also performed on arrays and individual wires. Arrays of 1.15% antimony showed ZT of 0.092, with the low ZT attributed to poor contact methods. Although contacting was an obstacle towards measuring whole arrays, single wire measurements were also performed. Single wire measurements were done by a novel method which allows for easy reproducible measurements of wire properties. So far, this method has only been used to measure the properties of bismuth telluride, but can easily be adapted to any type of nanowire. Bismuth telluride nanowires were found to have electrical resistivities matching that of bulk ($\sim$1.4*$10^{-5}\Omega$-m), and thermal conductivities lower than bulk ($< 1\frac{W}{m-K}$).

Professor Angelica M. Stacy
Dissertation Committee Chair

Contents

List of Figures

List of Tables

Acknowledgements

Thank you first and foremost to my parents and fantastic brother, Jason. You have been a great support leading up to, and throughout my time at Berkeley. Without you I could not have gotten to where I am now. I love you all very much.

To my friends, specifically those whose middle names I know (EAM, MCZ, JHN), to the tallest one (LV) and the less tall ones (PL and PE), and to those in San Francisco (CDB). Thank you for the fun times - from Lost Coast to Summer Softball - you have all been a large part of my Berkeley experience.

Of course many thanks to my PI, Angy Stacy, who has been eternally supportive, and an invaluable resource. I also must thank current and past members of our group: Lynn Trahey for her mentorship; Lee Brogan, my year awesome comrade; Pete Hillman, the p-type to my n-type thermoelectric research; Jenn for her irreverent humour and cat-related stickers; Latisha Paw U, for keeping our group from devolving into a frat house; and to my second best cube-mate, Chris Snedigar.

And a special thanks to my wonderful partner in crime, Ph.D. to be, Hilary Bell Falb.

Chapter 1

Introduction

The state of energy production and usage is an undeniable problem today; energy production relying on fossil fuels needs to be replaced by greener non-polluting methods. Even in cases where these energy sources cannot be replaced, an increase in efficiency, in both production and usage, is paramount. Thermoelectrics offer one way of alleviating issues of both energy production and efficiency. Thermoelectrics can be used either as direct energy producers, as photothermoelectrics, or to increase the efficiency of other established methods, by curtailing low efficiency due to heat losses. Whether on a small or a large scale, thermoelectrics offer a robust, solid state approach for converting entropically difficult to deal with, thermal energy, into electrical energy, which is easy to use and transport. U.S. energy production results in losses of nearly 60%, most of which is from heat loss, as shown in figure 1.1; globally, over 15 TW of energy are lost annually in power generation[47]. Recovering even a small portion of this lost energy would be extremeley significant. Furthermore, cooling and refrigeration could be made more efficient, quieter, more robust and greener by converting to freon-free, compressor-free thermoelectric modules. Apart from these mainstream uses, the unique nature of thermoelectics makes them viable candidates for niche applications ranging from thermal cloaking devises to powering deepspace spacecrafts.

The main reason that all of this promising technology is not currently being utilized is the low efficiency of current thermoelectric devices. Research is needed to turn theoretical models and predictions into experimentally verified materials, and ultimately into high performice thermoelectric devices. Before getting into the specifics of how my work has contributed to this goal, it is important to have a long-term and short-term understanding of thermoelectrics, along with an understanding of the underlying processes that result in such a phenomenon.

1.1 Historical Background

In 1821 Thomas Seebeck found that if two metals were joined, heating one junction induced a current to flow. This property was initially discovered using strips of copper and bismuth; subsequently many combinations of metals were found to exhibit the same property, and

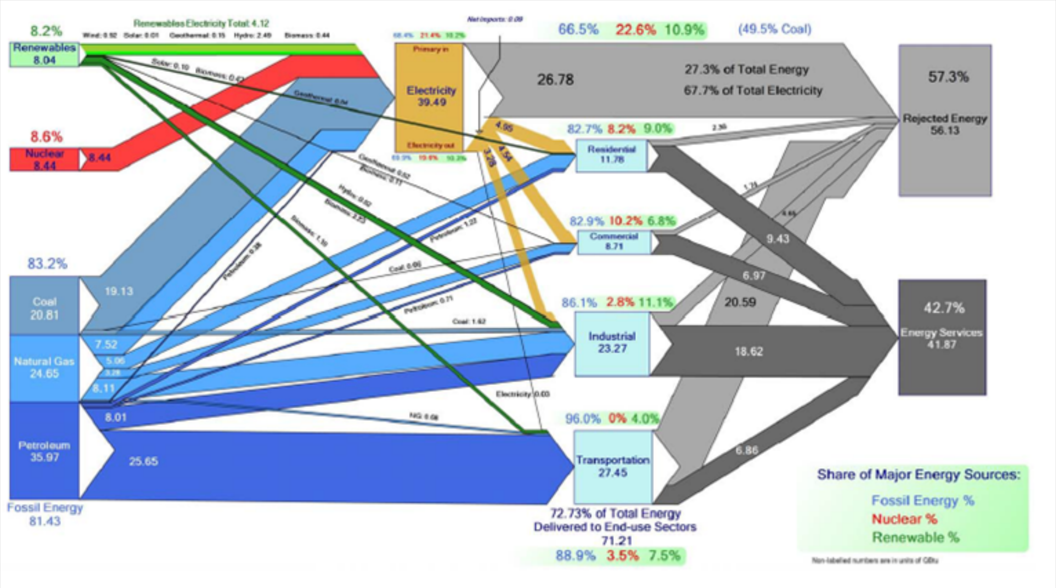

Figure 1.1: Sankey Diagram of 2010 US Energy Flow[72]. The left of the diagram shows different energy sources and their relative abundance; each source is linked to its use in the center, and finally the amount of energy lost and used is collected in the rightmost part of the diagram.

even holding one junction in his hand was sufficient to produce a measurable current. This phenomenon became known as the Seebeck effect, and is most notably used in thermocouples as a way to measure temperature. A short time later in 1834 Jean Peltier independently discovered the reverse to be true; he found that an electrical current would cause heating or cooling at a junction of two disimilar metals. Within 4 years this second but related phenomenon was being exploited to freeze water, and then melt it by Heinrich Lenz. Lenz would get his own law named after him in electromagnetism, however, this marvel would later be known as the Peltier effect. Finally in 1851 William Thomson predicted and discovered the third thermoelectric effect; a material through which a current is driven while a temperature gradient exists across the same material, will absorb or emit heat depending on the material. As would be expected (especially given the first two named phenomena), this would be known as the Thomson effect. Although all three thermoelectric effects were discovered and utilized, it took some time for overall thermoelectric performance to be quantified.

In two publications from 1909 and 1911, Edmund Altenkirch codified the ideal properties of a thermoelectric material. He showed that materials should possess high Seebeck coefficients, high electrical conductivity, and low thermal conductivity. The Seebeck coefficient measures the voltage created for some temperature gradient, ($\frac{\delta V}{\delta T}$), and it would obviously be desireable that a larger voltage be extracted from the same temperature profile. Similarly it is desireable that this temperature gradient be easily maintained, which would support the desire for low thermal conductivity. Lastly, a lower resistance results in less Joule heating, which would heat up the whole material and work against cooling of the cold end. These were still somewhat qualitative observations, that would ultimately be quantified in the figure of merit (ZT) by Abram Fedorovich in 1949; ZT weighed the relative importance of each factor, and allows for the qualitative comparison of two different thermoelectric materials.

$$ZT = \frac{S^2\sigma T}{\kappa} \tag{1.1}$$

In this equation, T is temperature, σ is the electrical conductivity, κ is the thermal conductivity, and S is the Seebeck coefficient. Although useful for allowing relative comparisons between different thermoelectrics, the figure of merit is also useful in comparing the theoretical performance of a thermoelectric device used for electrical generation to other heat engines; the maximum Carnot efficiency for a thermoelectric can be described as

$$\eta = \frac{T_H - T_C}{T_H}\frac{\sqrt{1+ZT}-1}{\sqrt{1+ZT}+\frac{T_C}{T_H}} \tag{1.2}$$

Here, η is the maximum Carnot efficiency, that the thermoelectric could produce, T_H is the hot side's temperature, while T_C is the temperature of the cold side, and ZT is the figure of merit for the whole device. It is with the mix of properties in equation 1.1, that a general blueprint for the best thermoelectric materials is created. Typically, the electrical and thermal properties of a material change together; as illustrated by figure 1.2, the ideal material for a high ZT thermoelectric is one in which a balance is struck between conductivity and resistance. Insulating materials have ideal thermal properties, but poor electrical properties, while metallic materials are electrically ideal, but too thermally conductive. By finding a balance between these two extremes, the figure of merit can be optimized.

By striving for these basic principles many exciting thermoelectric materials were discovered. By the 1950's, devices with Carnot efficiencies of 5%, and with the ability to cool from ambient temperatures to below 0°C, were developed. It was thought that thermoelectrics would soon replace conventional heat engines and refrigerators; instead research stalled as a ceiling was found for materials of ZT=1 ($\eta = 10\%$).

The promise of thermoelectrics was and is great, but their practical use has been limited by low efficiencies. Rather than being a ubiquitous part of our lives, they are materials that are largely unknown outside the chemistry and material science worlds. Even so thermoelectrics have found their way into many niche applications. Small portable thermoelectric refrigerators, where a compressor would be too heavy and a lower efficiency cooler can do the job, are now easily purchasable online. Thermoelectrics have also made their way into the Voyager and Cassini space probes, as a means of constant and reliable power generation in deep space, where light from the sun is too dim to be a feasible option. These probes, Voyager in particular, have highlighted the robustness and reliability of thermoelectric modules. In each of these spacecrafts, radioactive decay is used as a heat source relative to the cold of space; these radioisotope thermoelectric generators (RTGs) continue to power the Voyager spacecrafts well beyond expectations. The tunability of thermoelectrics has also been utilized recently in the creation of an active camouflage in the infrared spectrum; the

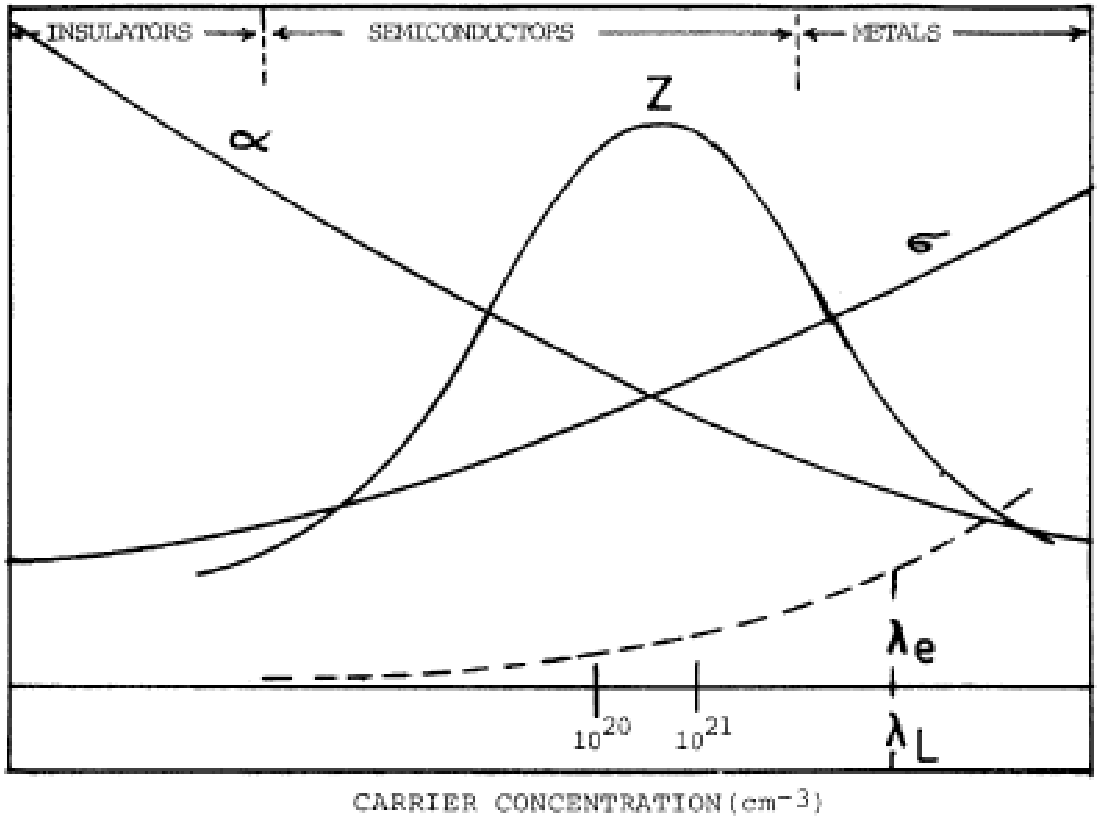

Figure 1.2: General trends for each property that contributes to the figure of merit for varying carrier concentrations[28], where α is the Seebeck coefficient, σ is electrical conductivity, and λ is the thermal conductivity in the lattice (λ_L) and due to eletrons (λ_e)

cloak uses panels of thermoelectrics all over the surface of a vehicle, such as a tank, and small cameras around the vehicle take infrared images of its surroundings. The panels are then used like IR pixels, whose signature is changed by controlled and tunable heating/cooling (figure 1.3. In this way the tank can blend in with its surroundings (IR invisible), or even overlay an image, so the optically visible moving object might be disguised as a car or even a cow.

The final interesting application I will mention, is that of thermoelectrics as photothermovoltaics; large amounts of sunlight can cause large thermal excitation, a hurdle for most conventional photovoltaics. Replacing a photovoltaic with a thermoelectric, and painting it with a highly absorptive coating results in a huge (many 100s of ^{c}ircC) temperature gradient which would generate large amount of electricity[59, 18]. Alternatively, a hybrid of photovoltaics and thermoelectrics could also be used[17, 57].

No matter what the use, thermoelectrics would benefit (and in some applications require) better efficiencies. In order to make higher efficiency semiconductor based thermo-

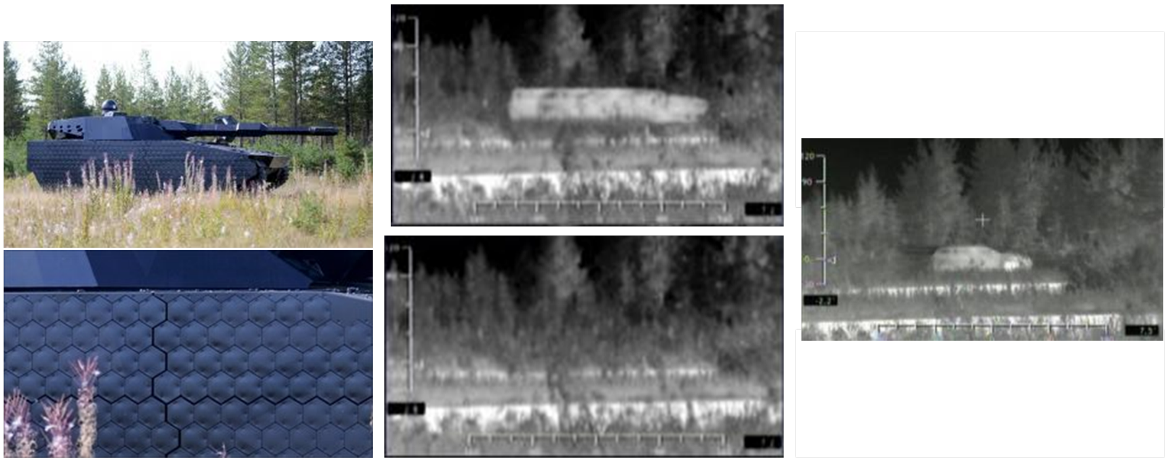

(a) Photograph of the thermoelectric panels used for this IR cloak

(b) IR images of the tank not using the cloaking system, and while using the cloaking system

(c) IR image of the same tank posing as a car

Figure 1.3: Images from muliple articles and press releases on IR cloaking technology developed by BAE systems, from late 2011

electrics, properties that are highly interdependant (the Seebeck coefficient and the thermal and electrical conductivities) need to be decoupled and manipulated in ways that require an understanding of what really causes them in the first place.

1.2 Scientific Background

There are two important classes of semiconductors, n-type and p-type. The two classes distinguish the majority carrier, the carrier which must be considered for charge transport; in an n-type material it is an electron, while for a p-type material, this is a hole. It is easier in this discussion to focus on n-type materials and have it be understood that the inverse would occur with a p-type material. In this way a discssion of just n-type materials, where the transport of electrons is the focus, is sufficient for the understanding of the material properties in all thermoelectric materials. This is not to negate the importance of both types, which are required in most applications, but instead to simplify the discussion.

The source of the thermoelectric effects can be easily understood by looking at the band diagram of a semiconductor; although the same thought process can be applied to insulators and metals. It is most applicable to focus on small band-gap materials. At absolute zero, electrons will populate up to the fermi level, which lies between the conduction and valence bands; as such, the conduction band will be empty. As the temperature increases, however, thermal excitation will allow for some electrons to move to the higher conduction band. It is electrons in this conduction band that will have the freedom to move around and create a current.

Now imagine a semiconductor heated on one end (fig 1.4). On the hot end there will

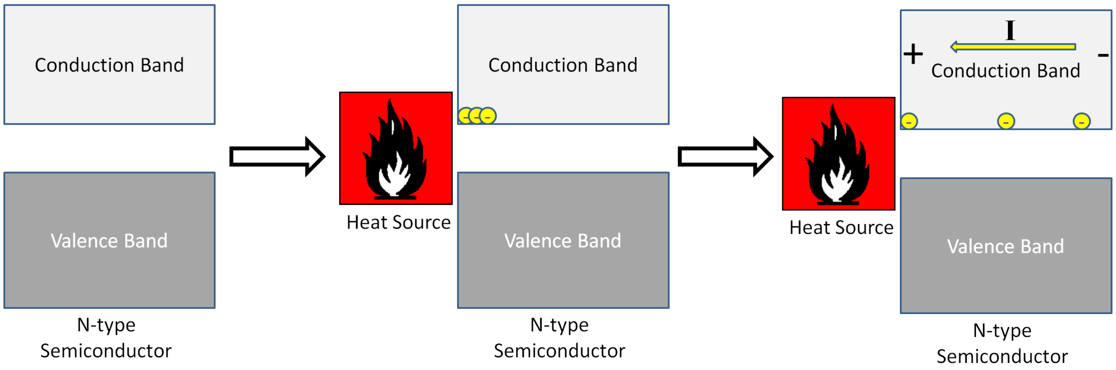

(a)

Figure 1.4: Cartoon demonstrating how the Seebeck effect arises

be a larger population of electrons than on the cold side. As these electrons are free to flow through the material they will spatially redistribute in the conduction band, resulting in a net current of electrons moving from the hot to the cold side (by convention current moves opposite to electrons, in this case cold to hot). Although the electrons appear equally distributed (fig 1.4), the electrons shown are representative of distribution in the conduction band; since these electrons came from the valence band on the hot side, there will be a net electron deficiency on that side. The same principle applies, in the opposite direction, if one cools one side instead of heating it up, as long as there is a resultant temperature gradient. The deficiency and excess of charge along the length of the material creates a (Seebeck) potential across the material; as noted earlier, the Seebeck coefficient of a material is the potential created by a temperature difference across a material, or more specifically

$$S = \frac{V_{Seebeck}}{T_{Hot} - T_{Cold}}. \tag{1.3}$$

By convention the voltage is measured at the cold side in reference to the hot side. By doing so an n-type material gives a negative value, while a p-type material gives a positive value. These potentials and currents working opposite to each other for each carrier type helps explain why thermoelectricity is reliant on majority carriers; the effect may be occuring for both carrier types, but in most cases the majority carrier contribution will exponentially outweigh that of the minority carrier, to the extent that we can in fact ignore it.

One could also picture the reverse effect by imagining a semiconductor metal junctions on either end. If a potential is applied in series with this material a current will begin to flow. Although the fermi level for the semiconducting material lies between the conduction and valence bands, for the metals it lies within the conduction band 1.5. As an electron travels from the negative pole to the positive pole, it must jump to the conduction band in order to conduct (fig 1.5b), and it must absorb some thermal energy to do so. It can then freely travel through the semiconductor's conduction band (figure 1.5c), where it will ultimately return the metal. As it makes this transition it sheds the energy gained earlier (fig 1.5d). In this way one side of the semiconductor continues to lose thermal energy (cool down) while the other continues to gain it (heat up), as in figure 1.5e.

This process can also be viewed in a different, but equally valid manner. Electrons in the metal near the negative pole can have many energy levels due to thermal excitation, but will only go into the semiconductor if they have a high enough energy. In this way, high energy electrons are siphoned away from the metal. If only high energy electrons are removed, the remaining electrons will be on average lower in energy, and a reduction in temperature will be observed. At the same time, relatively high energy electrons will be moving from the semiconductor the the metal on the positive pole increasing the average electron energy. This will result in a temperature increase on this side.

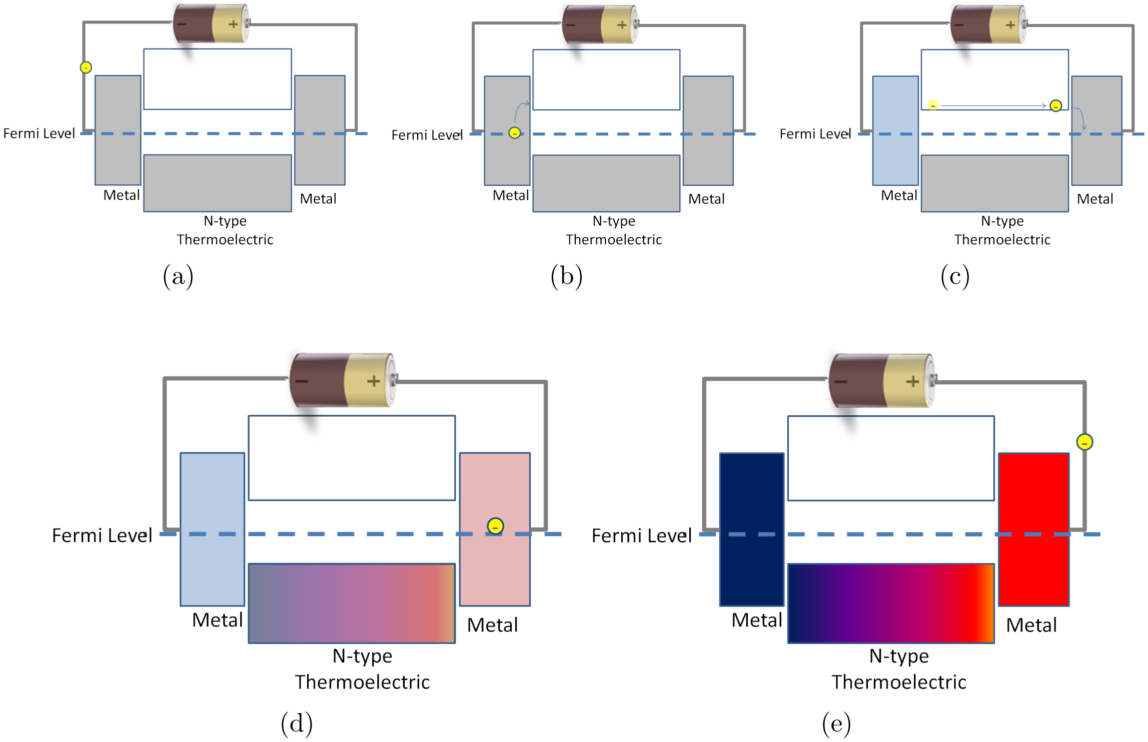

(a) (b) (c)

(d) (e)

Figure 1.5: Cartoon demonstrating how the Peltier effect arises

Understanding how the Seebeck effect occurs, leads to the question of why does one material have a larger or smaller Seebeck coefficient. It is easy to see that it is better to have more electrons promoted to the conduction band on the hot side, relative to the cold side, under the same thermal conditions. It would make sense then to analyze how many electrons will get promoted at a given temperature, which requires us to view the bands as collections of innumerable quantized states. The density of these states per unit energy (analogous to degeneracy when thinking of atomic or molecular orbitals) is of import. Not surprisingly, each material (and even different constructs of the same material) has a unique DOS; however, general trends can be extracted. If the conduction band of a bulk material is considered as a 3-dimensional free electron gas, the shape of the density of states will have the form $D(E) \propto E^{\frac{1}{2}}$[54, p.140]. Furthermore, thermal excitation of electrons relates to temperature by the boltzman constant, k_B, such that accessible conduction states can be viewed as those which are within k_BT of the Fermi level. A higher density of states near the bottom of the band will therefore correlate to a higher Seebeck coefficient. This is clearly a simplification, as the relative populations at two temperatures each need to be considered in order to evaluate the Seebeck coefficient; however, as a guide one can assume that k_BT_{Cold} is small enough that it is smaller than the gap between the fermi level and the band base, while k_BT_{Hot} is larger than that. In this case the area under the DOS curve between the Fermi level and k_BT above the Fermi level is the focus.

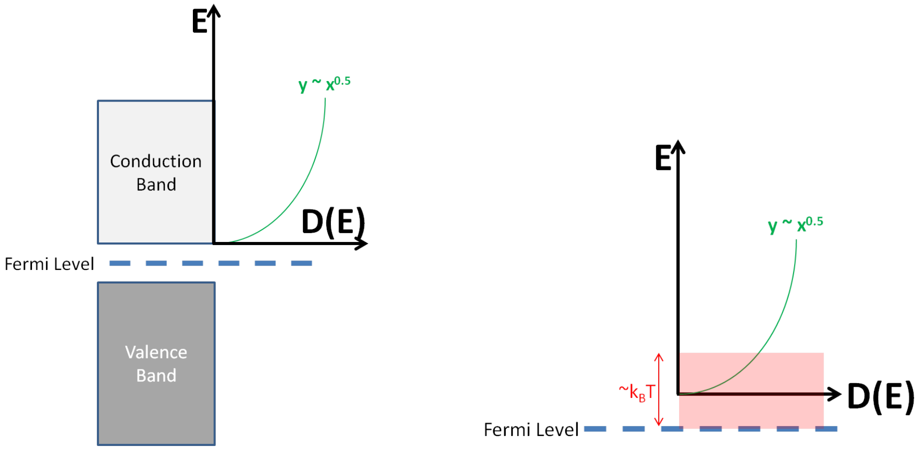

(a)

(b)

Figure 1.6: Cartoons showing the DOS for a 3-dimensional material. Accessible conduction band states for a moderate temperature are shown in red

The DOS can be greatly manipulated by changing only the shape of the material, not the material itself. Taking the same 3-dimensional material and making it into a 2-dimensional material results in a marked change in the DOS; rather than have an $x^{\frac{1}{2}}$ dependance on energy, as the density of states is independent of energy ($D(E) \propto E^0$). The 2-dimensional confinement means that there is some quantization and so there is a secondary structure to the DOS; for each quantized energy level, $n = 1, 2, 3, ...$ there is a constant number of states, but at higher energy levels the contribution is from multiple states. So instead of a uniform DOS at all energy levels within the band, there is an accumulation which looks like a stairway (figure 1.7). The steps occur less frequently as the spacing is the difference of sqaures.

For a 1-dimensional material the DOS actually has a shape related to $D(E) \propto E^{\frac{-1}{2}}$(figure 1.7). As with a 2-dimensional material, however, the quantization of energy levels must be convoluted with the macroscopic shape of the DOS; in this case ($n_x = 1, 2, 3, ...$, $n_y = 1, 2, 3, ...$) and spacings depend on the difference between $n_x^2 + n_y^2$.

Finally, as shown in figure 1.7, for a 0-dimensional material (quantum dots) the DOS is strongly quantized, with only well separated, highly degenarate energy levels.

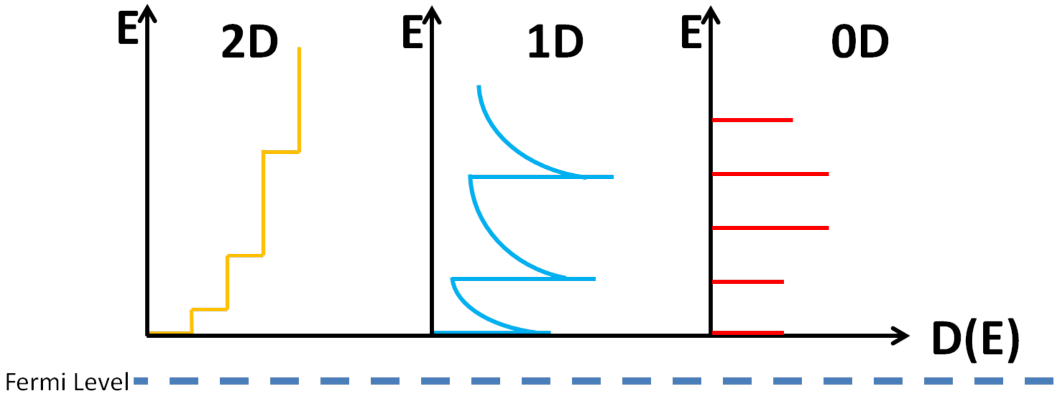

Figure 1.7: The DOS for a theoretical material that is spatially confined in one, two, or all three dimensions

It is the DOS for one and two dimensional materials which helped Hicks and Dresselhaus reignite great interest in thermoelectrics in the 1990's [43, 45, 44, 63, 7, 85, 42, 26, 27]. It was realized that this change in the shape of the density of states makes accessible many more states near the Fermi level (figure 1.8); in other words, many more electrons could get promoted to the conduction band at the same temperature. This would theoretically result in a higher Seebeck coefficient without largely changing the other properties of the material, which in turn would largely influence the figure of merit quite positively. This realization started the resurgence in research of spatially confined materials for thermoelectric applications, but ironically it is precisely a change in a different property that has been most promising.

Rather than altering the electrical properties, spatially confined materials have a much reduced thermal conductivity. For many materials the mean free path of a phonon is on the order of tens or hundreds of nanometers, so feature sizes smaller than this will increase phonon scattering, reducing thermal conductivity. This can be achieved for a bulk material by ball-milling a highly crystalline sample and then hot-pressing the powder into a pellet[105, 77, 50, 102, 29]; these pellets will be comprised of many nanocrystalls, small enough to largely hinder phonon transport, but also granular enough that electrical transport is hindered. Overall the drop in thermal conductivity outweighs the change in electrical properties, resulting in materials which are 50% or even 90% more efficient that their crystalline bulk counterpart. Alternatively, films[107, 89, 101, 64, 67, 22, 104, 21, 41, 75, 93, 6, 100, 39, 56, 48, 2] or nanowires[25, 65, 66, 67, 53, 68, 56, 46, 12] can be grown on similar size scales, such that phonon transport is arrested.

Wires are much more attractive than films not only because of a greater confinement, but because they are more intuitively incorporated into a device; the confinement of a film

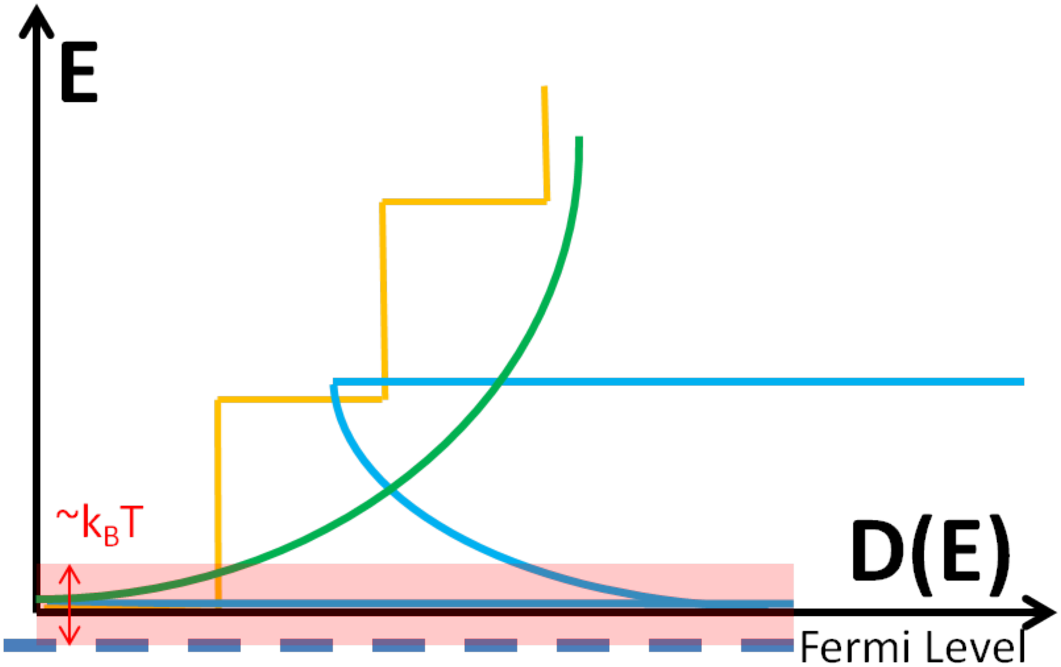

Figure 1.8: The DOS for a theoretical material that is spatially confined in one, two, or no dimensions

requires that the hot and cold side be separated edge to edge, not top to bottom as might be expected[69]. Nanowires, on the other hand, have only one reasonable geometry for use which fits well with most growth methods, where the wires grow by becoming longer and longer. Highlighting the progress and potential for nanowires are studies of silicon nanowires in particular[46, 12]; these studies looked at an incredibly poor thermoelectric, and found a greater than fifty-fold increase in ZT for nanowires. This increase in performance was entirely due to a near hundred-fold drop in thermal conductivity for wires of 50nm. Unfortunately silicon is such a bad thermoelectric, that even a fifty-fold increase in ZT is only ZT = 0.6; however, these experimental results give great promise that other established thermoelectric materials will have very high ZT's once confined. For example, even a five-fold increase in the ZT of bismuth-telluride, would make it out-perform (efficiency-wise) a basic refrigerator compressor, ignoring the benefits of a non-moving, highly tunable, freon-free component. It is for this reason that we are motivated to grow nanowires of well established, as well as lesser known, thermoelectric materials.

Bismuth telluride is interesting for our research approach as it is a very good thermoelectric in the bulk (ZT close to 1), with a significant thermal conductivity. As with many thermoelectric materials the crystal structure of bismuth telluride is complicated, a large unit cell filled with heavy nuclei results contribute to low thermal conductivities; in particular the bismuth tellurde crystal consists of 15 layers, each made up of either bismuth or tellurium.

There are 5 layer sheets of Te-Bi-Te-Bi-Te which are attracted via Van der Waals forces, and the sheets align such that they repeat relative position every third sheet, as in figure 1.9. Within each sheet there are covalent bonds between bismuth and telluriums above and below them. Furthermore, bismuth telluride has a very small band gap, which helps create a large seebeck coefficient (the fermi level is close to the base of the conduction band).

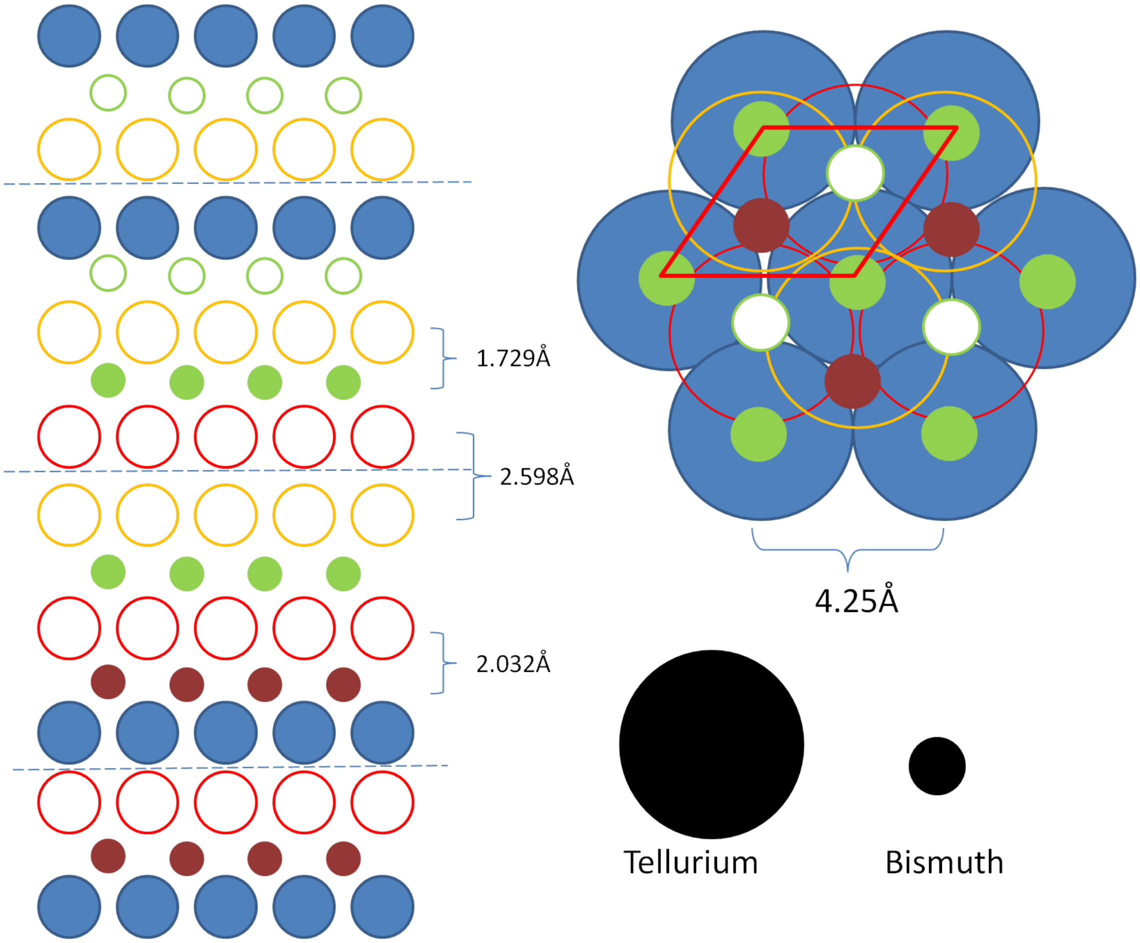

Figure 1.9: Side and top down views of the bismuth telluride crystal structure. Larger circles are used for tellurium, while smaller circles are used to represent bismuth. For the side view are indicated bond lengths for the Te-Te interatomic spacing, and the two Bi-Te bond lengths (internal and external); for the top down view the rhomohedral unit cell is shown in red, with the cell width indicated as well. Lastly, the layers of tellurium which interact via Van der Waals interactions are indicated by a bisecting dotted line.

Another well known bulk material is the alloy of bismuth and antimony. Bismuth antimony also has a layered structure though the packing is quite different. Each layer of bismuth antimony consists of networks of triply covalently bonded atoms, alternating up and down. As both bismuth and antimony have this structure individually, the resultant alloy consists of a random mixture of these two. Changing the antimony content (desired thermoelectrics are generally bismuth rich) can yield vastly different material properties; for example, although both are semimetals in bulk, alloying the two can result in a transition to a semiconductor[93]. It has even been shown theoretically that optimally doped, optimally sized nanowires of bismuth antimony could have ZT / > 2.5[79].

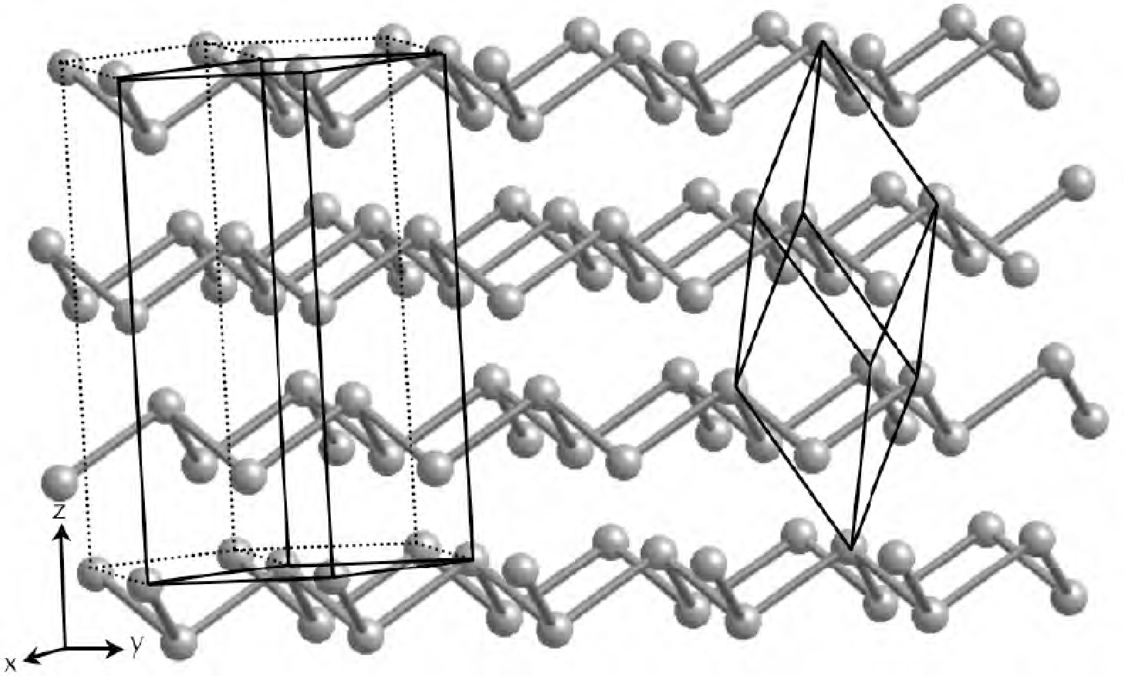

Figure 1.10: Cyrstal structure of $Bi_{1-x}Sb_x$ with the hexagonal and rhombohedral unit cells shown[52]

Although there are many methods to grow nanowires of these materials, we have selected electrochemical deposition into porous alumina. Electrochemical deposition is highly attractive because it is a cheap method that is highly scalable for potential industrial applications. Deposition into porous alumina allows us to grow arrays with billions of electrically isolated wires at once; these wires are parrallel, and embedded in a robust matrix which allows for handling and manipulation.

In the following chapters I will discuss the work behind understanding a novel electrochemical system (antimony and tellurium)in a non-aqueous solvent (dimethyl sulfoxide). After showing what was learned from these studies I will go on to explain the specficis of our growth method. This will be followed by analysis of samples grown by this method, based on information and understanding about the antimony-tellurium system. Lastly I will describe both the unsuccessful and successful measurement techniques used on various types of nanowires.

Chapter 2

The Electrochemistry of Tellurium and Antimony

This chapter describes the electrochemistry of tellurium and antimony through the use of cyclic voltammetry. Dimethylsulfoxide (DMSO) has been used as an alternate in other semiconductor depositions, such as bismuth antimony[52]. The electrochemistry of tellurium has been studied in aqueous solutions; however, it acts quite differently in DMSO. Tellurium nanowire arrays grown in DMSO are not only of higher quality than those grown in aqueous (see chapter 3), but they can be doped as well; in aqueous solutions doping of tellurium is prevented by underpotential deposition of telluride compounds (Sb_2Te_3 in the case of antimony and tellurium). Pure tellurium nanowires have potential uses in optoelectronics [23, 108], piezoelectronics [82], ammonia and carbon monoxide gas sensors [82], and magnetic memories [109]; the antimony doped wires have potential use in thermoelectric devices[23, 82, 109]. With the goal of growing high quality tellurium and antimony doped tellurium, the electrochemical systems of antimony, tellurium were studied individually and together through cyclic voltammetry.

2.1 Cyclic Voltammograms

Cyclic voltammetry (CV) studies are a neccessary step when investigating a new electrochemical system; by sweeping through a range of potentials, and measuring the resultant current, the potential at which oxidative and reductive events occur can be determined.

CVs are typically performed in a three-electrode cell with a disc electrode for the working electrode. A linearly variable voltage is applied between a starting and ending value, while the current is measured. Convention makes more positive potentials oxidative, and more negative potentials reductive; positive currents indicate an net oxidation at the working electrode, whereas negative currents indicate a net of reductive activity at the working electrode. The current is mostly determined by electron transfers at the electrode surface, however, capacitive charging is also a minor factor. The largest usable range is determined by the solvent window. The excess of solvent relative to solubilized species means that at potentials where the solvent can be either reduced or oxidized, there will be a sharp increase in current. This increase will drown out any other signal. Furthermore, the oxidized/reduced solvent may react with the species of interest.

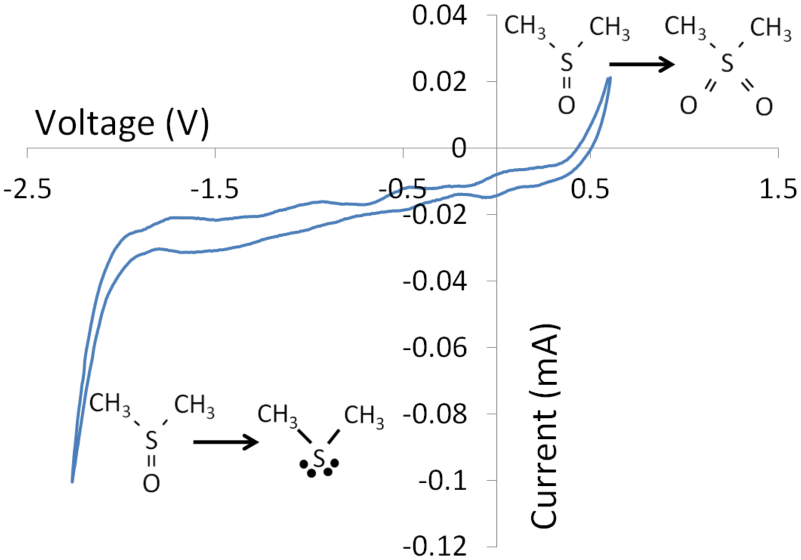

Figure 2.1: CV of 0.3M TBACl in DMSO, showing the solvent window for DMSO

Depending on the solvent an electrolyte may be necessary to allow for charge transfer through the solution by the rearrangement of ionic species. For DMSO, tetra-n-butylammonium chloride (TBACl) is a good choice of electrolyte due to its high solubility, low reactivity with tellurium and antimony cations, and because it has chlorine as an anion. Furthermore, TBA^+ does not contribute electrochemically within the DMSO solvent window, as evidenced by the lack of reductive or oxidative peaks in figure 2.1.

During a CV it is important not to stir the solution and for the solution to have a strong ionic strength, so that transport is diffusion controlled, with migration and convection are minimized. Reduction and oxidation can be treated similarly, with the only salient difference the direction of current. It is easier to speak in terms of only one direction, in this case reduction, as the same logic can be applied in order to understand oxidation.

At potentials which are either near to or more negative than the reduction potential the rate of reduction becomes limited by the number of electrons that are energetic enough to reduce the species.

$$i(E) \propto e^{E_{red}-E} \tag{2.1}$$

Above the reduction potential, where equation 2.1 $\gg 1$, species will be easily reduced; therefore it is the number of unreduced species near the electrode which controls the magnitude of the current. This can be modeled by Ficks second law of diffusion

$$\frac{\delta\phi}{\delta t} = D\frac{\delta^2\phi}{\delta^2 x} \tag{2.2}$$

with the boundary conditions of instant conversion near the electrode surface

$$C(0,t) = 0 \tag{2.3}$$

and a relatively limitless supply of species from the distant bulk solution

$$C(\infty,t) = C_{bulk} \tag{2.4}$$

Combining these two boundary conditions, with the time dependent diffusion conditions described in equation 2.2, we get the Cottrell equation which describes the current decay as $t^{-1/2}$. This current decay occurs even as the applied potential is further increased [70, 3, 30].

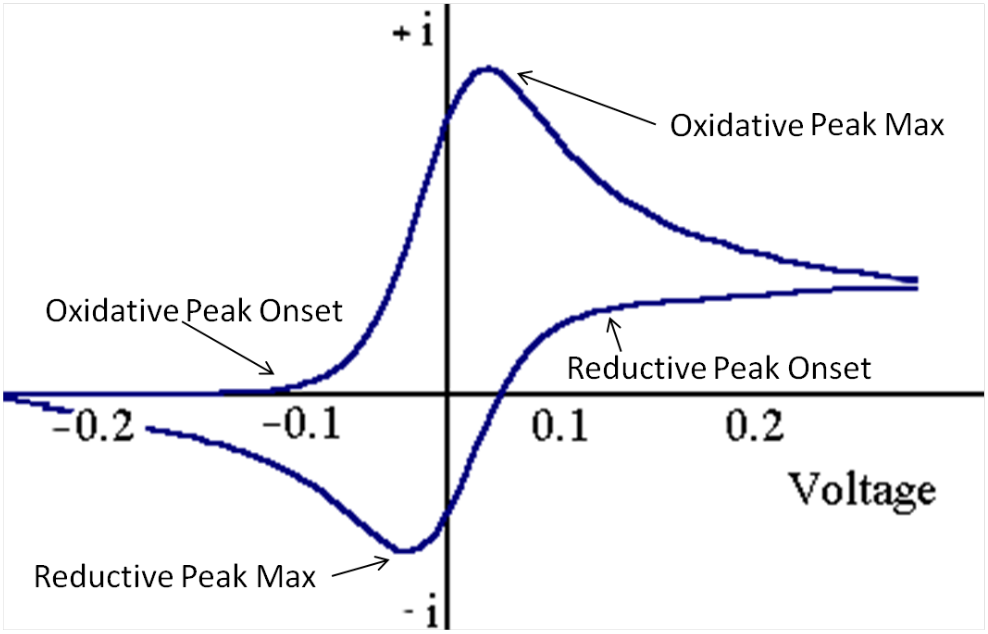

Figure 2.2: Generic CV

For CVs, a working electrode of a platinum wire in a Teflon sleeve was used as a disc working electrode (figure 2.3a). Platinum was chosen because it is the material we use as the working electrode when growing nanowire arrays. The counter electrode is a mesh of platinum attached by a knot to a platinum wire (figure 2.3d). For DMSO, the pseudo-reference electrode is a platinum wire embedded in paraffin wax (figure 2.3c). Each is connected by an alligator clip to a potentiostat that is controlled by a LabView program made in house. A potential difference is created between the working and counter electrode. This potential difference is adjusted until the desired potential difference is created between the working and reference electrode. All of this is controlled quickly enough to be considered instant for

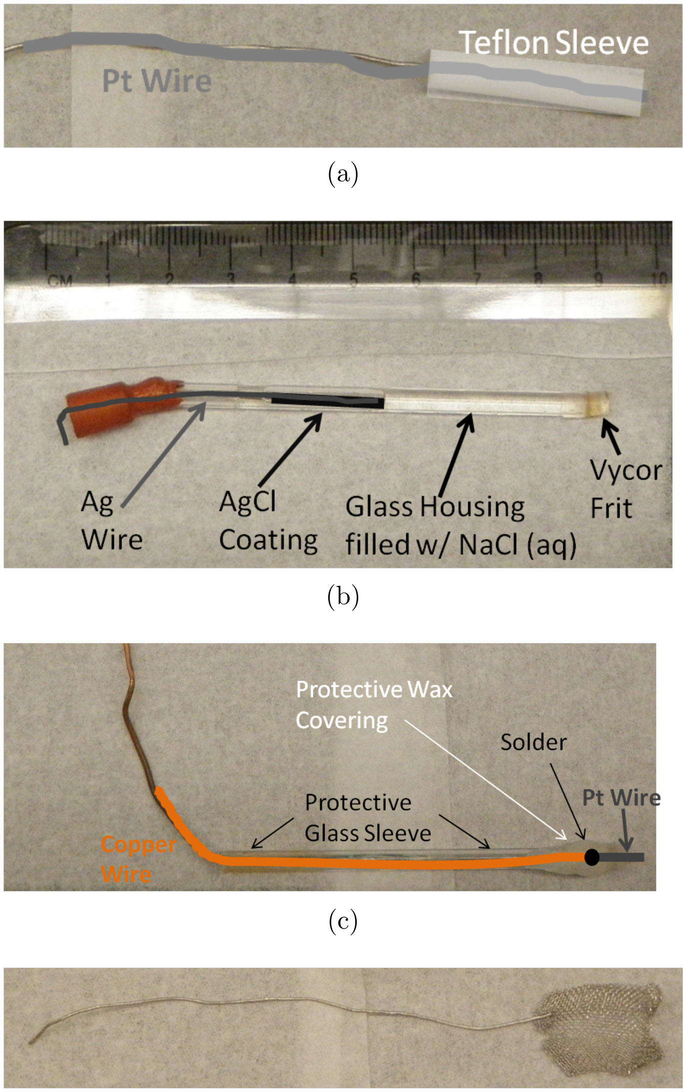

(a)

(b)

(c)

(d)

Figure 2.3: (a) Platinum working disc-electrode for CVs (b) Ag/AgCl reference electrode, for aqueous solutions (c) Platinum pseudo reference electrode, for DMSO solutions (d) Platinum mesh counter electrode

our purposes. Throughout, the program records the current that goes through the working electrode. It is also possible to choose which currents to apply, and the counter electrode's potential relative to the working electrode is varied until the desired current results. In this case the potential difference between the reference and working electrodes is also outputted by the program.

CVs were used to study antimony and tellurium individually, as well as when combined in solution. CVs of each system were studied until all features could be assigned and explained as specific electrochemical events.

2.1.1 Antimony CVs

One of the benefits of moving to DMSO is that antimony is not soluble in water, except under strongly acidic conditions with a stabilizing complexing species. On the other hand, Sb^{+3} in DMSO is very stable without assistance. Despite a very different mechanism, the electrochemistry of antimony in DMSO is similar to that of antimony in acidic aqueous conditions. In this section, the mechanism of deposition for each solvent system are compared.

Citric acid can effectively chelate antimony, and is often used as the stabilizing chelator of antimony in aqueous solutions[22, 21]. In acid solution, whether chelated or not, antimony is present as SbO^+[48, 8]. In order to make aqueous solutions of Sb(III), $SbCl_3$ can be dissolved with tartaric acid (or citric acid) in water. Alternatively, Sb^0 or Sb_2O_3 can be dissolved in nitric acid, and then tartaric acid can be added to complex the oxidized antimony species.

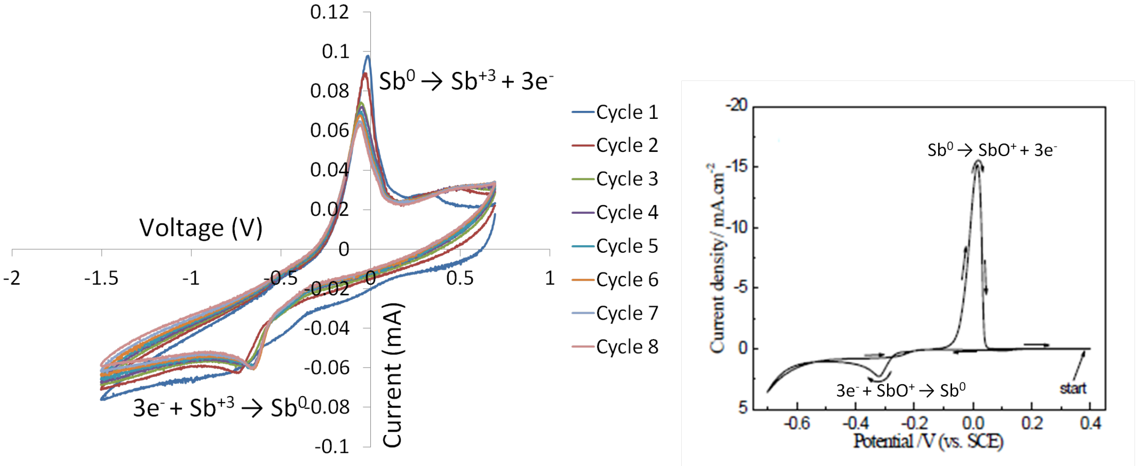

(a) Antimony CV in DMSO

(b) Aqueous antimony CV[31]

Figure 2.4: CV showing (a) multiple sweeps for $SbCl_3$ and TBACl in DMSO and (b) a single sweep for Sb_2O_3 and tartaric acid in 1M HNO_3(aq)

The sharp shape of the oxidative peak (∼0mV versus Ag/AgCl) is due to the availability of the antimony on the electrode surface, rather than needing to reach the electrode via diffusion. The reduction (∼-0.3V versus Ag/AgCl) occurs in a two-step, 3-electron process[31]

$$SbO^+_{ads} + 2e^- \rightarrow SbO^-_{ads} \tag{2.5}$$

$$SbO^-_{ads} + e^- + 2H^+ \rightarrow Sb^0 + H_20 \tag{2.6}$$

In DMSO, no chelation is necessary, and the prevalent antimony species is Sb^{+3}[52]. Sb^{+3} solutions can be made in DMSO by dissolution of $SbCl_3$. Antimony is reduced (∼-0.7V versus Pt wire) through a straight 3-electron transfer

$$Sb^{+3} + 3e^- \rightarrow Sb^0 \tag{2.7}$$

Similarly, the oxidation of Sb^0 (∼-0.3V versus Pt wire) occurs through a single 3-electron tranfer

$$Sb^0 \rightarrow Sb^{+3} + 3e^- \tag{2.8}$$

Although no chelator is neccessary, in order to maintain a sufficient ionic strength, TBACl is also added to the solution. Both TBA^+ and Cl^- are electrochemically inactive in the region of interest, which is verified by the lack of non-solvent peaks in figure 2.1.

The electrochemistry of antimony in DMSO is straightforward, and superficially the same in both DMSO and aqueous solutions; despite the differing mechanish, in both solvents there is a single oxidative and a single reductive peak, neither of which changes over subsequent sweeps. In the case of tellurium there is a also a distinct mechanism, but this also translates into a unique set of electrochemical reactions.

2.1.2 Tellurium CVs

Tellurium nanowires grown in DMSO can be made of much higher quality than those grown in aqueous (chapter 3). Unlike what was seen with antimony, for tellurium, CVs done in DMSO and aqueous solutions vary greatly. In this section each system is described to highlight these differences; for DMSO an in depth explanation and study is described for this previously unstudied system.

Tellurium requires an acidic solution to be dissolved in water, otherwise it will precipitate out of solution as TeO_2. In acidic solutions the tellurium oxide can be protonated, resulting in the soluble species $HTeO_2^+$. Solutions of $HTeO_2^+$ were generally prepared by mixing nitric acid with Te^0, and then adding enough water to get the desired concentration. Enough acid was used to allow the nitrate ion to act as a supporting electrolyte in solution (∼1M), more than 10 times the concentration of the tellurium. A cyclic voltammogram of an $HTeO_2^+$ solution reveals the reduction of tellurium by the equation

$$HTeO_2^+ + 3H^+ + 4e^- \rightarrow Te^0 + 2H_2O \tag{2.9}$$

At largely negative potentials there is a second reductive peak which corresponds to the further reduction of Te^0[24]

$$Te^0 + 2e^- + 2H^+ \rightarrow H_2Te(g) \tag{2.10}$$

Almost all of the H_2Te bubbles off of the working electrode or decomposes quickly, so there is no oxidative peak observed on the positive sweep[65]. In DMSO the CV shape is very different for the first sweep, versus subsequent sweeps, and it is always different from those done in aqueous solutions.

In DMSO solutions the first large difference from aqueous solutions is that tellurium is soluble as Te^{+4} as opposed to $HTeO_2^+$; solutions of which are made by dissolving $TeCl_4$ in

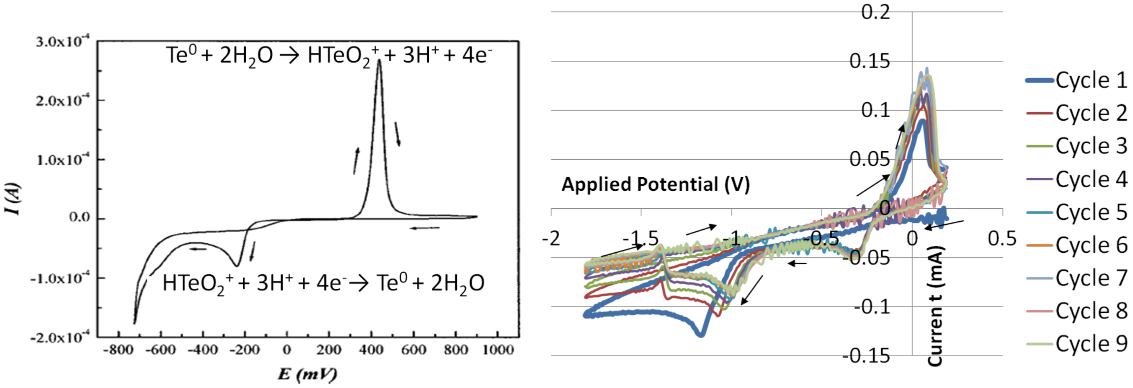

(a) Aqueous tellurium CV with Ag/AgCl reference electrode[65]

(b) CV of all sweeps for tellurium in DMSO

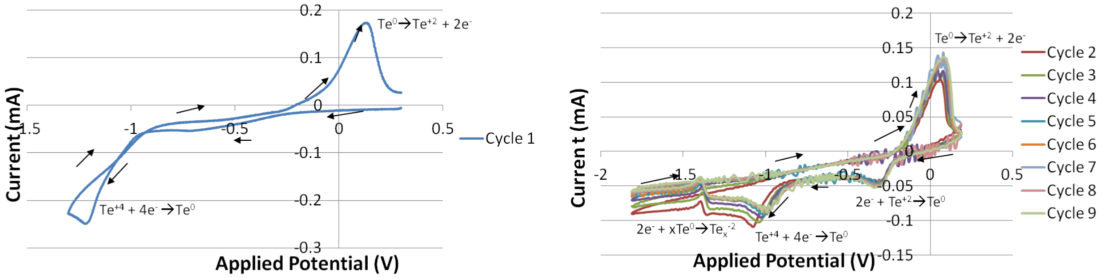

(c) First Sweep for CV of tellurium in DMSO

(d) Second and later sweeps for CV of tellurium in DMSO

Figure 2.5: CVs of tellurium in (a) acidic aqueous conditions (b-d) DMSO with TBACl

DMSO, along with TBACl as the supporting electrolyte. Both species have chloride as an anion, which shows no activity within the DMSO solvent window (figure 2.1). At the start of the CV the only species present is Te^{+4} which is reduced to Te^0 (at ~-1V versus Pt wire)

$$Te^{+4} + 4e^- \rightarrow Te^0 \tag{2.11}$$

During the oxidative sweep Te^0 is oxidized to a cation (at ~-200mV versus Pt wire)

$$Te^0 \rightarrow Te^{+2} + 2e^- \tag{2.12}$$

$$Te^0 \rightarrow Te^{+4} + 4e^- \tag{2.13}$$

$$Te^{+2} \rightarrow Te^{+4} + 2e^- \tag{2.14}$$

It is not immediately certain whether equation 2.12, 2.13 or 2.14 (or some combination), is the correct electron transfer mechanism. However, the prevalence of Te^{+2} in subsequent sweeps (and thus the fact that the Te^{+2} has not all been further oxidized), points to equation 2.13 being the dominant electron transfer method. Both pathways occur at a more positive potential than equation 2.12; equation 2.13 is the transfer of more electrons to the same species, and equation 2.14 is the transfer of the same number of electrons to a less positively charged species. In subsequent reductive sweeps there is a second, smaller, more positive reduction peak observed (at ~-0.3V versus Pt wire); this peak is due to the reduction of Te^{+2} to Te^{0}

$$Te^{+2} + 2e^{-} \rightarrow Te^{0} \tag{2.15}$$

$$Te^{+4} + 2e^{-} \rightarrow Te^{+2} \tag{2.16}$$

As Te^{+2} can be viewed as a partially reduced version of Te^{+4}, it is not surprising that the 2-electron reduction of Te^{+2} occurs at a less negative potential than the direct 4-electron reduction of Te^{+4}. The peak for reduction of Te^{+2}, does not occur if the CV range does not reach the partial oxidation of Te0. This indicates that the peak is indeed the reduction of Te^{+2}, a species which is not present until Te^{0} has been converted to Te^{+2}. Therefore, this peak can be assigned to the reaction in equation 2.15, as opposed to the partial reduction of Te^{+4} in equation 2.16

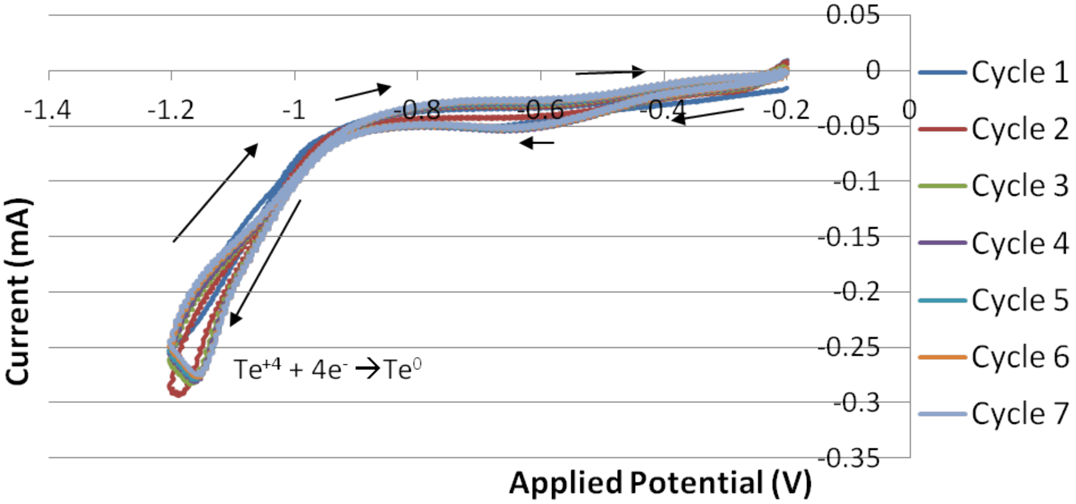

Figure 2.6: CV where oxidative region is not entered

The second CV feature (at ~-1.5V versus Pt wire), occurs only in the second and later sweeps, is seen at very largely negative potentials, as shown in 2.7.

This second feature is quite odd, in that the current oscillates unusually. Tellurium can be reduced beyond its elemental form, as in Bi2Te3, and even form polytelluride chains, Te_x^{-2}[74, 99].

$$2Te^{0} + 2e^{-} \rightarrow Te_2^{-2}[5] \tag{2.17}$$

Polytellurides come in all sorts of structures. The simplest is the diatom seen in equation 2.17, but there are also longer unbranched chains with negatively charges terminal atoms;

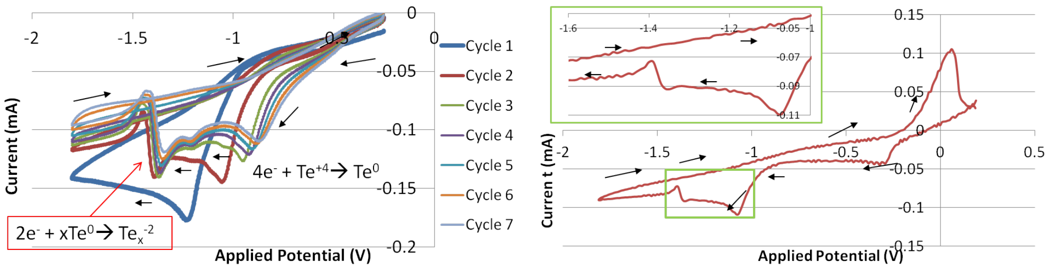

(a) CV of tellurium in DMSO over a limited range: -0.25V↔-1.8V

(b) Single late sweep from a CV of tellurium in DMSO, done over the range: +0.2V↔-1.8V Inset: zoom in on the reduction of Te^0

Figure 2.7: CVs showing the reduction of Te^0

these chains can be 3-5 atoms longs [4] or even commonly 12 atoms long [99]. There are also simply branched chains, or those described as a seven tellurium atom "butterfly" [55]. With rare exceptions the one thing these polyellurides have in common is that they are all of the form Te_x^{-2}, and all readily coordinate cationic species.

In order to study the formation of polytellurides, tellurium can double as the working electrode and as a Te^0 source. Crystalline needles of tellurium can be grown by creating a temperature gradient [83, 20, 86]. Elemental tellurium was placed at the bottom of a $\frac{1}{4}$ inch quartz tube, which had been cleaned with aqua regia and then dried in a furnace. The sample was then heated in a vertical furnace at 500°C ($mp_{Te} = 449.5$°C). After many hours the sample was slowly cooled to room temperature. A nitrogen atmosphere was maintained throughout by flowing nitrogen through the furnace apparatus. The flowing nitrogen worked both to aid the evaporation of tellurium from the melt, and to displace oxygen, preventing the formation of TeO_2. As there is a temperature gradient across the length of the tube, evaporated tellurium deposits along the quartz tube surface in the "colder" regions. Tellurium atoms will preferentially deposit on other tellurium atoms, and from this preferential deposition, needles will form.

A single crystalline needle was mounted in wax, in the same way as the platinum pseudo-reference electrode was used for DMSO CVs, and used as a working electrode. A solution with only 0.3M TBACl was used, and then a CV was swept between -0.5V and -2V. As there is no tellurium initially in solution, there is no reductive current until the potential is negative enough to reduce elemental tellurium. At below -1.75V a reductive current is measured. This reductive current coincides with the formation of a deep red "blob" on the end of the working electrode. As the applied voltage returns above -1.5V this reduction ceases and no more red material is created. The "blob" material sinks, leaving a wispy tail, and slowly changes from deep red to grey. During this time the sweep continues and eventually another deep red "blob" forms and the process repeats; each "blob" continues to sink until it collects with the others at the base of the vessel in which the experiment is performed.

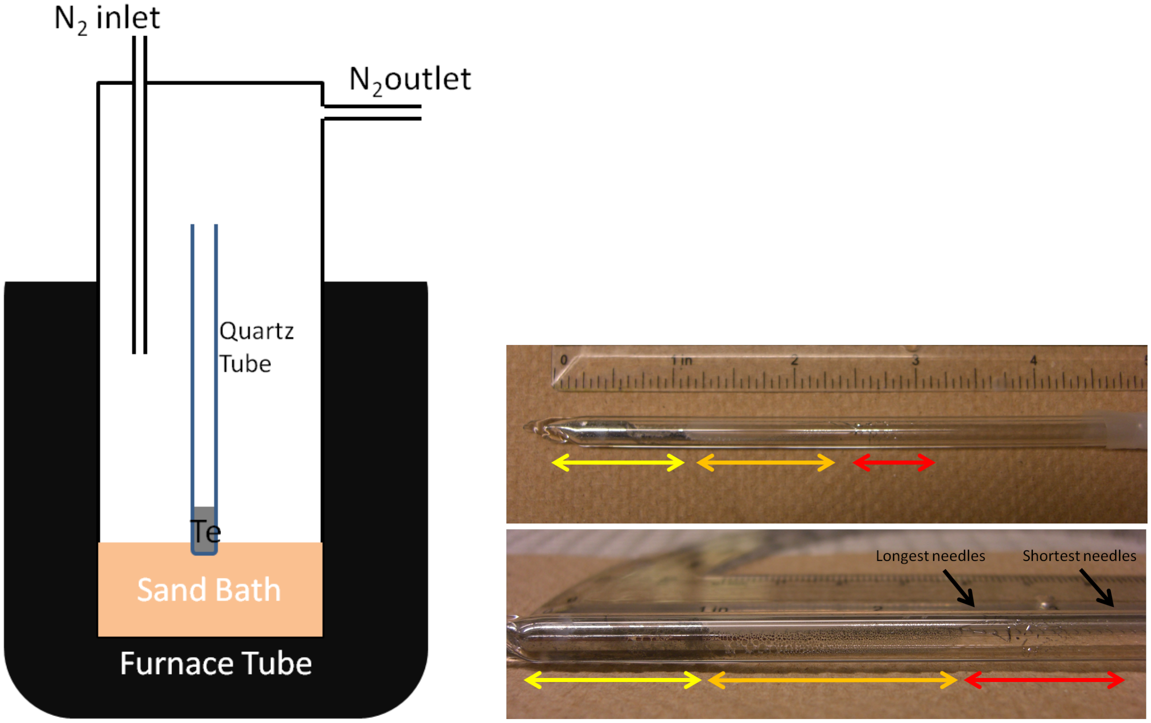

(a) Furnace setup

(b) Tellurium ingot (yellow), non-crytalline deposits (orange), and tellurium needles (red)

Figure 2.8: Diagram of furnace setup used to grow Te needles (a). Photographs of a quartz tube with Te needles (b)

Instead of running a typical CV, a sweep can be run where at each end of the sweep the potential is held steady. This type of cycling was run, and the result, can be seen in figure 2.11. Qualitatively the observed reactions match observations previously done in aqueous solutions with an $SbTe_{10}$ working electrode; specifically a color change to gray, which is linked to the formation of the insoluble salt, $TBA^+(Te_{12}^{-2})$ [99].

The color and peak position observed agree with previous observations[99] and confirm that polytellurides are indeed being formed during CVs in very reductive regions (fig 2.7). In CVs there is no red coloration observed because the amount of tellurium on the working electrode is minimal, merely layers on the platinum disc surface rather than a large crystalline needle.

Knowing that there are polytellurides being formed can help explain the odd behavior seen in fig 2.7. After the second reductive peak (the reduction of Te^{+4} by equation 2.11) there is a slight incease in current (∼-1.3V), due to the reduction of tellurium to polytellurides. Tellurium on the electrode is not crystalline, so it is reasonable that it will begin to reduce and form polytellurides more easily than would the crystalline tellurium of a needle. As the polytellurides are repelled from the surface (due to their net negative charge), they move

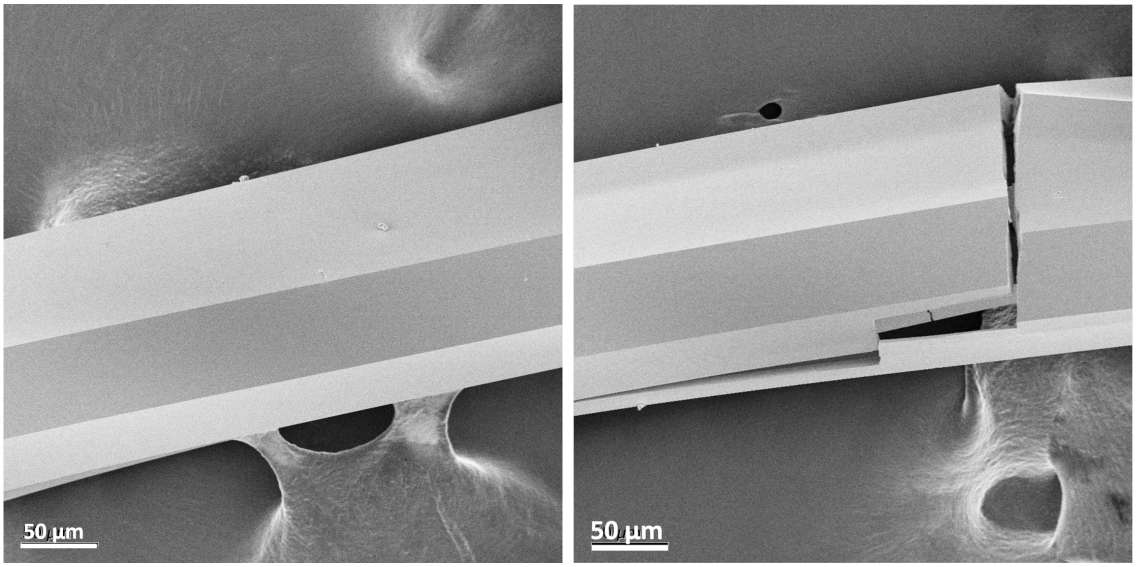

(a) Segment of single crystalline Te needle (b) Broken segment of single crystalline Te needle

Figure 2.9: SEMs of Te needle grown in furnace

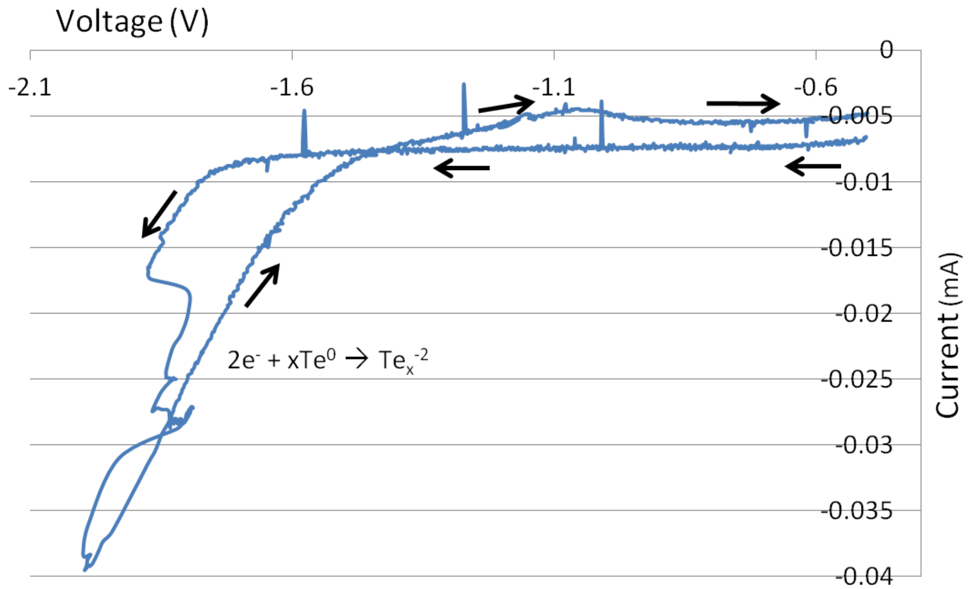

Figure 2.10: CV performed with a tellurium needle as the working electrode

into solution and can react with tellurium cations.

$$Te^{+2} + Te_y^{-2} \rightarrow Te_{y+1}^0 \tag{2.18}$$

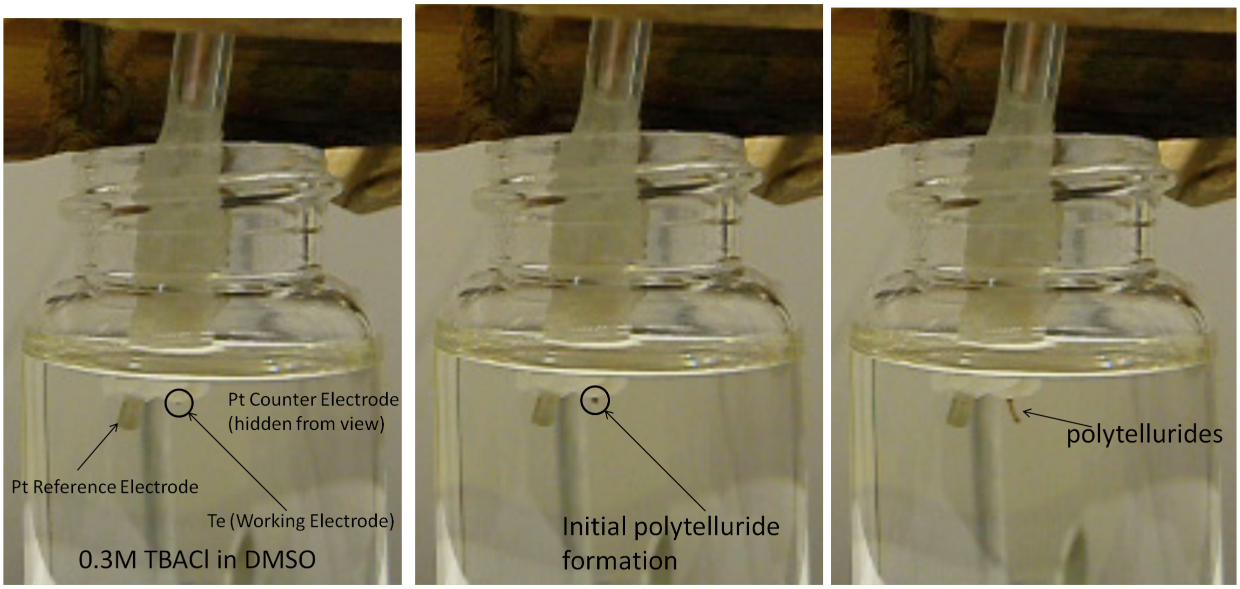

(a) Set up (b) Start of polytelluride formation (c) 10 seconds after start of reduction

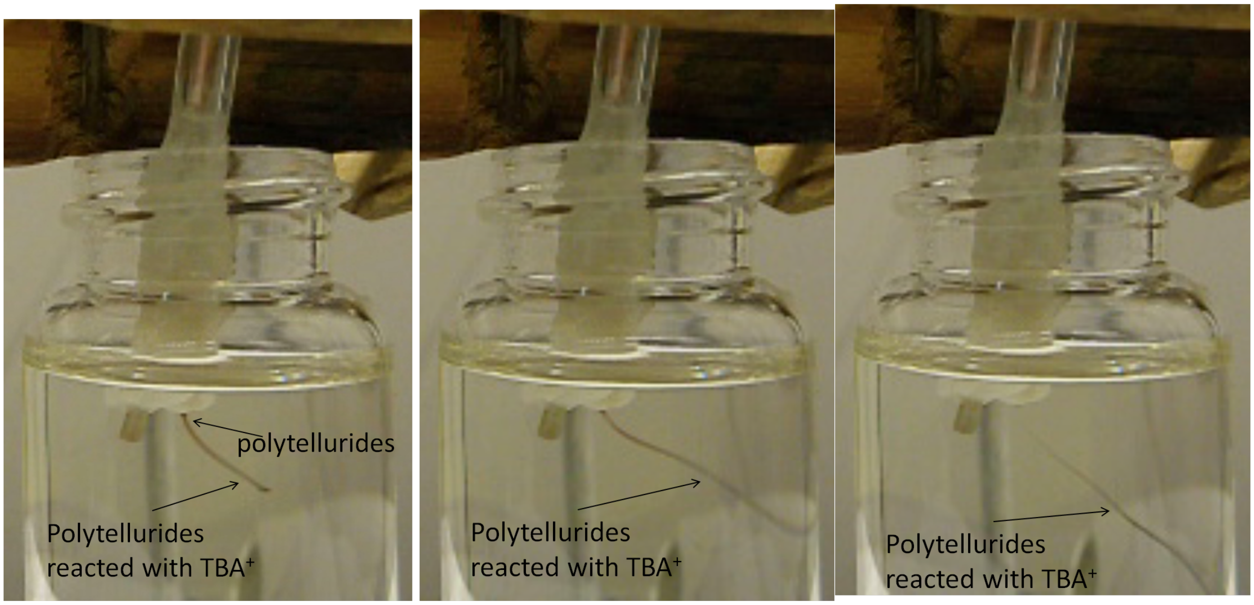

(d) 30 seconds after start of reduction (e) End of polytelluide formation (f) 10 seconds after end of reduction

Figure 2.11: Frames from a video taken during a potential sweep between -0.5V and -2V, holding the potential steady at each end

$$Te^{+4} + Te_y^{-2} \rightarrow Te_{y+1}^{+2} \tag{2.19}$$

$$Te^{+4} + 2Te_y^{-2} \rightarrow Te_{2y+1}^0 \tag{2.20}$$

A wave of polytellurides getting repelled from the electrode will cause a blockade against cations of tellurium reaching the surface of the electrode, and a subsequent drop in the current. At the same time, there is only a very limited amount of tellurium that will have collected on the electrode, and so it is expected that the reductive peak due to equation 2.10 will be small and quickly decay. Once most of the tellurium on the electrode surface has been reduced, further polytelluride formation is rate limited by the reduction of tellurium cations. This will not cause the current to deviate from what would be observed, if no interuption or reaction between the polytelluride and tellurium cations in solution occured (fig 2.12); for each polytelluride chain that requires n electrons, a proportional number of reductions will be prevented, preventing the transfer of n electrons.

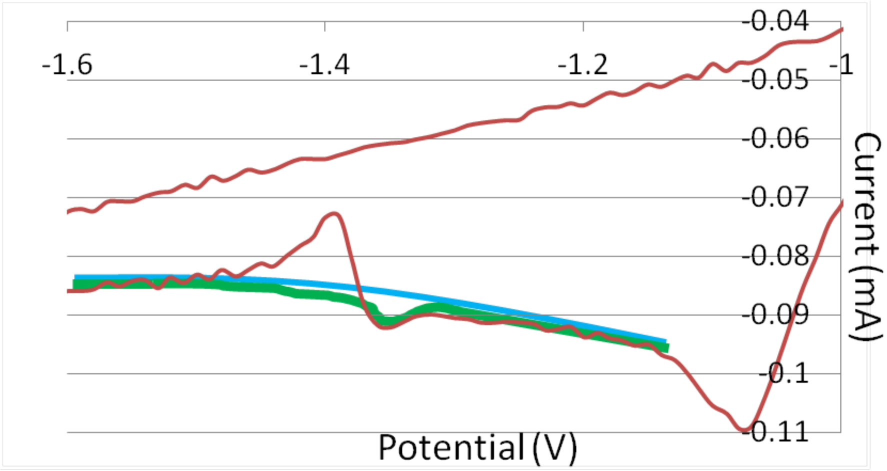

Figure 2.12: A portion of an actual CV of tellurium in DMSO (maroon), with the expected shape for a second reduction that does not interfere with the reduction of tellurium cations (green), and the expected shape for a CV in which no second reduction takes place (blue)

2.1.3 Antimony and Tellurium CVs

Cyclic voltammograms of multiple species are not merely the sum of their parts. There is the likelihood that either a binary compound will result in additional peaks, or that the presence of one species will stabilize or destabilize the reduction or oxidation of the other. The interaction of different species can be studied by looking at CVs where the concentration of one species is changed, while the other is held constant.

When electrochemically deposited in DMSO, tellurium doped with antimony - rather than a binary compound such as antimony telluride, as happens in aqueous solutions - is the deposition product (see section 3.4). Tellurium is a group-VI element, which easily forms bonds between other tellurium atoms; indeed elemental tellurium consists of Te atoms which form parallel three-fold helical chains.

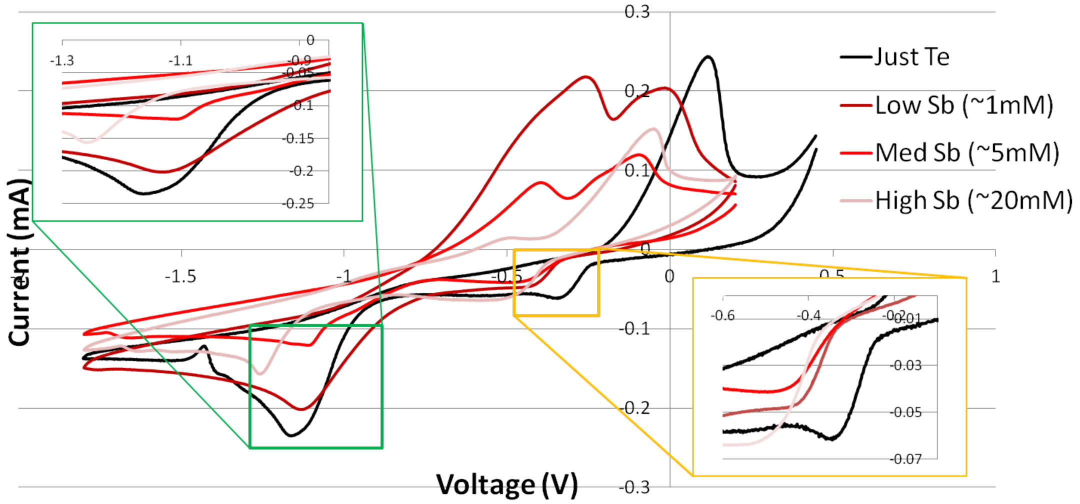

Figure 2.13: Second cycle from CVs of 20mM Te (black), 20mM Te and 1mM Sb (maroon), 20mM Te and 6mM Sb (red), 20mM Te and 20mM Sb (pink). The insets highlight the two reductive peaks and the relative position of those peaks for each solution. (All solutions also contain 0.3M TBACl as a supporting electrolyte)

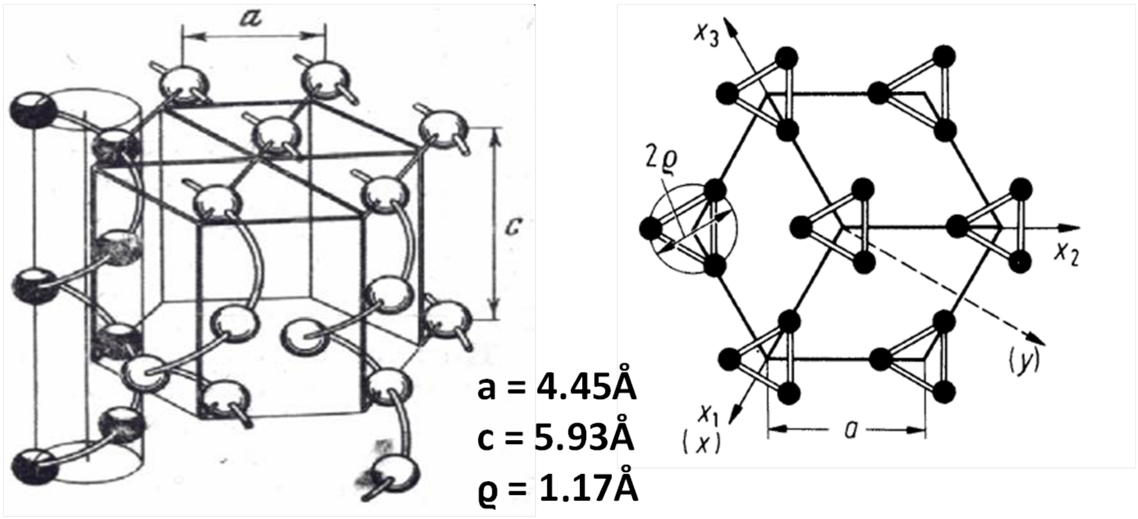

Figure 2.14: Te unit cell[37], with cell dimensions added. 3-fold helical chains are visible for both perspectives

In crystalline tellurium, each atom is singly bonded to two other tellurium atoms, forming chains. These chains are weakly attracted to each other, resulting in the crystal structure shown in 2.14. Dopants can either be interstitially positioned between chains, or can directly replace a tellurium atom in a chain. Electrochemical deposition of tellurium and antimony in DMSO results in antimony interstitially doping tellurium (see section 3.4).

The first (less negative) reduction of Te occurs much more positively than that of antimony. Since this peak occurs before antimony can be deposited, the reduction occuring at this point (~-0.3V vs Pt wire) is only that of Te^{+2}, and not of Sb^{+3}. The shift in peak position at the addition of antimony indicates a destabilization of the deposition of pure tellurium. As this peak only occurs in cycles after the first (section 2.1.2), the deposition is occuring on top of antimony doped tellurium as opposed to pure tellurium. The antimony doped tellurium has a different lattice spacing (section 3.4), and thus the deposition should be less favorable (requiring a more negative potential). This mismatch likely explains the general shift in the first reductive peak (~-0.3V vs Pt wire), with a very slight dependence on the amount of antimony in solution, as seen in the slight negative shift of the peaks with antimony shown in figure 2.13.

The second peak (~-1V vs Pt wire) occurs in a range where both antimony and tellurium can be deposited. Since antimony can and will get incorporated into the deposition product at these potentials, the amount of antimony in solution highly impacts the peak position. Antimony doped tellurium is more stable than pure tellurium, and much more conductive. This stabilization by the addition of antimony results in a positive shift in peak position, seen in figure 2.13. As more antimony is added to solution the peak does not continue to shift positively, but instead shifts to more negative potentials. As more antimony is added to the solution, more antimony is incorporated into the tellurium lattice. Elemental tellurium has full bonding orbitals (figure 2.15), the excess antimony contributes electron density which adds to the anti-bonding nature of the bonds in the tellurium chains. Overall, this leads to a less stable structure as more antimony is in the lattice (requiring a more negative potential). So although the addition of antimony initially causes a positive reductive peak shift, as more antimony is added to solution a gradual negative shift occurs.

2.2 Conclusions

Although tellurium is one of many attractive thermoelectric materials, its deposition in DMSO has not been previously studied. By understanding the electrochemistry of the tellurium and antimony-tellurium systems in DMSO, it is possible to intelligently deposit nanowires of pure or doped tellurium. A less thorough study of the electrochemistry of this system would have sufficed for depositions; however, because most electrochemistry is done in aqueous solutions, it is important to promote and understand the novel opportunities afforded to electrochemical depositions of all materials in non-aqueous solvents. Non-aqueous electrochemistry may be less conventional, but often, it is the best method. The following chapter will demonstrate how knowledge of this system was put to use, by explaining a general method for electrodepositing nanowires; the chapter will then focus specifically on the deposition and analysis of tellurium and doped tellurium wires grown in DMSO.

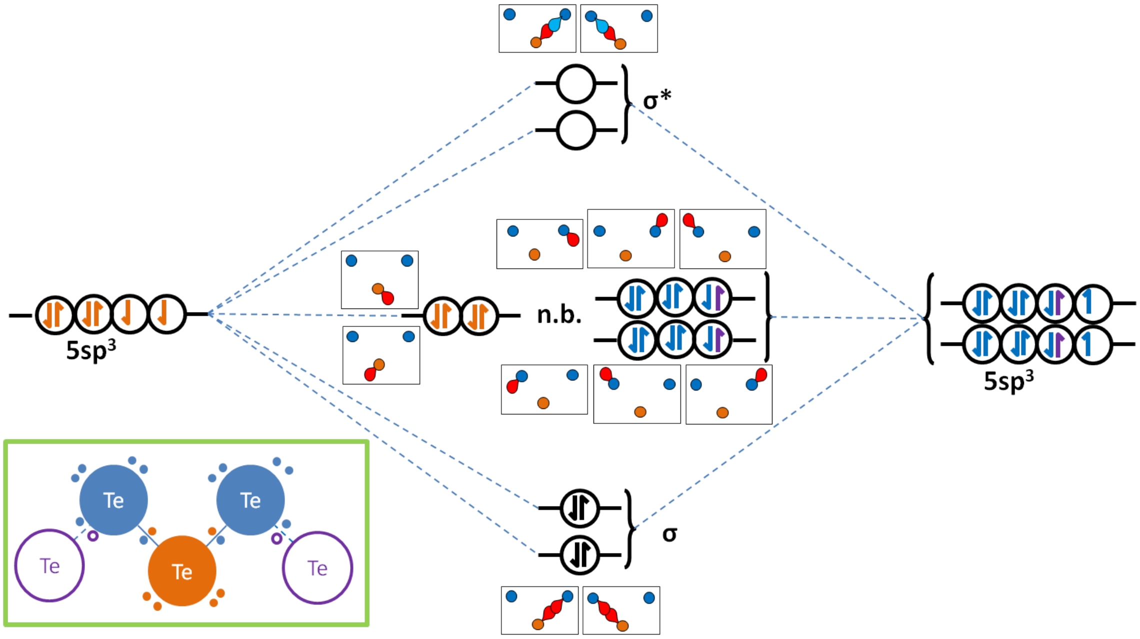

Figure 2.15: Tellurium chains consist of tellurium atoms singly bonded to two other tellurium atoms. A lewis dot representation of this is shown in the green box. The purple tellurium atoms are added to help deal with the fact that the chains are near-infinite, not just a few atoms long. Each tellurium atoms can be treated as sp^3 hybridized, like oxygen in water. The different non-bonding orbitals as well as the σ and σ^* orbitals are illustrated above; red and light blue bulbs represent the main positive and negative lobes for each sp^3 orbital, while the orange and dark blue circles represent the nuclei of the similarly colored boxed off atoms.

Chapter 3

Nanowire Arrays of Tellurium and Antimony

This chapter provides information on both the method of creation and the analysis of nanowire arrays of tellurium and antimony doped tellurium grown in DMSO. Nanowires of tellurium have been grown using a variety of methods [19, 38, 88, 106, 108]. Electrochemically, however, they have previously only been grown in aqueous solutions[108, 109] which results in two main deficiencies. The first deficiency is the inability to easily dope the tellurium nanowires with antimony. Secondly, the quality of aqueous based tellurium nanowires (as well as those grown using other methods), relative to those grown in DMSO, is poor in some or all properties of import (crystallinity, uniformity of growth, orientation, length, wire diameter, and wire density). Described in this chapter is a method for growing isolated high quality wires en masse, with controllable antimony doping, by electrochemical growth in DMSO.

3.1 Nanowire Array Synthesis

3.1.1 Porous Anodic Alumina

Electrochemical deposition of nanowire arrays was done using a template assisted deposition method. Porous anodic alumina (PAA) was formed by anodization of well polished aluminum sheets. The formation of porous aluminum oxide by anodization in an acidic environment is well documented[52, 95, 94, 10, 80, 103, 58, 91, 81, 32]; using a two stage anodization and oxalic acid, highly ordered and reproducible 35-40nm hexagonally packed pores can be made (illustrated in figure 3.1a).

As shown in figure 3.1a, after anodization the pores are only open on one end, and the whole of the PAA is still mounted on aluminum metal. The open end of the pores was sputtered with platinum (or another conductive substance) which would later be used as the working electrode surface. Further processing removes aluminum and leaves PAA with both ends of the pores closed off (one by the aluminum oxide caps, the other by the platinum).

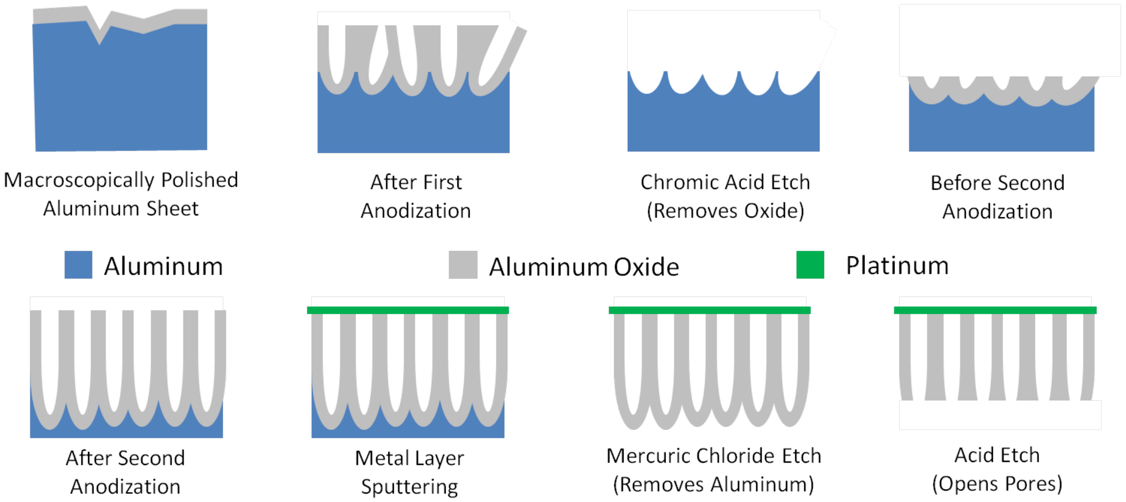

(a) Stages of preparing PAA template

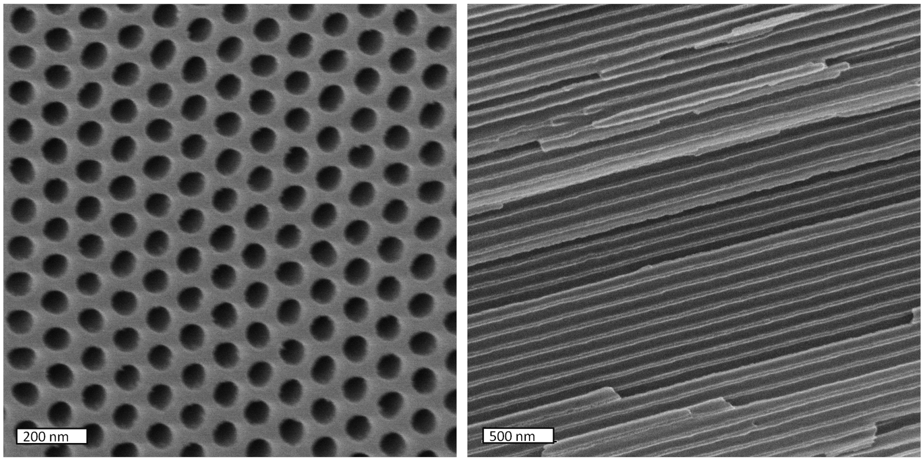

(b) Top down SEM of PAA in which the black circles are the empty pores, and the grey matrix is the PAA itself

(c) Cross-section SEM of PAA

Figure 3.1

3.1.2 Working Electrode Construction

The porous alumina template is mounted onto a copper support using silver paste and later protected with nitro-cellulose (nail polish), and left to dry. The pore bottoms (the barrier layer) are then removed with 10% phosphoric acid. Nail polish degrades in DMSO, so a different coating must be applied to protect the template and prevent growth on the copper support. Parafin wax is easy to apply, is insoluble in DMSO, and inert in the presence of all solution species of interest; the one exception being phosphoric acid. If the phosphoric acid etch is done in the presence of paraffin wax there is no visibly observed change, but upon inspection by SEM, small particles of wax have entered and blocked most pores. For this reason, two stages of protection (nail polish before the phosphoric acid etch, wax before deposition) are done instead of starting with the protective wax layer. Wax does not make a liquid tight seal with the alumina; in order to assure a good seal, at the wax/template surface, ThermalSeal^{TM} was used around the edge of areas to be deposited. When the hot melted wax is applied to the surface it forms a liquid tight seal not only with the alumina, but also with the wax which wets to the ThermalSeal^{TM} surface very nicely.

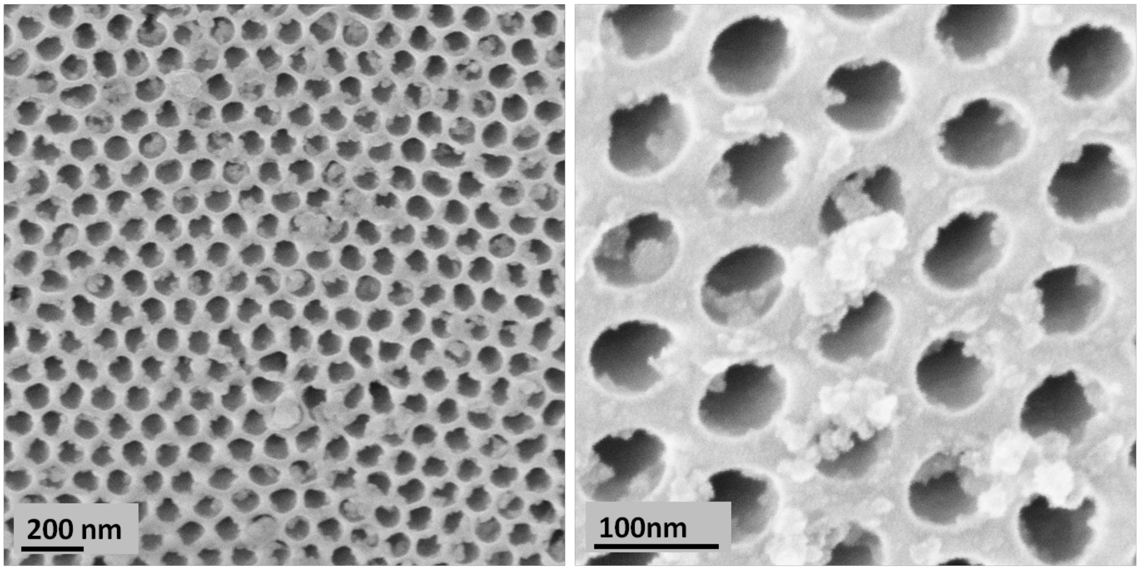

Figure 3.2: SEMs of PAA with pores opened *after* protective wax layer was applied. Wax can be seen blocking many pores in both instances.

At this point, the working electrode is ready for use.

3.2 Nanowire Growth

3.2.1 Deposition Setup

The working electrode is placed in solution and connected to the Potentiostat in the same manner as is done for CVs. Once again a platinum mesh is used as the counter electrode, and platinum wire is used as the reference. Unlike in a CV, the solution is stirred in order to maintain as much solution uniformity as possible during the whole deposition; a variable solution composition, and thus a varying wire composition, results in a less crystalline product.

3.2.2 Deposition Conditions

Information from the CVs presented in chapter 2, and prior work with depositing bismuth-antimony in DMSO[52], helped guide the deposition conditions tested. In particular, tellurium depositions were tested for potentials ranging from -0.75mV to -1.2V (versus a Pt wire reference). Concentrations of tellurium and TBACl for these depositions were based on other depositions in DMSO, and solutions were typically 20mM $TeCl_4$, with between 0.3M to 0.5M TBACl. Antimony doped tellurium arrays where grown with between 0.05mM and 5mM $SbCl_3$; in these solutions the $TeCl_4$ concentration was adjusted to between 10mM and 40mM, depending on what was being studied. Depositions were done into 60μm thick PAA, backed with 500nm thick platinum; pores of 35-40nm were used, resulting in 10^{10} nanowires of 35-40nm diameter per cm^2.

For deposition of pure tellurium nanowires, a 20mM tellurium chloride, 0.5M TBACl solution was used. Similar solutions, with varying amounts of antimony chloride, were used to grow arrays of antimony doped tellurium wires. The porous alumina film will cause slight changes in the electrochemistry on the platinum working electrode. For this reason CV data was used only as a guide to help determine appropriate condition. The source of these changes stem from the fact that even while stirring the bulk of the solution, any solution in the pores will not be affected by convection; this allows factors that rely on diffusion to enter into the picture, factors which normally could be ignored due to stirring. These changes are small, and so the CV data is still a very good guide. Through targeted trial and error high quality arrays of tellurium were found to grow best by direct deposition at -825mV; however, when antimony is added to the mix, a pulsing potential is required for high quality arrays.

The better results noted for pulsing versus direct deposition can be linked to the fact that two, rather than one species is being deposited. Since the transport of each species down the length of the pore will vary, a constant potential will result in changing solution concentrations at the base of the pore over time. A variable solution composition, and thus a varying wire composition, results in a less crystalline product. An example of an ideal array is shown in figure 3.3c. This sample has a uniform growth front, which approaches the top of the template, as well as a high density of wires; furthermore, the XRD (figure 3.3d) shows the sample to be highly oriented.

By periodically moving to a potential range where no electrochemical activity occurs (-400mV works well in the tellurium-antimony system in DMSO), the solution in the pores has time to continually replenish and approach the bulk. For this reason it is also important to use a large amount of solution, and high concentrations of species (relative to amounts deposited) so that the bulk concentration is constant throughout the deposition.

A worst case analysis of concentration change is given to assert that during deposition the solution was not changing significantly over time. For a large sample, the area deposited into is $\sim 1cm^2$, and the longest pore length is 120 μm, with a porosity of 30%(based on SEM image analysis matching literature[10, 11]). This means approximately $0.036cm^3$ of nanowires are deposited in a full $1cm^2$ of 120 μm template. For tellurium this equates to depositing less than 2mmol (assuming a bulk density for tellurium of $6.27g/cm^3$). Using templates that have shorter pore lengths (60 μm), opening a smaller area for deposition (0.25 cm^2), and using a large amount of solution (200mL) the change in tellurium concentration over the deposition is from 4mmol to about 3.8mmol, or 5%. When small amounts of antimony are added, there is an even smaller amount that is deposited and so the change in solution composition over time is minimal. For example, in the sample shown above (figure 3.3) a 0.15mM $SbCl_3$

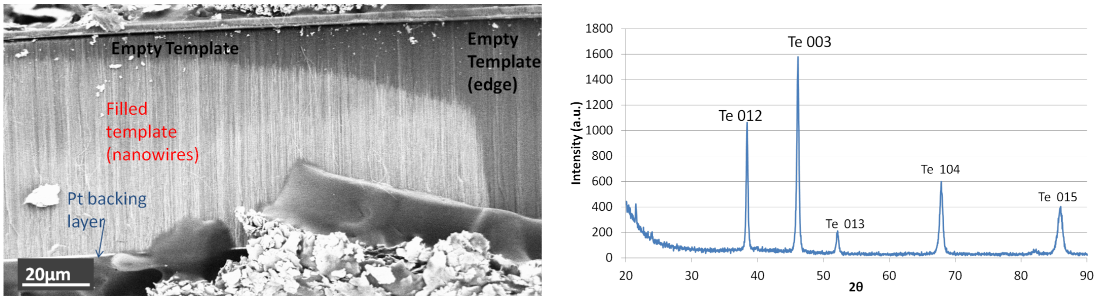

(a) BS-SEM of pure tellurium nanowire array (b) XRD of pure tellurium nanowire array

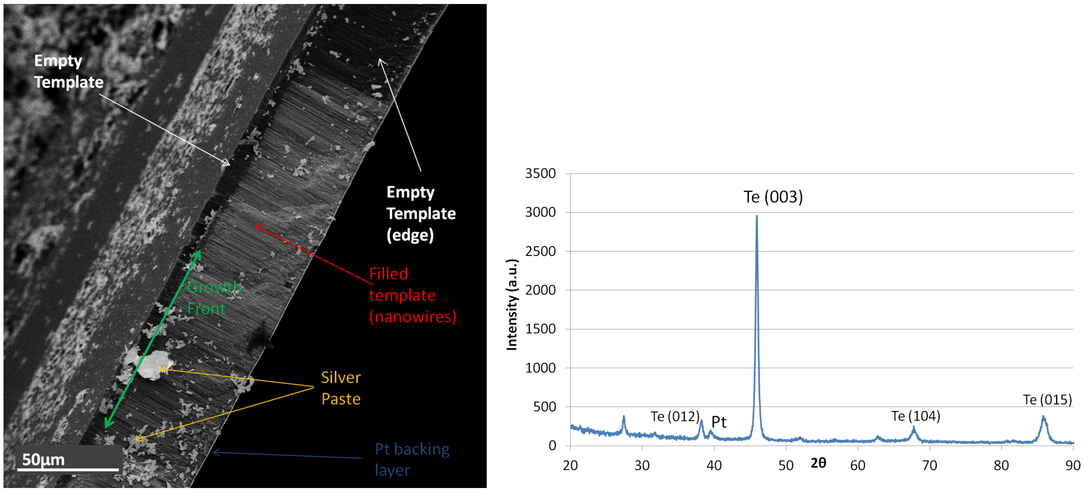

(c) BS-SEM of 1.15% Sb doped tellurium nanowire array (d) XRD of 1.15% Sb doped tellurium nanowire array

Figure 3.3

solution was used, and resulted in a 1.15 at% antimony; not taking into account changes in density, but correcting for the wires only being ∼55 µm long, the final solution would have about 3% less antimony than the original.

3.3 Analysis Techniques

Arrays were analyzed using a wide range of techniques. X-ray diffraction (XRD) was used as a quick check of composition, crystallinity and orientation; Electron microprobe was used to accurately determine the composition of the material; Scanning Electron Microscopy (SEM) was used to determine the filling and growth uniformity of the wires, along with the wire diameter and template thickness; multi-meters of varying accuracy were used for rough electrical conductivity measurements, or more accurate figure out merit calculations.

3.3.1 Sample Preparation for Analysis

After a deposition, samples were dismounted by first removing as much wax as possible, without harming the template, using a razor blade. A soak of many hours in acetone would follow in order to weaken the adhesion of the ThermalSeal^{TM} which could then be carefully removed with tweezers. It is important to do this with a delicate touch, to minimize breakage. Although samples are generally broken into smaller pieces for later analysis, it is preferred that this is done in a controlled manner, so the size and location (near an edge, through the middle, etc.) of the piece relative to the whole is controllable. A further acetone soak removed any lingering nail polish from the initial mounting and pore opening steps. Infrequently the template will still be attached to the copper support, even after the nail polish dissolution, by adhesion of the silver paste to the platinum backing. The most effective method of removal in this case is to run the razor or the ends of flat tweezers behind some edge of the sample. Repeated sweeps, each time going slightly closer to behind the center of the sample will eventually free the array. A razor blade could then once again be used to remove any remaining silver paste on the platinum side of the array.

Once removed, whole arrays were analyzed by XRD, as it is very informative while not requiring the sample to be changed (polished, broken or etched), and itself is non-destructive.

3.3.2 X-ray Diffraction

XRD analysis of a sample was done by mounting it on a film of petroleum jelly on the surface of a sample holder.

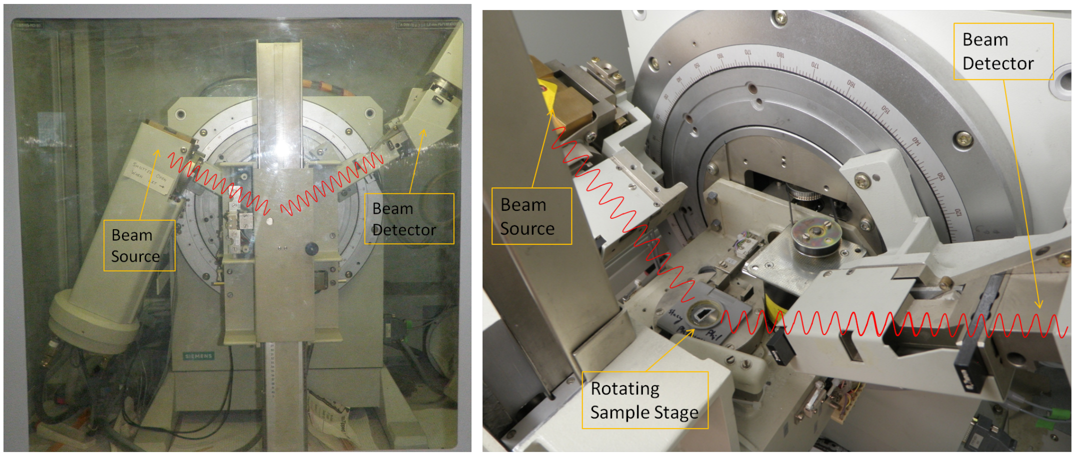

(a) Stacy group X-Ray Diffractometer (b) Sample on sample holder in the XRD

Figure 3.4

The XRD aims a coherent x-ray source at the sample at an angle, θ, while a detector is placed on the opposite side of the sample at the same angle. Constructive interference occurs at angles which satisfy the Bragg equation

$$n\lambda = 2dsin\theta \tag{3.1}$$

where n is an integer, λ is the wavelength of the radiation (1.54nm for a copper-Kα source), θ is the angle being scanned (as measured between the sample surface and the beam), and d is the atomic spacing for the lattice reflection.

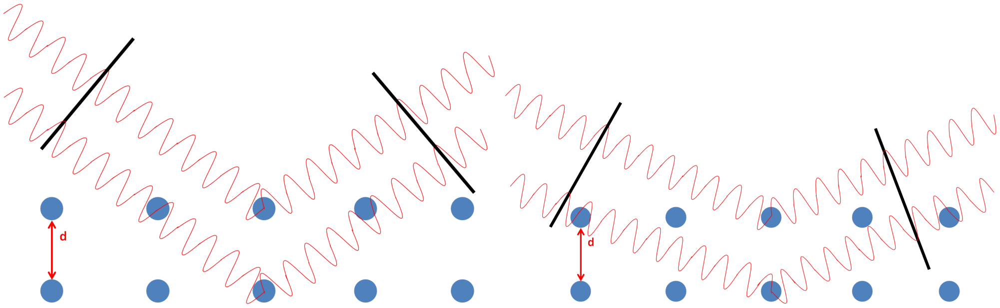

(a) At Bragg condition, the beam constructively interferes resulting in a large signal reaching the detector

(b) Away from Bragg condition, the phase of the diffracted beam is incoherent, resulting in destructive interference and little to no signal

Figure 3.5: Cartoons illustrating constructive and destructive interference due to Bragg's law

In cases where equation 3.1 is not satisfied, the phase of the diffracted beam will be shifted as shown in figure 3.5. Although the phase shift for two layers (figure 3.5) is not completely destructive, the diffracted beam will shift by the same amount for each subsequent layer of penetration

$$\sum_{n=0}^{\infty} e^{n*\Delta*i} = 0\{if\ \frac{\Delta}{2\pi} \notin \mathtt{Z}\} \tag{3.2}$$

Δ is the phase shift for each layer of pentration by the beam, and n is the number of layers. In this simplistic and idealized case destructive interference would result in no signal at any angle which did not satisfy equation 3.1; however, near angles that satisfy the Bragg condition the desructive interference will not be fully realized.

Peaks with non-zero width result from the non-perfect destructive interference which is observed in real samples. Real samples contain strain and other sources of non-uniform d-spacing; they also do not perfectly transmit photons, resulting in non equal weighting of different reflections. Furthermore, the beam and detector are not perfect points but have some physical size. Lastly, the samples contain crystalline grains that are not infinite in size, and thus contain only limited numbers of layers which can cause diffraction; in practice, this gives n, in equation 3.2, a finite limit.

While being scanned the sample holder is rotated in the plane perpendicular to the bisecting angle between the incident and reflected beams. For a powder sample this means every lattice spacing that satisfies the Bragg condition will be give a signal (fig 3.6a); for a single crystal only those lattice spacings which are parallel to the plane of rotation will give a signal (fig 3.6a).

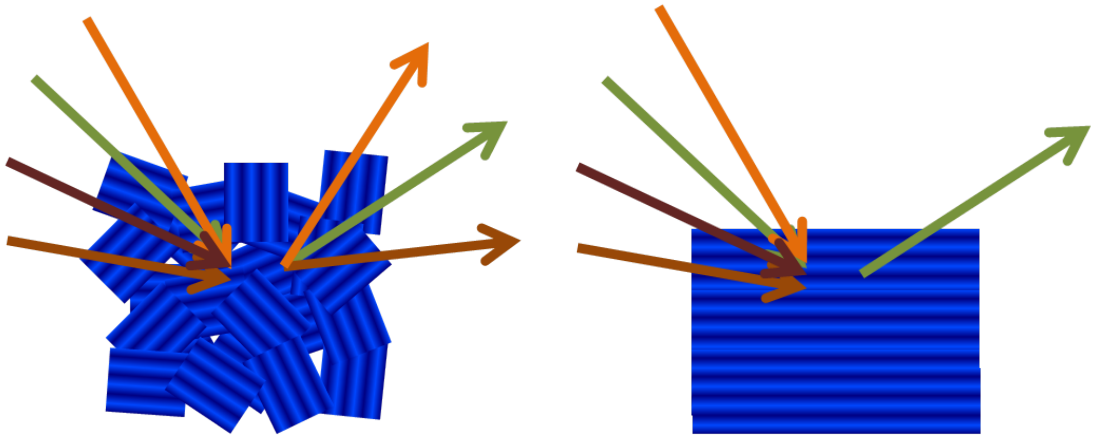

(a) Cartoon of a randomly oriented crystalline powder

(b) Cartoon of a single crystal

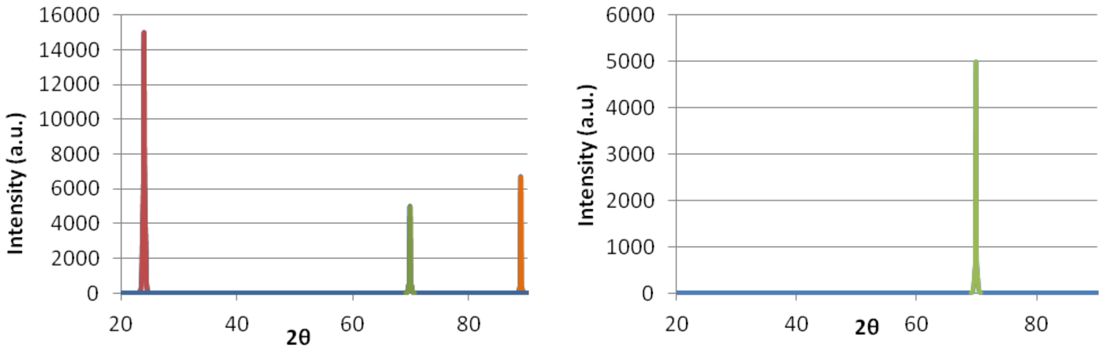

(c) A theoretical XRD pattern for the sample above

(d) A theoretical XRD pattern for the sample above

Figure 3.6: (a) Cartoon of a randomly oriented crystalline powder, and (c) its expected XRD pattern. (b) Cartoon of a single crystal, and (d) its expected XRD pattern

Similarly, an array made up of randomly oriented wires, or wires composed of randomly oriented grains will create a signal like that of a powder sample (fig 3.7a); whereas an oriented wire array will only result in the constructive interference of a limited number of reflections (fig 3.7b).

With this in mind, comparing relative peak heights to those of a theoretical (or actual) polycrystalline samples of the same material can elucidate the general orientation of the wires in the array. Relative crystallinity of the wires in the array can be determined by comparing peak heights, since only crystalline segments will result in significant constructive interference. Scans were generally done over 2 hours, scanning from $20^\circ < 2\theta < 90^\circ$. Longer

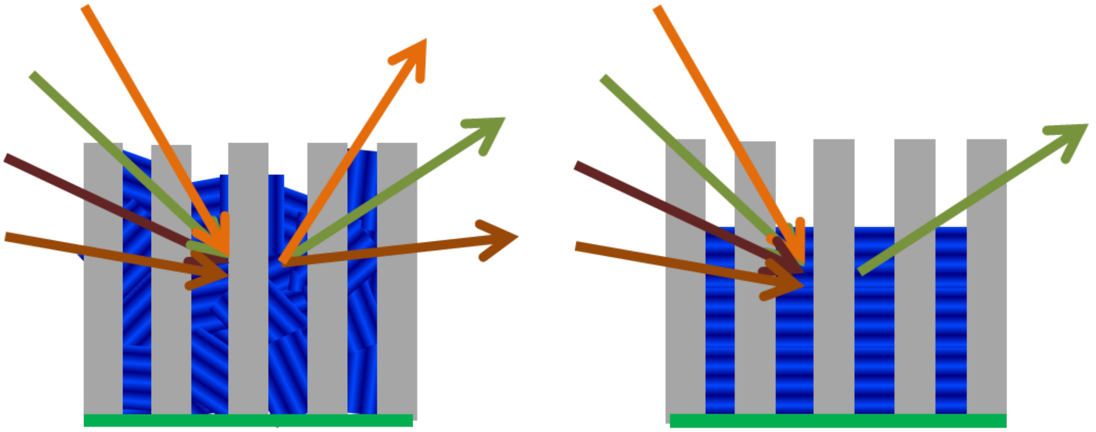

(a) Cartoon of a polycrystalline, non-oriented wire array (b) Cartoon of a crystalline, oriented wire array

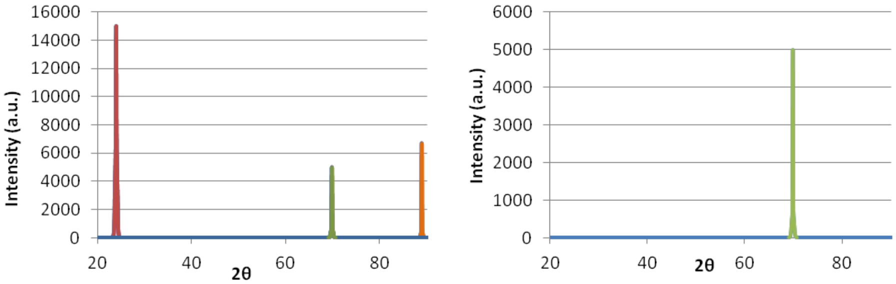

(c) A theoretical XRD pattern for the sample above (d) A theoretical XRD pattern for the sample above

Figure 3.7: (a) Cartoon of a polycrystalline, non-oriented wire array, and (c) its expected XRD pattern. (b) Cartoon of an oriented wire array, and (d) its expected XRD pattern

scans, or scans over smaller 2θ ranges were done when more distinguishable peak heights or positions were desired. By matching theoretical patterns, to those recorded, and by having knowledge of the starting materials in solution an identification of the material can be made. Furthermore, for alloys and substitutionally doped samples, we can approximate composition directly using Vegard's law; this law states that lattice parameters (and hence the peak position) will have a linear relationship to the fractional composition of each component.

All XRD data was done on our lab's own Siemens D5000 autmated XRD, which is pictured in figure 3.4a. For many samples XRD information was not sufficient, especially if an accurate determination of composition was required; in those cases the samples were analyzed by electron microprobe after removing the platinum backing.

3.3.3 Electron Microprobe

Although XRD can help determine the rough composition and structure of the array material, electron microprobe is needed to give a precise and accurate determination of composition. As microprobe is a surface technique which requires very flat samples, arrays were polished with the aid of a mechanical polishing wheel. Generally the samples were polished from the platinum side (the wire "bottom") where the highest wire density is found. Polishing was done by hand on a polishing wheel; an initial rough polishing to remove the thick platinum layer was done with a 6μm diamond paste. Once the platinum layer was removed, 3μm and then 1μm diamond pastes were used. A final polish, with a 0.05μm silica solution, was done to make the surface as flat as possible.

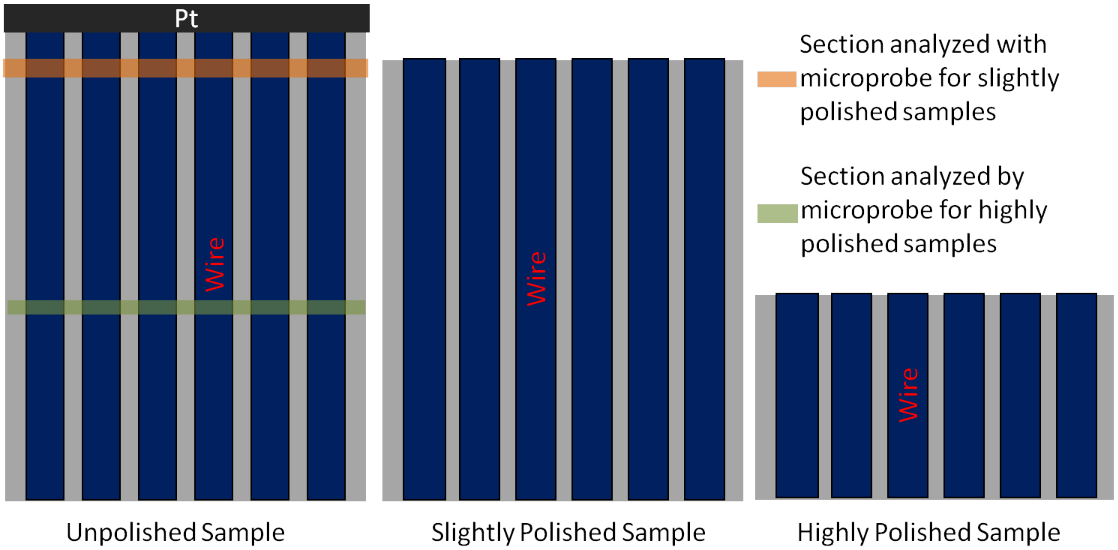

Figure 3.8: Cartoon of sample preperation for microprobe analysis along a wire array

Electron microprobe works by aiming a high energy electron beam onto the sample surface. There, electrons interact with and eject core electrons from atoms in the material; these newly formed vacancies are filled by higher energy core electrons which creates radiation as they fall to a lower energy state (fig 3.9). Due to the quantized nature of these electron states, the resultant radiation has characteristic wavelengths for each element. The different wavelengths that are observed come from the multiple combinations of electron ejection and emission. For example in fig 3.9, the ejected electron is from the K-shell and the emitting electron is from the M-shell; in this case the radiation would be considered Kβ. Further specification can be made between Kβ_1, Kβ_2, and so forth, where slightly different wavelengths are due to the slight energy differences between different subshells of the M-shell electrons (e.g. 3p and 3s). Similarly if the emitting electron were from the L-shell the radiation would be considered Kα, or it would be considered Lα if the ejected electron was from the L-shell instead of the K-shell.

One wavelength (for example Kα) for one element may be the same as another wavelength (for example Lα) of another element, however, the fingerprint of a set of wavelengths is unique for each element. The overlapping wavelengths are important to consider when choosing the appropriate wavelength to analyze in the ultimate signal analysis. Moreover, the impinging electron beam cannot penetrate deeply into the sample (penetration depth is dependent on beam energy and the elements in the samples), and so the signal only tells us about the surface of the sample being analyzed.

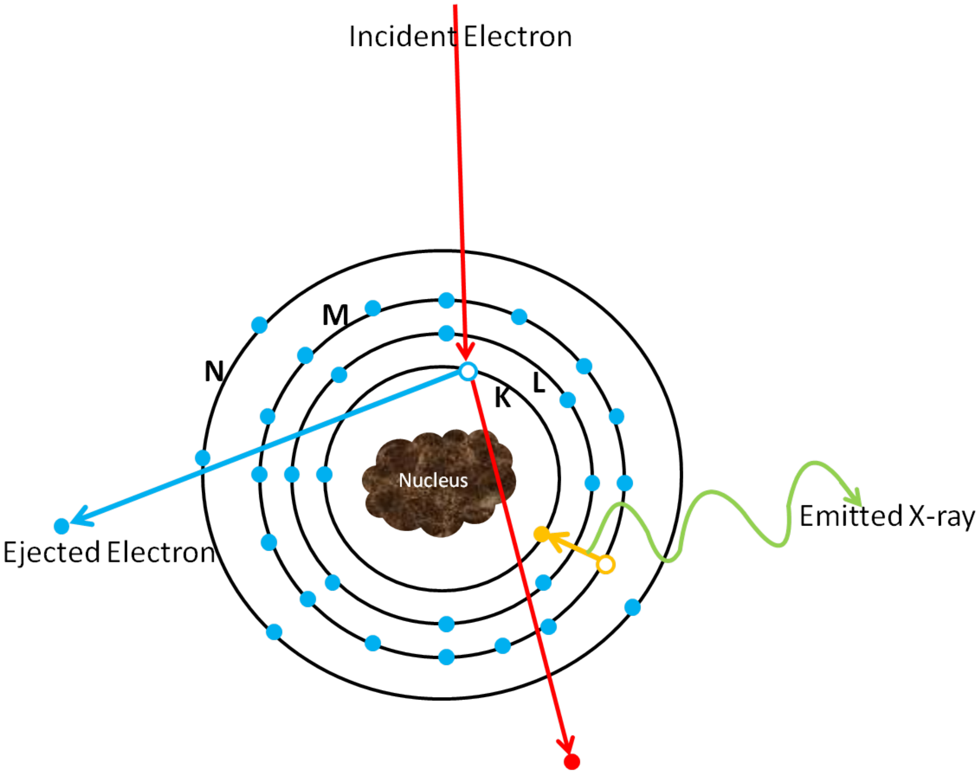

Figure 3.9: Cartoon of electron microprobe on the atomic level

By normalizing the signal for each element possibly present in the material against a standard, which contains that element in a known composition, highly accurate and precise elemental compositions can be determined.

Electron microprobe work was done by Kent Ross or Sean Mulcahy in the Earth and Planetary Sciences department here at UC Berkeley, or done myself (with assistance from Sarah Roeske) in the UC Davis Geology deparment.

Although these techniques (XRD and Electron Microprobe) are very informative, they dont give much information about individual wires. Pieces of samples were frequently also analyzed under SEM to get topological and dimensional information such as wire lengths, diameters, and filling percentages.

3.3.4 Scanning Electron Microscopy

Topological information was obtained using SEM, in which an electron beam is focused on the sample and rastered over a specific area. Inelastically scattered electrons with low energy (<50 eV) are considered secondary electron; electrons of this type do not typically escape from further than a few nanometers below the surface. The relative number of electrons escaping from any area corresponds appropriately to how the surface would look in a 2D representation, owing to the fact that edges and steep surfaces allow for electrons to escape more frequently.

Some electrons are elastically scattered and conserve most of their energy, these are backscattered electrons. The elastic scattering of backscattered electrons occurs due to the nucleus, and thus nuclear charge (Z) of the atoms being analyzed is critical; a higher Z value will elastically scatter more electrons, and result in a stronger signal. Although this is considered a surface technique, the signal is accumulated from hundreds of nanometers below the surface.

In most cases a layer of sputtered conductive material is needed; although the sample is grounded, there is a possibility that electrons will collect on the surface. This highly conductive covering prevents charging, which would create an electric field that could deflect the incident electron beam, resulting in falsely high numbers of deflected electrons (and false brightening in the image). Only a few nanometers of Pt are sputtered on; enough to allow for charge dissipation at the surface, but thin enough that the detected signal is mostly from the sample itself.

Backscatter images often prove more useful because the contrast between aluminum oxide and high-Z atoms (such as antimony and tellurium) is quite strong. The pore filling percentage can be determined by taking samples which were prepared for Electron Microprobe, and using imaging software to count the number of filled pores versus the number of unfilled pores.

Most SEM images were taken on one of two microscopes in the Berkeley Electron Microscope Lab (EML). Low resolution images, or samples which I did not want to sputter, were imaged with a Hitachi TM-1000 (e.g. 4.6); higher resolution images were taken using the Hitachi S-5000 and required sputtering to avoid charging as described above.

A small piece of the array, mounted on its side, can be used to image the cross section. Once again, the contrast between the two materials is crucial in the imaging; the uniformity of the growth front and the length of the wires can be determined by such a backscattered image.

3.4 X-ray Diffraction Data

Samples with a range of doping concentrations were grown by adjusting deposition conditions. As was discussed earlier in section 3.2.2, pulsing is important for uniform composition; for this reason most samples were grown by pulsing between an “OFF” potential of -400mV, where no electrochemistry occurred, and an “ON” potential, much more negative than the

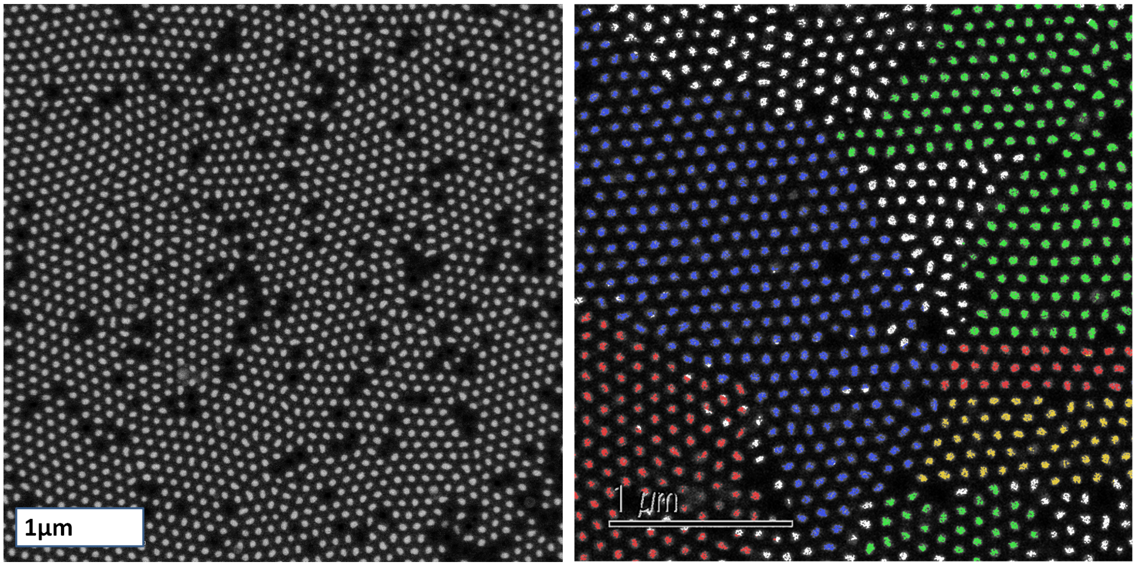

(a) Backscatter SEM of bottom of polished array. The bright spots are individual wires, the dark areas are the alumina template

(b) Backscatter SEM of bottom of polished array. The light spots are individual wires, the dark areas are the alumina template. Colors added, showing different grain boundaries

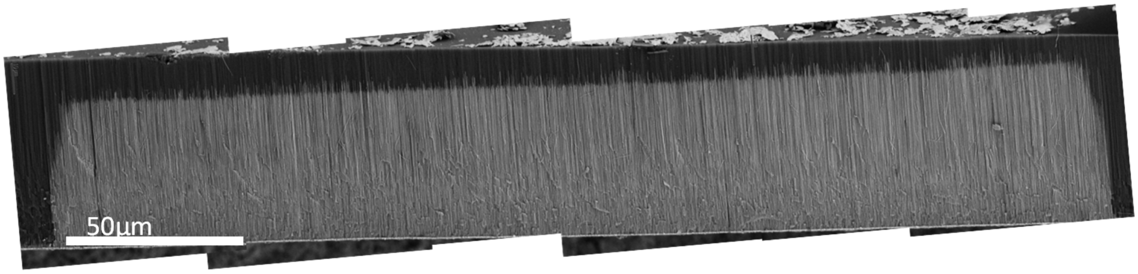

(c) Collection of backscatter SEMs of a single cross-section of an array

Figure 3.10

OFF potential. It is possible to deposit wires with a large range of composition, well beyond previously reported values [15, 76, 92, 16, 14, 1, 33, 96].

Antimony can dope tellurium in two ways different ways; as discussed in section 2.1.3, either the antimony could replace tellurium in the helical chains, or it could interstitially insert itself between chains. In the former case the average spacing in the c direction would be shortened by the smaller antimony atom, while the latter case would result in expansion in the x-y plane, as interstitial antimony would push chains away from each other.

If the antimony were to dope substitutionally, the d spacing in the x-y direction would remain unchanged, while the d spacing in the z direction would shrink[96]; the peak position for any z-dependent reflections would increase linearly with the doping concentration. If the antimony were instead to dope interstitially, the d spacing in the x-y direction would increase while in the z direction, remaining unchanged or slightly increasing[96]. In this case

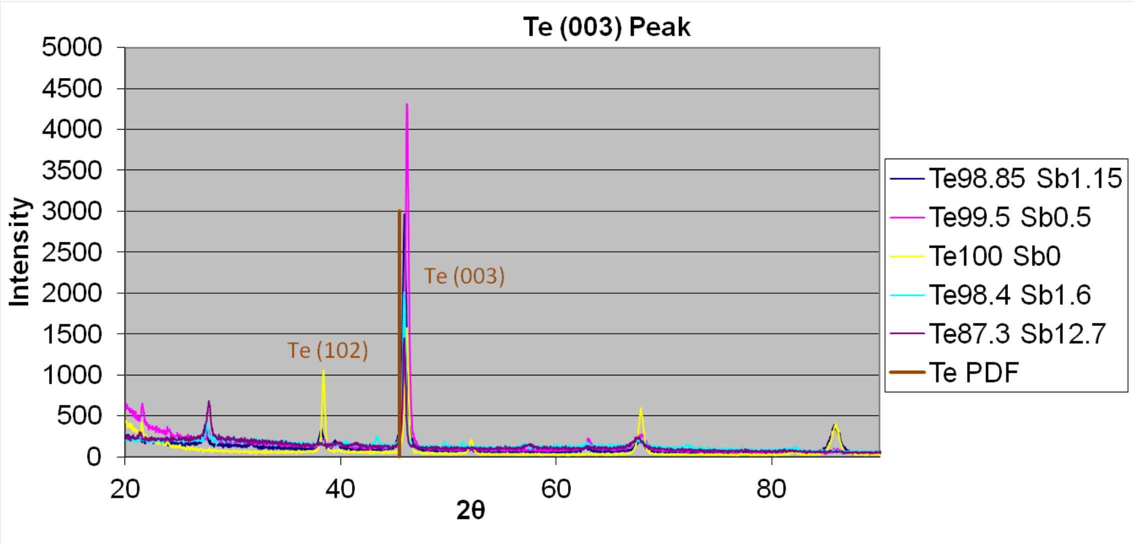

(a) Full XRD patterns of various samples

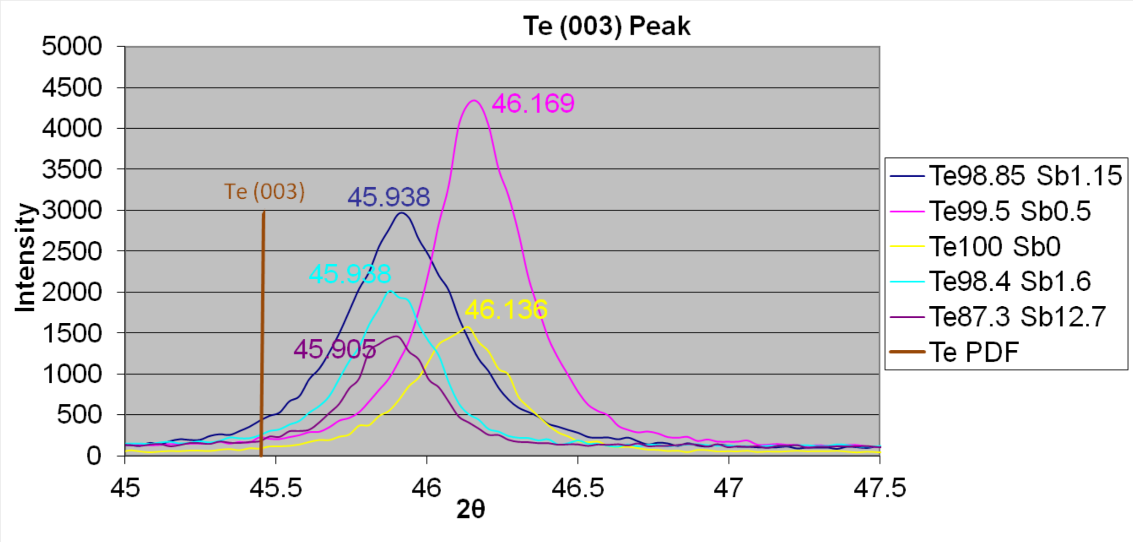

(b) XRD patterns focused on the region near the (003) reflection

Figure 3.11

the 2θ value for Bragg diffraction of peaks of the form (00z) would either decrease slightly or remain unchanged, while peak positions for all other reflections would decrease.

By focusing on a peak that is observed in most crystalline samples, any peak position trend or lack of trend can be observed. The (003) peak is just such a peak; many deposition conditions result in highly oriented growth in the (003) direction with a wide range of compositions. This orientation is seen in the XRD patterns of figure 3.11; although other peaks are seen in some patterns, the relative heights indicate a preference for the (003) growth

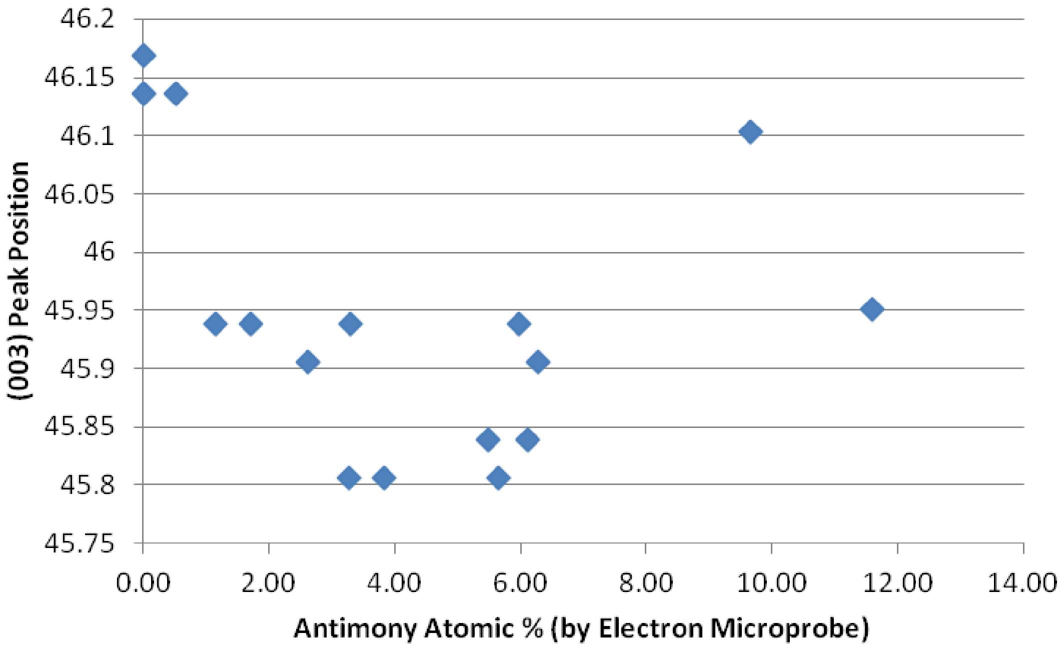

Figure 3.12: Plot of wire composition versus measured XRD peak position

direction.

A theoretical pattern predicts which peaks should be seen, as well as their intensity; for tellurium the powder diffraction file (PDF) shows that the intensity of the (003) peak should be about $\frac{1}{4}$th of (102) peak (table 3.1). Instead the (003) peak is consistently the highest; this is true even for pure tellurium (figure 3.11a) which is the least oriented sample shown. In fact, the (003) peak is 150% that of the next highest peak (the (102) peak) in the pattern, which is equivalent to 7 times as much crystalline material oriented in the (003) direction relative to material in the (102) direction.

As expected for interstitially doped arrays, there is no increase in diffraction angle peak

2θ	Int	h	k	l	2θ	Int	h	k	l
23.044	16	1	0	0	45.901	9	0	0	3
27.563	100	1	0	1	49.630	14	2	0	1
38.261	36	1	0	2	56.878	8	2	0	2
40.446	25	1	1	0	62.811	7	1	1	3
43.332	8	1	1	1	63.753	5	2	1	0

Table 3.1: Tellurium PDF #36-1542 for λ=1.54060nm (only peaks with relative intensity of 5 or greater)

position when compared to pure tellurium arrays (figure 3.11b). In fact, there is a slight decrease in the peak position which levels off quickly; this slight decrease is consistent with the slight increase in anti-bonding character of the tellurium bond after the addition of antimony (section 2.1.3). Weaker bonding should result in slightly larger tellurium bond lengths, larger d-spacing, and importantly a slightly smaller Bragg angle.

It would be beneficial to look at other orientations of the nanowire arrays, in hopes of tracking peak shifts for reflections caused by lattice spacings in the x-y planes. As our template geometry is like that of a thin wafer, the sample must be ground up using a mortar and pestle. Once coarsely ground, the resultant powder is mixed with a minimal amount of vaseline, and this dark goop is spread onto a sample holder. As is shown in figure 3.13, the relatively strong (102) peak is visible in samples of pure tellurium, while it is not seen in samples with any antimony doping. For antimony doped samples, both polished and unpolished samples were chosen to make sure the peaks were neither hidden nor interfered with by the nearby platinum peak. Composition was determined by microprobe which was done on the polished pieces themselves, and on separate fragments for those samples which still contained platinum.

It is hypothesized that the lack of signal in doped samples results from the interstitial antimony. Antimony between the tellurium chains would increase non-uniform bending and deformation of the chains (figure 3.14). The small (003) peak visible in one of the polished samples, further corroborates this hypothesis; there is enough randomly oriented and crushed sample to produce a peak of relatively small strength, yet no other peaks arise. This non-uniformity indicates that deformation is mostly limited to the interchain ordering, while the ordering along the length of the chain is mostly unaffected.

XRD analysis was used to identify that highly oriented, crystalline arrays of tellurium and doped tellurium were being grown; furthermore, the absence of a relationship between antimony doping and diffraction angle peak position supports the hypothesis that antimony is doping via interstitial inclusions. Knowing where the antimony is going is important, especially since it determines the majority carrier, but getting only random concentrations of antimony is insufficient; being able to tune the antimony concentration is equally important.

3.5 Composition Control

A key benefit of using DMSO for the deposition of antimony doped tellurium is control of the composition and orientation. The potentials applied, pulse times and solution profile can all be adjusted to grow a specifically doped array. Independent of composition there is an inherent drive for the electrodeposition to occur in the most conductive orientation. As expected tellurium is most conductive along the length of its chains, so there is a very strong (003) orientation for the electrodeposited wires.

Composition was determined by electron microprobe, as explained previously (section 3.3.3). For each reported measurement, multiple lines (5-10 points each) were taken at random points around the polished sample surface. These measurements of composition are shown to be uniform by the low standard deviations across each sample. The limitations of

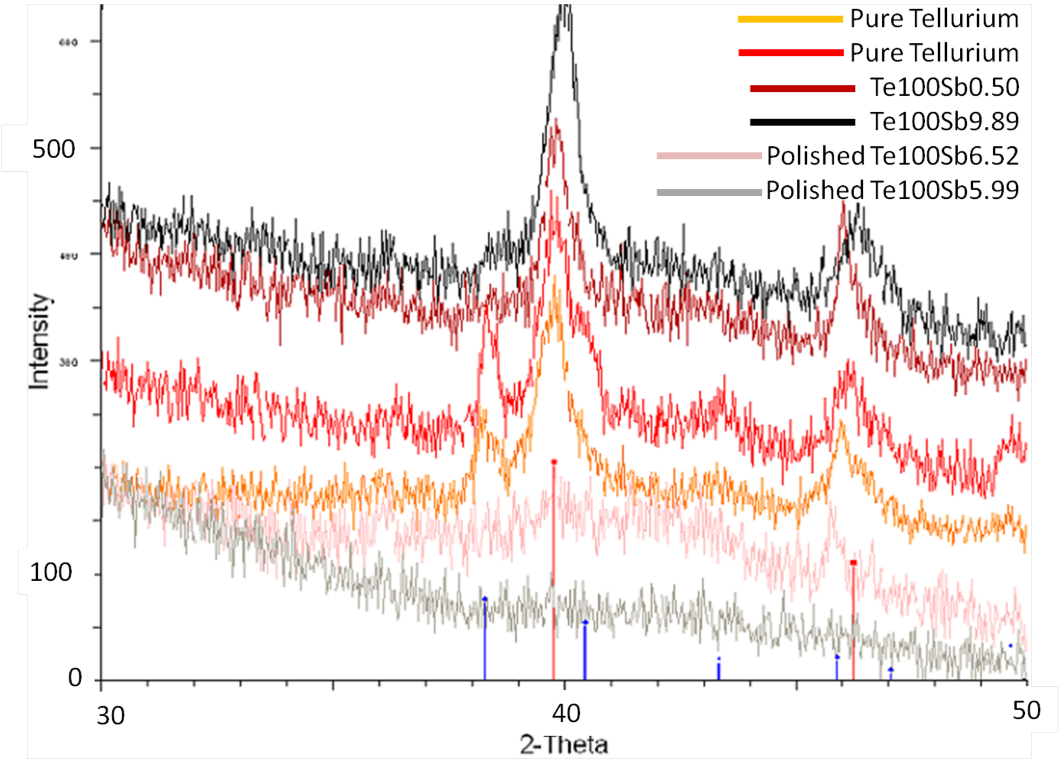

Figure 3.13: Collection of XRDs over a small range of angles, for samples that have been crushed by mortar and pestle. The samples include arrays of pure tellurium, as well as several antimony doped samples. The polished samples were polished minimally to merely remove the platinum backing layer before grinding them up. Samples have been displaced in the y-axis for better clarity, but the y-axis is scaled equivalently for all spectra. The red and blue lines give the theoretical peak positions for platinum (PDF #040802) and tellurium (PDF #361452) respectively.

detection are seen in data from a sample grown with no Sb in solution; the composition was determined have 100.11±0.13 at% tellurium and -0.11±0.13 at% antimony. Similar noise is noted in samples of low and high antimony composition. The sample presented in table 4.1 was similarly determined to have 1.15±0.1 at% antimony, while even a highly doped sample was measured as having 6.94±0.46 at% antimony.

Uniformity in composition along the length of the wire was not done specifically for tellurium samples grown in DMSO; however, past studies on arrays of bismuth telluride have shown that composition along the length of wires grown by electrodeposition is uniform. An array was grown and polished as described in section 3.3.3; the sample was then divided in half, and one of these halves was polished a second time. Reported as Bi_2Te_x, the first piece was found to have $x = 3.258 \pm 0.013$ while the twice polished piece was found to have a composition of $x = 3.260 \pm 0.018$.

This microprobe data highlights the uniform composition along individual nanowires,

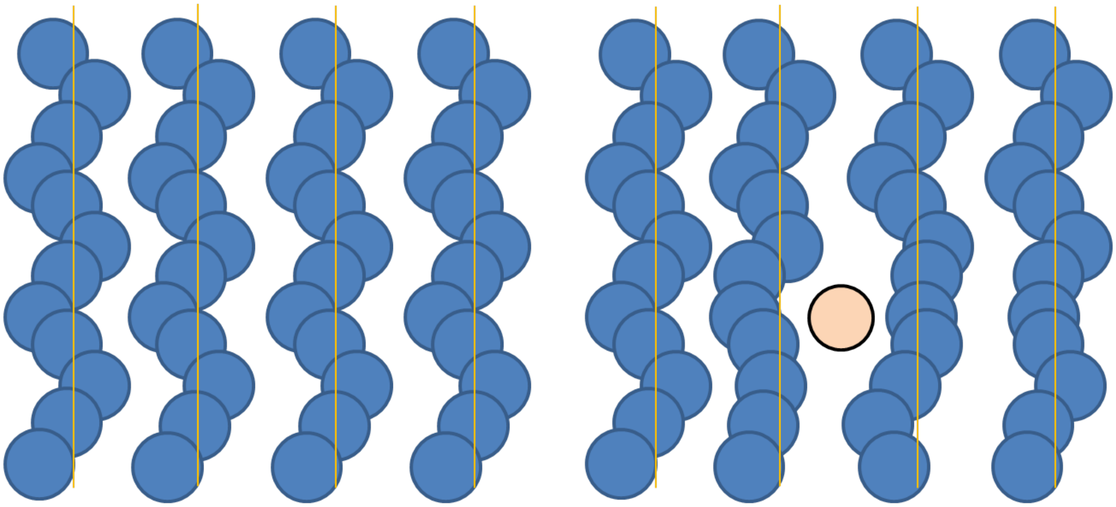

(a) Cartoon showing a side view of tellurium atoms in three-fold helical chains. Lines are included to highlight the uniform spacing in the x-y direction

(b) Cartoon showing a side view of tellurium atoms with an interstitially included antimony. Lines are included to highlight the lack of uniform spacing in this representative atomic ordering

Figure 3.14

and also between nanowires.

3.5.1 Solution Concentrations

The most obvious way to adjust the composition of deposited antimony doped tellurium wires is to adjust the solution concentrations of each species. A small change in antimony concentration, while all other deposition conditions held constant (table 3.2), results in a controllable shift in the eventual wire composition. Table 3.2 shows samples that highlight this controllability; each pair of samples were grown under the exact same conditions, except for a change in antimony concentration. As would be expected, an increase in the antimony

[TBACl]	[TeCl$_4$	[SbCl$_3$]	Wire Composition
0.3M	**15mM**	**4.0mM**	$\mathbf{Te_{100}Sb_{10.69}}$
0.3M	**15mM**	**1.0mM**	$\mathbf{Te_{100}Sb_{3.38}}$
0.3M	**20mM**	**4.4mM**	$\mathbf{Te_{100}Sb_{5.99}}$
0.3M	**20mM**	**1.0mM**	$\mathbf{Te_{100}Sb_{2.68}}$

Table 3.2: DMSO solution concentrations used for electrodeposition, as well as compositions (normalized to Te_1Sb_δ) as determined by electron microprobe. All samples above were grown by pulsing between -825mV and -400mV for 2 and 1 second respectively.

concentration resulted in an increase in antimony content in the nanowires.

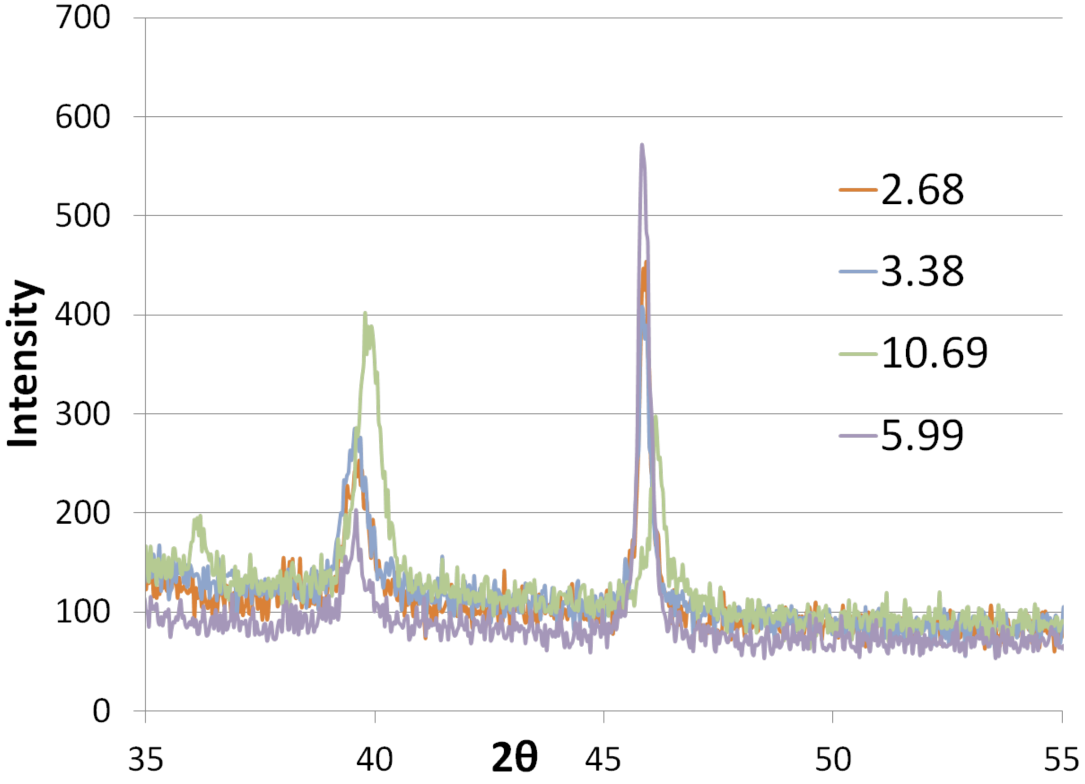

Figure 3.15: XRDs of arrays described in table 3.2, with the corresponding Sb content (as $Te_{100}Sb_x$) indicated for each plot

Coupled with a change in composition is a change in orientation. As is typical, high antimony content in the arrays accompanies a decrease in orientation. In the XRDs presented in figure 3.15, all samples are well oriented in the (003) growth direction when the expected relative peak heights (see table 3.1) are taken into account. This orientation is further reinforced when it is realized that these samples were grown for an excess of time (until overgrowth covered the surface of the whole exposed area). These XRD patterns were taken once the overgrowth was removed with a razor blade. This method is effective in removing most overgrowth, without damaging the template, but does not remove *all* overgrowth. Even when wires are supremely oriented, the overgrowth does not have a preferential deposition direction, and so the XRD pattern matches that of a powder sample. All of this works to somewhat decrease the apparent orientational preference of the wires in these arrays.

Despite all of this, the (003) peak is larger than the (102) peak for all except the most antimony rich of these samples, for which the peak heights are comparable. Although the low (102) peak height may result from poor uniformity in the x-y plane (section 3.4), as opposed

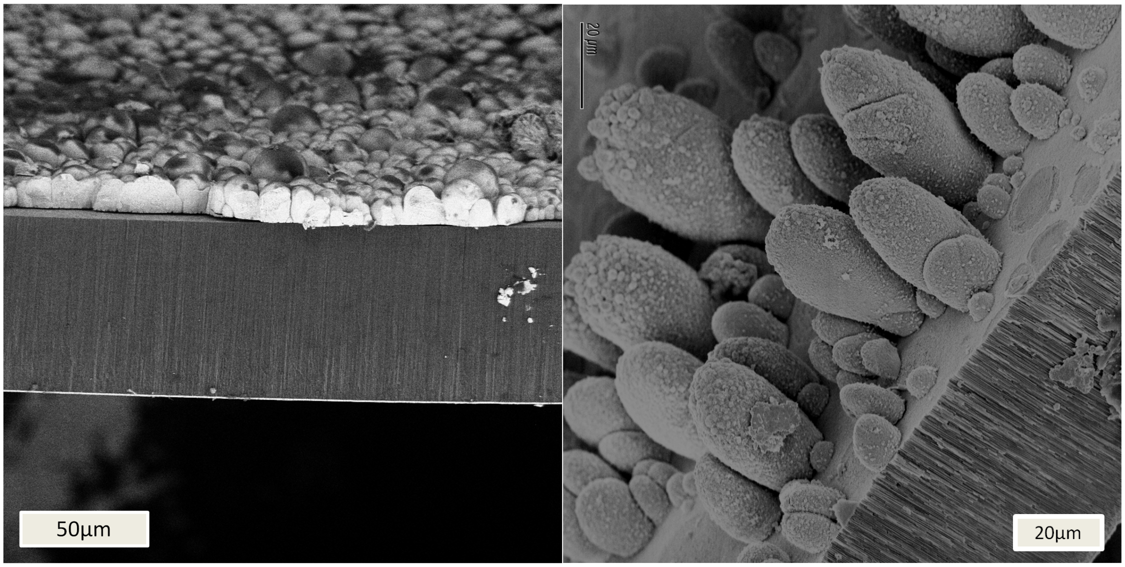

(a) (b)

Figure 3.16: SEM images for visual explanation of what is meant by overgrowth. The shape and density of the overgrowth depends on depositions conditions and the material being deposited. These images are of samples grown in aqueous solutions (a) bismuth selenium telluride (b) bismuth telluride

to strong orientation, there is nonetheless a significant (003) peak. Over a large, though limited, range of antimony doping, wire compositions can be achieved while maintaining a preference for the (003) orientation.

3.5.2 Applied Potentials

Apart from the solution concentrations, the potential profile is key to the resulting wire array. The first relevant aspect of the potential profile is pulsing, and the second the potentials themselves.

Pulsing is important in that it allows for uniform growth by slowing growth rate, and allowing the solution within the pores to re-equilibrate[95].

Applied poential also greatly affects the resultant array. At more negative potentials the fermi level of the working electrode is high, such that deposition can occur at sites of lower stability, and in non-crystalline positions. At more negative potentials a higher fermi level in the working electrode results in electrons of high enough energy for even unfavorable reduction events (e.g. figure 3.17). This is observed experimentally in the relative crystallinity and orientation which can be qualitatively compared by XRD. As shown in table 3.3 more positive ON potentials result in samples which have higher overall crystallinity; furthermore, the seemingly random orientation observed for the more negative potentials

ON Potential	(003) Intensity	(102) Intensity
-775mV	1244	307
-825mV	452	253
-850mV	386	245

Table 3.3: These samples were grown with 2 seconds at the ON potential (above), 1 second at the OFF potential (-400mV), using 100mL solution of 20mM $TeCl_4$, 1mM $SbCl_3$, and 0.3M TBACl in DMSO.

becomes very highly oriented in the (003) direction at relatively positive ON potentials.

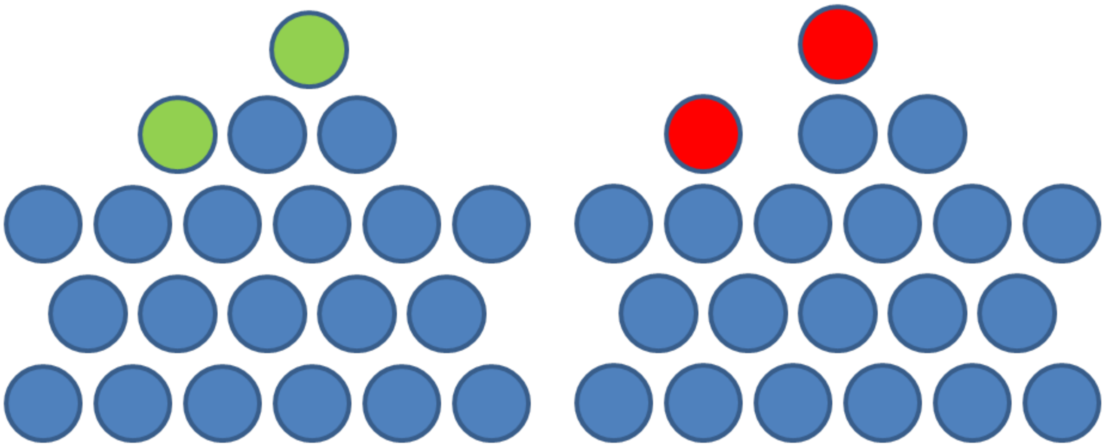

(a) Favored crystalline deposition possible at no overpotential

(b) Unfavorable amorphous deposition possible at large overpotential

Figure 3.17: Relatively favorable and unfavorable deposition sites shown by green and red respectively

For the antimony/tellurium system it is important to choose a positive potential so that the desired (003) direction is favored, while at the same time choosing a potential negative enough in order for both species to freely deposit. Through multiple trials, the optimal deposition potential is somewhere between -800mV and -825mV. At this potential both tellurium and antimony are easily deposited, there being a significant but not excessive overpotential for the deposition of each; at the same time, the overpotential is small enough that arrays show extreme tendency towards orienting in the desired (003) direction (section 3.4).

3.6 Conclusions

Electrochemical deposition into porous alumina allows for the growth of dense, electrically isolated, high aspect-ratio nanowires of all sorts of materials. The ability to grow such wires has been taken advantage of for a wide range of thermoelectric materials, to which pure tellurium and its antimony doped counterpart can now be added; however, being able to make nanowires is not in and of itself sufficient. Quantitative assessements of the properties of specific materials, in nanowire form, are needed in order to support or refute theoretical studies, and to direct future research. It is only recently that thermoelectric measurements have been made on nanowires, and those that have require specialized equipment, and lots of luck; there is curretly no way to measure nanowire properties without specialized equipment, however, the next chapter will describe how the need for luck can be removed from this process, and how easily measurements can be taken on individual nanowires. Furthermore, a variety of sample preparation methods for single wires and whole arrays will be discussed, as well as some of their difficulties, failures, and successes.

Chapter 4

Property Measurements of Nanowires

Previous chapters have been described the methods for understanding the underlying chemistry of electrodepositing antimony doped tellurium, as well as the practical considerations for performing these depositions. While antimony doped tellurium was previously a poorly understood system, bismuth telluride is one that has been well studied[21, 89, 22, 60, 104, 41, 84, 9, 98, 65, 49]. For this reason, during the investigation into the antimony-tellurium system in DMSO, property measurements were taken on not only anitmony doped tellurium samples, but also samples of bismuth telluride. Discussed in this chapter are the measurements taken on individual nanowires and whole nanowire arrays, both successfully and unsuccessfully.

4.1 Methods for measurement

There are three main schemes for determining thermoelectric properties of wires prepared by template assisted electrodeposition. Each of these methods requires a very different set of sample preparations, and each serves its own purpose. The first is to modify the template and/or growth conditions, such that only a few, countable number of wires grow. Measuring countable numbers of wires simplifies the contacting process, eliminating uncertainty or issues associated with contacting, while including the negative and positive affects of the template (extra thermal conductance, possible strain, etc.); however, it does not solve the question of how one would build an actual device with a full array. Actual devices (in most applications) will require many wires (a whole array), and such measurements can be done by creating a top contact to all of the wires at once. Any limitations in contacting a full array will result in a less than optimal device performance, but one which realistically represents how the actual device would perform. Lastly, individual isolated wire properties can be measured; these isolated wires give insight into the thermoelectric performance limits and physical properties of the wires themselves, decoupled from the choice of template or quality of contact methods. It is with these three techniques that the properties of the wires, the template, and the contacts can each be investigated.

4.2 Whole Array Measurements

As mentioned, measurements on full arrays of wires are important. These measurements give the full picture of how well or how poorly an array will perform as a practical device. All considerations, including the choice of template, contact resistances, and percent of wires contacted will be reflected in such a measurement. Furthermore, in order to utilize a thermoelectric device, a top and bottom contact is neccessary. By default, electrochemical deposition results in one contact; the wires must be electrically connected to the metal backing layer, otherwise they would not continue to grow. This leaves creating a good top contact.

4.2.1 Making Contact to a Whole Array

If contacts are to be made, it is not good practice to allow the wires to overgrow (grow above the template top). Growth outside of the template occurs much faster than in the pores for a variety of reasons. Once growth begins at the top of the template, growth can occur in all directions, creating a self reinforcing feedback loop; as more deposition occurs the overgrowth gets larger and larger (has more surface area) resulting in more and more growth (see section 4.3.2). This overgrowth is not inherently bad, but it will grow so large and so quickly that it will block solution from entering nearby pores. If all of these areas of overgrowth were contacted only a small fraction of wires would actually be contacted.

Removing this overgrowth mechanically (section 3.3.1) is possible, but has a few drawbacks for contacting. First of all, the mechanical strain may cause some wires to break, which is fine for XRD study, but results in an electrically open circuit. Furthermore, it is difficult to remove smaller areas of overgrowth even after multiple attempts. If these areas of overgrowth are left, then during etching of the template they will shield the template beneath them (as in figure 4.1), preventing access to a large number of wires, again resulting in low contact percentage. For this reason, depositions are ideally stopped just before the start of any overgrowth (exemplified in figure 3.3).

The most straightforward method for making a contact to wires within a template would be to etch away a small amount of the template, but only enough so the ends of the wires stick out; next, nickel (or another metal which forms an ohmic contact with the material) can be deposited onto the wire tips electrochemically. The nickel coated wires can then be put in an electroless nickel bath, resulting in a thick layer of nickel with all the wires embedded in it. This electroless deposition is reliant upon a redox couple in solution, particularly dimethyl ammonium borate (DMAB) and the nickel cations. Finally an electroless gold bath gives a highly stable top layer of gold which can be contacted macroscopically by solder; the gold deposits by the reduction of stabilized Au^+ and the oxidation of surface Ni atoms [61].

Alternatively, slight modifications to this general approach can be made. Other metal pairs (besides nickel and gold) can easily be substituted, although for bismuth telluride and tellurium, nickel is the best choice. Growth can also be stopped prematurely, followed by the nickel electrodeposition; this results in nickel tipped wires which will be exposed when the template is etched.

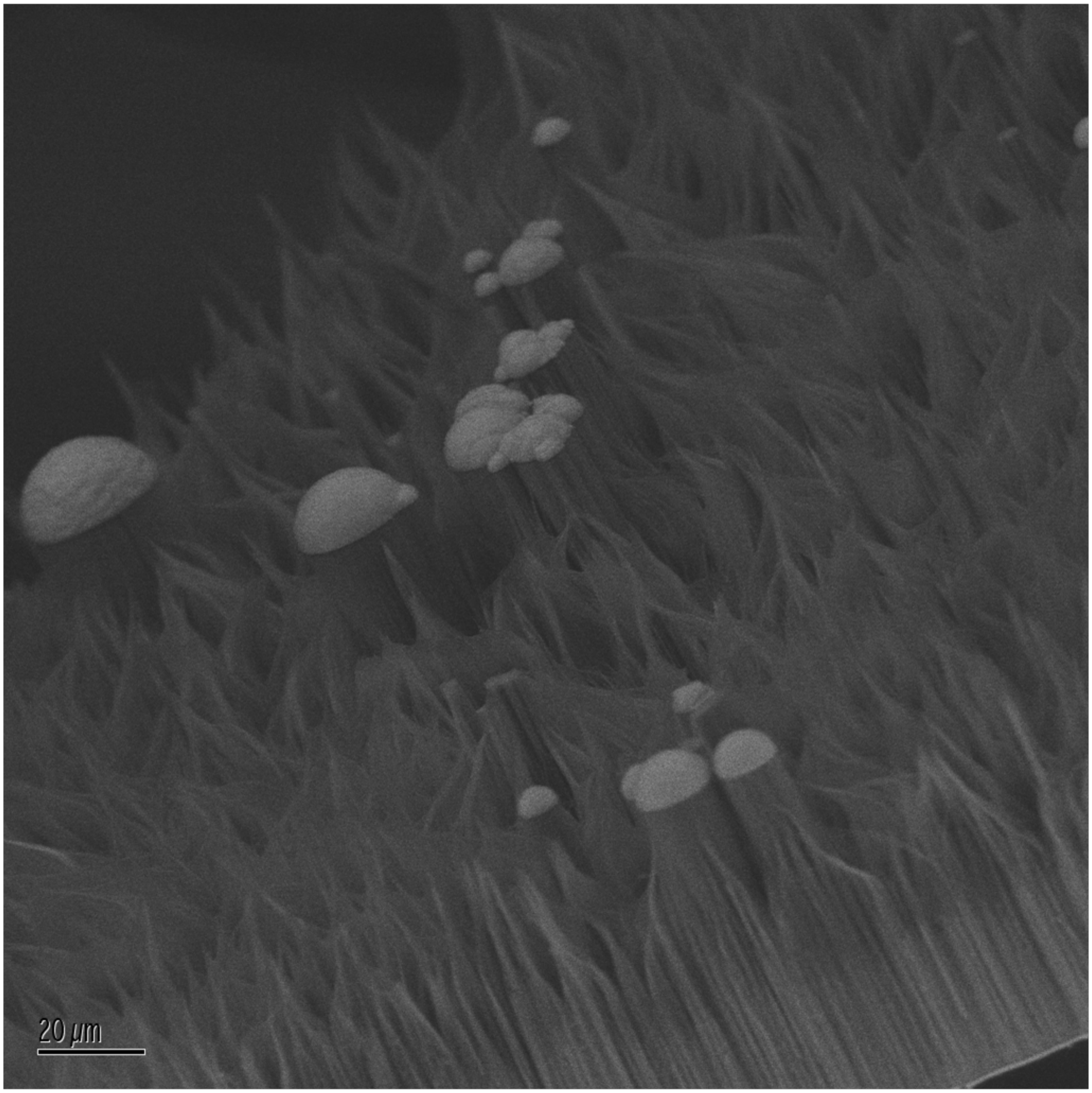

Figure 4.1: SEM of an overly etched template. The overgrowth has protected the alumina below it, resulting in towers of unetched template.

It is uncertain why this seemingly straightforward methodology has caused such difficulty, but it continues to be a hurdle for array measurements. Despite trying many different methodologies, conditions and preparation techniques resistance measurements on arrays are consistently higher than they are expected to be, often by many orders of magnitude; furthermore, these discrepancies themselves are inconsistent, even between different preparations of the same samples, which suggests it is not merely a result of wires which are poorly conductive. One possible reason may be that the conditions for nickel deposition result in poor coverage (the nickel onlu deposits onto a small fraction of wires), though SEM imaging does not support this (see figure 4.3). Alternatively, the exposed wire tips may be prone

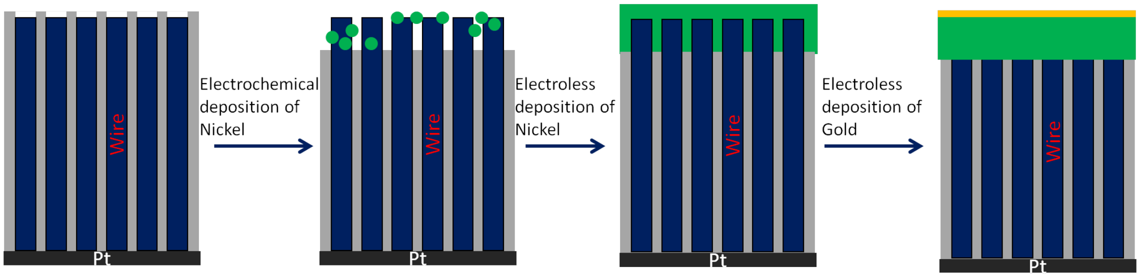

Figure 4.2: Cartoon of the stages for contacting a whole array with nickel and gold

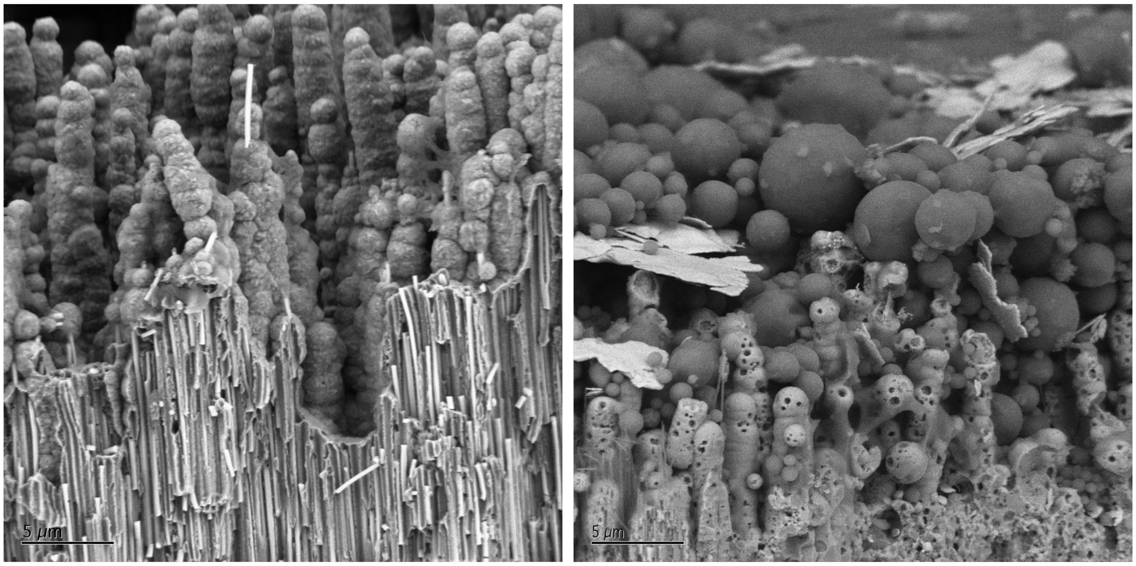

(a) (b)

Figure 4.3: Cross-section SEM images of two arrays which were etched and then coated with nickel through electrodeposition and then with an electroless nickel deposition.

to breakage once they are no longer supported by the alumina, causing breaks which would result in fewer electrically connectd wires.

Being able to make contacts reproducibly to whole arrays is an avenue of research that deserves attention, and which has yet to be solved. Some samples have yielded low enough resistances to make their measurements worthwhile; albeit with no resolution as to why these samples turned out better than others, and with the understanding that these measurements may be poor due to contacts which are neither comprehensive across the array nor ohmic. Despite this, in cases where resistances were within an order of magnitude of what would be expected based on bulk, measurements were taken.

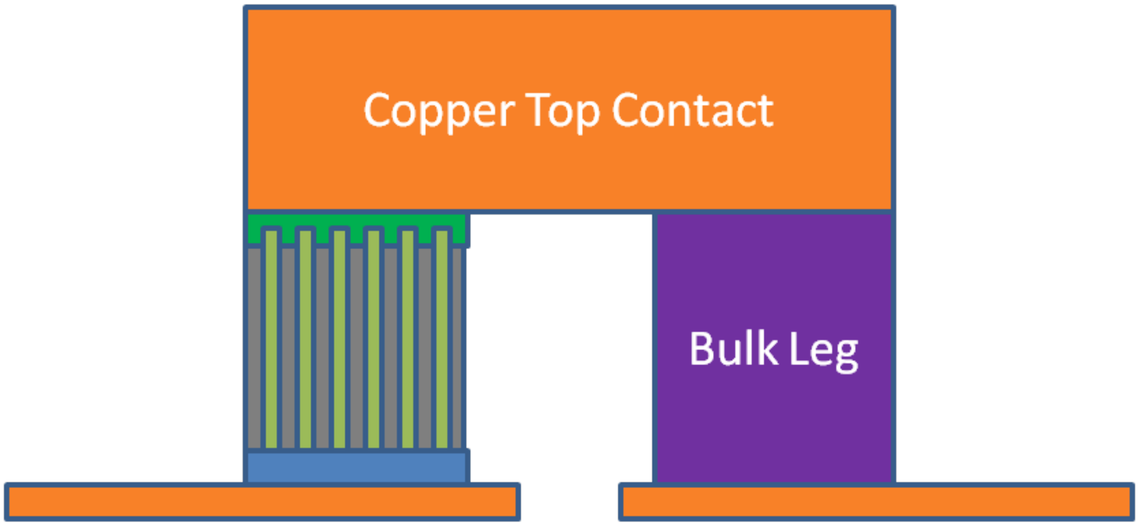

Figure 4.4: Cartoon of a hybrid nanowire-bulk device

4.2.2 Preparing Measurements on Whole Arrays

In order to get a full suite of thermoelectric measurements, two pieces of each sample are needed (equation 4.2); the sample of interest needs to be matched to both an n-type and a p-type bulk leg. To get multiple similar pieces, however, samples are diced into 380 µm by 380 µm squares. The dicing procedure could cause damage to the wires or contacts, so some samples were only measured by soldering directly onto the gold and platinum of a whole large (typically ∼1cm^2) piece.

4.2.3 Measurements on Whole Arrays

Measurements were made on one large piece of an array of pure tellurium, and on two sets of couples of diced antimony doped tellurium (1.15 atomic% antimony). Contacts were soldered to the platinum backing and the deposited gold layers; once soldered, AC resitance (ACR), and DC resistance (DCR) measurements were taken with a multimeter. Although the antimony doped tellurium pieces are from the same original sample, the differences in measured properties can be attributed to different contact methods.

Table 4.1 shows data from three different samples. The first is an array of pure tellurium nanowires, which was a piece broken off of a whole array, but separated from the rest of the sample *before* performing the nickel and gold contact procedures. The low ZT is not surprising as this sample has no doping; bulk samples of even optimally antimony doped tellurium have a maximum ZT of around 0.5[87]. As the thermal conductivity of the PAA is relatively high, and it does not contribute at all thermoelectrically, this ZT is neither encouraging nor discouraging. Measurements on the wires outside of the template are neccessary to determine if the poor performance is actually the wires, the combination of the wires in a thermally conductive template, or even just a poor electrical contact.

Sample Composition (determined by EMP)	Bulk Type	DC Resistance	AC Resistance	Seebeck Coefficient	ZT
Pure Te	-	65.1mΩ	64.0mΩ	-	0.017
1.15% Sb	N-type	25.07, 32.95mΩ	23.20, 30.60mΩ	-9.26 $\frac{mV}{^{\circ}C}$	0.077
	P-type	33.31, 36.22mΩ	30.45, 33.25mΩ		0.092
1.15% Sb	N-type	57.6mΩ	56.0mΩ	-35.4 $\frac{mV}{^{\circ}C}$	0.0298
	P-type	57.3mΩ	54.0mΩ		0.0589

Table 4.1: ACR and DCR data as measured by collaborators. The pure tellurium sample was not matched with a bulk leg as there was only one piece analyzed. Each resistance value is an average of multiple measurements of a single device couple. Multiple samples matched to the same type of bulk leg, with first DC resistance value presented coming from the same device as the first AC resistance value (e.g. the 25.07Ω DCR and 23.20Ω ACR come from a single device). The Seebeck coefficients were measured by combining ACR and DCR value from the same sample but matched to different bulk types. The ZT values are calculated from the ACR and DCR using the Harman method[40]

The two slightly doped samples shown in table 4.1 come from two different contacting methods (though both consisting of a nickel contact followed by a gold contact) on pieces from the same original sample. For each preparation a phosphoric acid etch was used to expose wire tips; this acid etch was followed by a pulsed deposition (-1V for 2 seconds, followed by -0.5V for 3 seconds) to coat the wires in nickel. The nickel coated wires were then further covered in nickel through a warm electroless nickel bath. At this point one sample was put in an electroless gold bath (the third sample in table 4.1), while the other had gold electrolessly deposited right before measurements were taken, many day later (the second sample in table 4.1). From each of these two preparations, a collection of pieces were diced into 380 µm by 380 µm squares. These squares were connected to conductive copper pads with solder and coupled to a bulk leg with known thermoelectric properties and dimensions (figure 4.4). Samples were screened by measuring DC resistance, and accepting any samples that had reasonable (low mΩ) resistance. Those acceptable samples had their AC resistance measured as well, and from the compilation of DCR and ACR matched with an n-type and a p-type bulk leg, Seebeck and ZT values were obtained. The ZT was determined using the Harman technique[40]

$$ZT = \frac{V_\alpha}{V_\rho} = \frac{R_{DC} - R_{AC}}{R_{AC}} \tag{4.1}$$

V_ρ is typical IR drop, and V_α is the Seebeck voltage. When AC current is applied, the Peltier effect is negated as an equal current flows in each direction; when a DC current is applied the normal Peltier effect is realized and the resulting temperature gradient will alter the voltage across the sample. Thus, by scaling for current, the V_α can be determined by the difference in the DC and AC resistance of the sample. As these ACR and DCR values are for the whole couple, and not just the nanowire leg, the choice of bulk leg pair will affect the measured ZT. A pair of legs with the same majority carrier type will perform worse than a leg of differing majority carriers, since two legs of the same type will be working against each other (one will be cooling the same side the other is trying to heat).

The sign of the Seebeck coefficient can be determined by comparing the two ZT values; as noted above, two legs of the same type will perform poorly since they are working against each other. So as long as the bulk legs which get paired with the sample of interest are reasonably similar (but of opposite types), the pair with a lower ZT will be of the same type. A more accurate Seebeck coefficient can be obtained either directly, by measuring a change in temperature or voltage by applying a gradient of the other, or indirectly, by manipulating the ZT formula.

$$S = S_{bulk}\sqrt{\frac{|ZT_P - ZT_N|}{ZT_P + ZT_N}}[71] \tag{4.2}$$

This calculation relies on each of the bulk legs having similar electrical properties, and equal but opposite Seebeck coefficients. For this reason, bulk legs that fit this description were used for taking our measurments.

Although neither of these device couples has a very high ZT, it is interesting to note how much the contacting method affects the performance. By changing the contacting recipe, the same sample, when put in the same device, has a figure of merit about twice as large as that of its counterpart.

It is also important to realize that the 1.15% antimony is well above the ideal doping concentration in the bulk, which is closer to 0.5%; one of many ways to increase performance would be to make a less doped sample. Although this can be done, it is not worthwhile until a reliable contact and measurement scheme is devised. These issues mean that the magnitude of the Seebeck coefficient may be falsely low, but do not refute that the sample is indeed n-type. A negative Seebeck coefficient further confirms what was supported in previous chapters, that antimony is (at least preferentially) interstitially, and not substitutionally, doping the tellurium.

Limited reliability in these types of measurements prompted other approaches to growing and contacting nanowires in PAA. In particular a novel growth method developed for DMSO, in which a handful of nanowires could be grown at once, using the same PAA templates used for whole arrays.

4.3 Pseudo Single Wire Measurements

Although measurements of a whole array are important, it is also important to know the physical properties of the individual wires themselves. One approach is to grow a multiple samples, each with countable number of wires, in templates of different thicknesses (to account for contact resistances). As these wires are still embedded in the template they are grown in, any changes or influences to their properties caused by the template will still be measured, and so theoretical predictions of a full array that is fully (or partially) contacted can be accurately made. A method for growing sparse nanowires has been previously described[13], but the mechanism proposed therein would make such a process impossible in DMSO. Instead a method was found to grow spare wire arrays in DMSO, the mechanism of which is only partially understood.

4.3.1 Method for Making Countable Wires

When growing whole arrays the porous alumina is prepared as in figure 3.1a. This procedure can be slightly modified by stopping after the second anodization and mounting the template as is [13]. In this case the pores are open at the top, while at the bottom there is a small barrier layer of alumina between the bottom of the pore and the metallic aluminum. It is proposed that etching at the pore bottom opens up sites for wire nucleation. Once a wire has been nucleated at the bottom of a pore, it is electrically tethered to the backing aluminum metal, and growth proceeds as normal. Those wires which get an early start will fill the pores relatively quickly and then overgrow (unconfined by the PAA matrix) at an increasingly faster rate; this overgrowth will block neighboring pores, preventing nearby wires from reaching the surface and overgrowing themselves. In this way the few nucleation sites result in even fewer overgrowth sites, few enough that they are countable under either an optical or electron microscope[13].

4.3.2 Growth of Sparse Wire Arrays

This growth method works extremely well in aqueous solutions for nickel and copper, but fails for silver; in order to grow silver nanowires by this method, a seed of nickel is created by a long soak in a nickel sulfate solution, and then the silver is deposited into the prepared template[13]. The mechanism in aqueous solutions is believed to rely upon acidic etching of the aluminum oxide barrier layer. In DMSO there is no acid present, yet counter to this, using DMSO as a solvent, and without a pre-soak, sparse wire arrays *can* be deposited.

It is obvious to wonder whether the mechanism is analogous to that in aqueous, or coincidental and completely different. Understanding the true mechanism would surely be worthwhile for performing depositions from other non-acidic or even other non-aqueous solutions. Although this question has not been answered, a hypothesis is that chloride in solution could be assisting in alumina dissolution, as $[\mathrm{MCl}_x]^{+n}$, or as dimethylchlorosulfonium by reaction of the DMSO with chloride in solution (similar to the Swern oxidation intermediate[73]). Further study is required to elucidate the mechanism, but in the meantime, it can still be used for growth of sparse nanowires.

One observation is that an overpotential was required for wire deposition. In fact, an overpotential was required even after nucleation had occured. This was confirmed by looking at different potential profiles during deposition; the most important of these are summarized in table 4.2. When a normally sufficient potential, for deposition of tellurium (-825mV), was applied for extremely long lengths of time, no growth was observed. On the other hand,

Time at -1100mV (per cycle)	Time at -825mV (per cycle)	Result
1 hour	n/a	Growth
1 hour	1 hour	Growth
3 minutes	4 hours	No Growth
n/a (constant)	1 hour	No Growth

Table 4.2: Conditions used to grow tellurium sparse nanowire arrays in aluminum backed porous alumina. All depositions were left for at least 100 hours (or until overgrowth was visible), and are presented as potential versus a Pt wire reference electrode.

when a more negative potential (-1.1V) was applied, overgrowth was always seen. Interestingly, if nucleation was promoted by brief pulses at -1.1V, followed by long periods at -825mV, no overgrowth was observed. This suggests that even after nucleation, an overpotential is required for deposition. If the pulse lengths were comparable in length, deposition could occur during the more reductive (-1.1V) pulses, and eventually overgrowth would be observed. In the cases in which pulsing was performed, it was qualitatively observed that fewer hemispheres of overgrowth were found.

An overpotential is needed, even after initial nucleation, for wire deposition; otherwise even short pulses to nucleate pores, at -1.1V, would be sufficient for growth at regular potentials. Further evidence for the need of an overptential was found when subsequent deposition of nickel, into templates with overgrown tellurium, showed no nickel deposition on the overgrowth themselves (figure 4.5). The overgrowth remained unchanged, and were not coated by nickel; however, nickel itself deposited in other pores. Seemingly, nickel growth occured as it would in a fresh template, but only in accessible pores, those in which tellurium nucleation had not begun.

The need for an overpotential when depositing sparse wires from DMSO, and the seeming lack of electrical connection between those wires and the backing aluminum, are starting points for understanding the mechanism for these sparse arrays in DMSO. While understanding the mechanism would be useful, it is also beneficial to determine which materials can or cannot be grown in this way; for this purpose, the three systems our group has studied thoroughly in DMSO (pure tellurium, doped tellurium, bismuth-antimony) were each grown by this method.

4.3.3 Tellurium Sparse Wire Arrays

Solutions of 20mM tellurium with 0.3M TBACl as the supporting electrolyte were made, and used to deposit tellurium into templates for sparse wire arrays. Deposition occurs whether or not a nickel soak is done preceeding the deposition, as long as a large overpotential is applied. Depositions at -800mV, -900mV, and -1V (versus a Pt wire pseduo-reference electrode) resulted in no visible overgrowth, and no measured current after multiple days of deposition; deposition did not appear to occur in cases where a nickel soak was done, as well

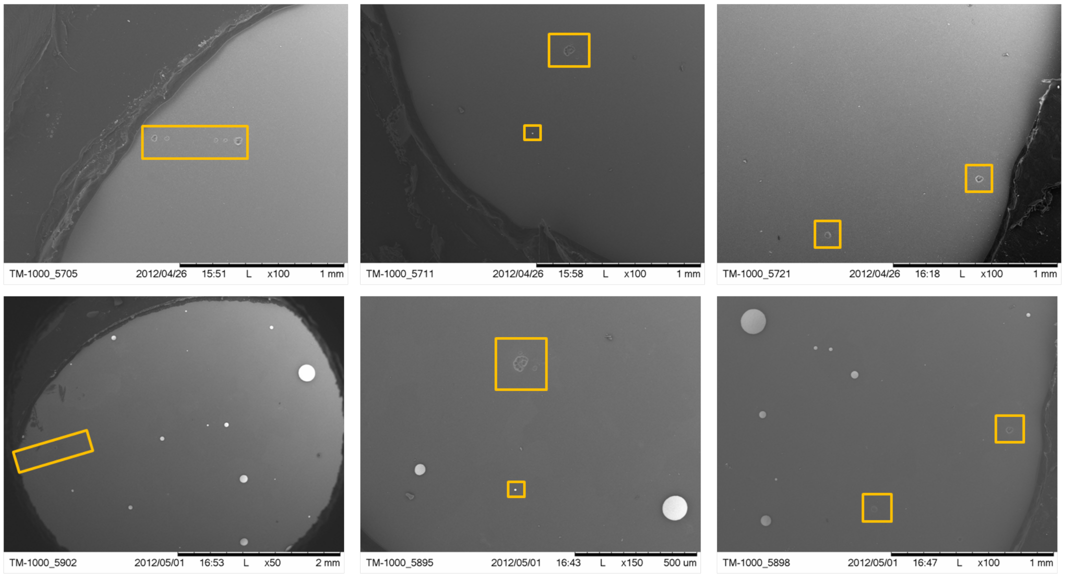

Figure 4.5: Low resolution SEM images of different areas across a single sample. The top row images were taken before a nickel deposition, while the bottom row images were taken afterwards. Selected features which appear in both images are boxed for clarity. The large bright spherical dots seen only in the lower row images are nickel nanowire overgrowths.

as when it was not. Depositions done at -1.1V (without nickel pre-soak) and -1.2V (with nickel pre-soak) also did not result in measurable current, but spots of overgrowth were visible on the surface (figure 4.6). The lack of measureable current is expected since the amount of material actually being deposited is around 10^{-8} to 10^{-9} times what is deposited in a similarly sized working electrode, whereas the current is only 2-3 orders of magnitude above what we can measure.

The overgrowth can be counted visually, but even small overgrowths can be definitively seen and identified by using a low magnification SEM (which does not require sputtering or other sample modification); once counted the macroscopic overgrowth can be contacted to perform measurements[13], which will be discussed in section 4.3.6.

4.3.4 Doped Tellurium Sparse Wire Arrays

Once it was determined that sparse arrays of tellurium could be grown, the next question was whether doped wires could be grown as well. By depositing from a solution of 20mM $TeCl_4$, 1mM $SbCl_3$, and 0.3M TBACl visible overgrowths were observered. Both of these point to deposition of some wires; however, due to the sparseness of the wires no compositional information was obtained. Confirmation of growth was obtained by looking at the samples under SEM, and seeing what must be overgrowth on the template (figure 4.7). These wires were considered doped tellurium (and not just pure tellurium), by the change in their overgrowth. The overgrowth observed when no antimony was in solution were perfectly hemispherical

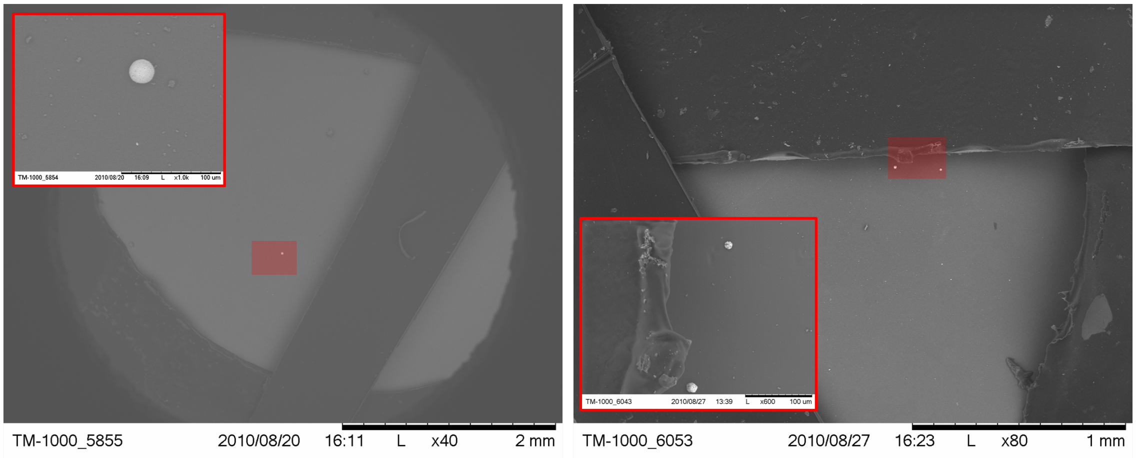

(a) Low magnification SEM of area with one overgrowth of tellurium, grown from DMSO without pre-deposition nickel soak

(b) Low magnification SEM of area with multiple overgrowths of tellurium, grown from DMSO solution after pre-deposition nickel soak

Figure 4.6

(figure 4.6); after adding antimony, the overgrowth grew in an abnormal bulbous fashion (figures 4.5 and 4.7.

Compositional determination by electron microprobe would require much large sample size, and although TEM would be an option, getting one of ten or so nanowires to be in the drops of solution placed on the TEM grid, and for that wire to lay in a desireable orientation for anaylsis was deemed too unlikely to be worthwhile. Full arrays grown under equivalent conditions would not neccessarily result in wires of equivalent structure and composition.

Knowing that pure tellurium or doped tellurium wires could be grown in this way, a next step was to further test the limits of this growth technique, and see if deposition could be done for systems besides tellurium.

4.3.5 Bismuth Antimony Sparse Wire Arrays

Bismuth antimony electrodeposition in DMSO has been previously studied by our group[52, 78, 66, 51]. The deposition of bismuth antimonide occurs over similar potentials as tellurium; similarly, an overpotential is needed to deposit sparse arrays of bismuth-antimony.

If an overpotential was applied, overgrowth was observed both visually and by SEM (figure 4.8). Bismuth antimonide overgrowth was identified by a unique flower-like topology, decidedly distinct from that of either tellurium or antimony doped tellurium. As with antimony doped tellurium, the composition was not determined for the same reasons; using XRD or electron microprobe would require more sample, and analysis by SEM or TEM on one of a few wires would be restrictively difficult.

There does not seem to be anything specific, which would limit this technique to only systems with tellurium, antimony, or bismuth; any material that can be deposited in DMSO

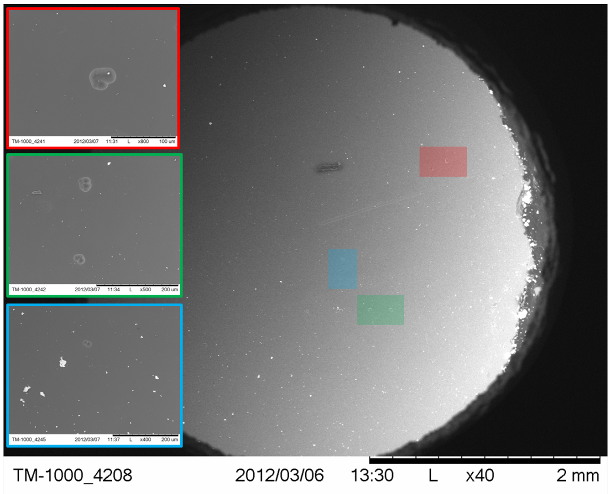

Figure 4.7: SEM images of overgrowth from a sparse array grown with tellurium and antimony in a DMSO solution

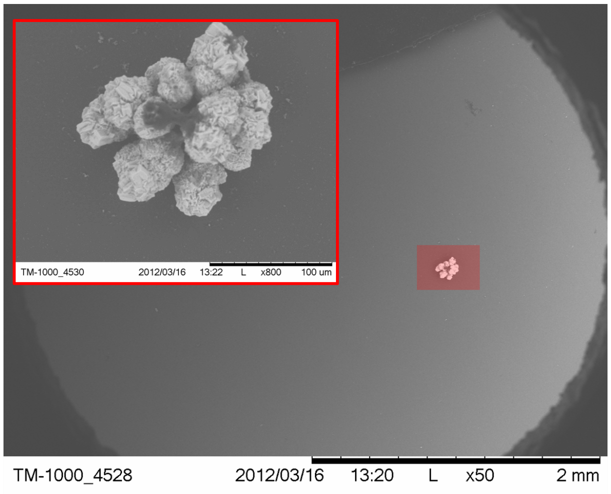

Figure 4.8: SEM images of overgrowth from a sparse array grown with bismuth and antimony in a DMSO solution

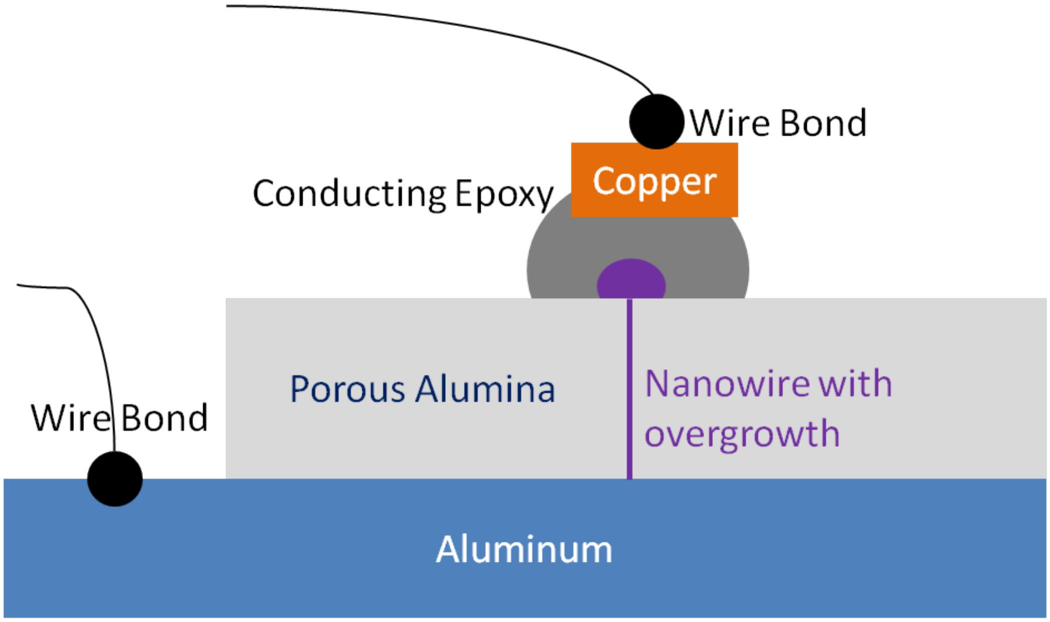

Figure 4.9: Cartoon of setup for PPMS measurements. The other end of the wirebonded wires are connected to pads on a puck which is designed to integrate into the specific PPMS being used.

would seemingly work. It may even be possible to extend this method to more solvents besides water and DMSO. Expansion of this method remains to be tested, but in the meantime, measurements were attempted on arrays of these materials.

4.3.6 Measurements of Sparse Wire Arrays

After growing sparse arrays of tellurium, areas were cordoned off using ThermalSeal^{TM}, and the number of overgrowth in each area were recorded (figure 4.6). Once counted, property measurements were attempted by placing a small amount of conductive epoxy on the area; a piece of copper metal was placed on top of the epoxy as well. A corner of the aluminum was then etched in acid or base for a short period. Wirebonding was done to connect the alumina and copper contact to pads on a small puck (figure 4.9). This puck was designed to go into a PPMS which would allow for electrical property measurements of the wire.

All measurements performed in this manner resulted in apparent open circuits. Initially this was attributed to excessive currents (either from multi-meter measurements, or due to electron discharge by the wirebonder) destroying the wires. Alternatively, it may be that the base of the wires themselves are insulated from the aluminum substrate, which would explain both the open circuit and the inability to deposit nickel onto overgrown wires (figure 4.5). This would also explain why an overpotential is neccessary for these depositions (described in section 4.3.2)

The pseudo single wire approach is very promising, as it allows for structurally supported, easily contacted single wires; unfortunately further research into the mechanism is needed before it can be taken advantage of fully for actual measurements. Although measurements on DMSO grown sparse wire arrays failed, measurements were successfully taken on individual wires which were removed from their template.

4.4 True Single Wire measurements

Traditionally, single wire measurements have not been done in a template, but rather by separating out a single wire and then contacting it with the help of a pattern. Usually this pattern is made with the use of masks and photoresist, and is intensive in time and resources. Although this is the case, free single wire measurements give physical information about the nanowire, completely decoupled from the template. As was stated earlier, the template plays a role in overall device performance; however, there is no reason to limit ourselves to measuring the performance of wires grown in the templates we know how to make today. It is reasonable to expect that other research will find a way to make thermally insulating porous templates, or a way to replace the alumina with an insulating material after deposition is completed. In this case having the knowledge of the properties of wires themselves and how these properties change with changes in composition, diameter, or orientation would be a critical step that could be determined before this template exists.

Contacting and measuring a single nanowire is non-trivial, and previous methods require not only specialized equipment but lots of luck. This section describes a novel methodology which removes any luck factor, though specialized equipment is still essential. In this section this method will be explained, and measurements taken will be discussed.

4.4.1 Nanowire Suspension

In order to make measurements on a free single wire, the first step is to get wires to disperse; considering that we start with highly dense arrays of high aspect ratio (>500:1) wires, avoiding clumping is important. As will be shown in section 4.4 a wire segment of at least 20 microns is needed. Since fracturing is common in the process of dispersing nanowires, templates with 60 microns in thickness are filled using well established electrochemical deposition conditions. The first step is the removal of the support structure around the wires, the porous alumina template. This can be done by placing an array in either a strongly acidic or basic solution. A solution of sodium hydroxide was chosen for its effectiveness and speed at dissolving alumina. A small piece (e.g. 2 x 2mm) of an array was broken and placed in a vial with approximately 5mL of 0.1M NaOH (aq). After only a few hours there are visible signs of the alumina dissolution. The Pt film that is sputtered onto the alumina is under a significant amount of strain; normally the alumina prevents the Pt from deforming, however, as it is dissolved away the Pt film will roll up like a scroll. Although this takes only a few hours, the samples are left in longer (typically 24 hours) in order to ensure all alumina is removed. The samples are then washed repeatedly with pure water. If the sample dries, wire clumping will occur, as the water has a high surface tension. To avoid this, subsequent washes are done by removing most of the liquid, but leaving enough so the sample is submerged; next the vial is filled with pure water and this process is repeated. From experience, 5 such washings are generally enough to remove all residue of NaOH and dissolved alumina. Once cleaned with water, isopropanol (IPA) is layered on top and the bottom water layer is removed. Further washings with IPA done in the same way as with the water, help to remove any residual water. At this point the wires are still attached to the platinum (which will roll up like a scroll) and submerged in pure IPA. Mechanical agitation is caused by stirring with a stir bar in the vial, and results in the breakage of wires. This process can be qualitatively observed as the solution continues to get darker and darker as more and more wires break off and become suspended in the IPA.

4.4.2 Nanowire Dispersion

Nanowires suspended in IPA can be dispersed by placing a drop onto a desired substrate. While the IPA is evaporating wires continue to move in the drop; eventually the IPA evaporates leaving wires that are dispersed along the surface of the substrate. If the washing steps have been done sufficiently well, no residue will be visible when this is done on a glass microscope slide. Despite the small size of the wires, their dispersion, and location on a substrate can be viewed by under an optical microscope. In this way wires dispersed on a patterned substrate can be identified as potentially useful before entering the SEM. Furthermore, knowing what part of the substrate is of interest helps in positioning the substrate appropriately. If wires are dispersed onto a patterned substrate, a special nanomanipulator setup designed by Brian Schwartentruber (at Sandia's Center for Integrated Nanotechnology (CINT) in Albuquerque, New Mexico) can be used to make contacts. This method works well for thick wires (diameter > 200nm), but not for thin wires (diameter < 100nm). Nevertheless, the next sections will describe this special setup, and how it *can* be used intelligently to measure individual wires.

4.4.3 Nanomanipulator

The nanomanipulator consists of a sample stage as well as two probes that go inside an SEM. Each probe, as well as the stage are independently controlled. The stage can be rotated clockwise or counter-clockwise by a slip-disc motor. The slip disc motor works by turning in one direction and then recoils to its original position. As it moves forward a second piece moves with it; as it recoils back the second piece does not, because it has enough forward momentum to overcome the friction. These types of motors result in inconsistent (in magnitude) jerky movements which will not work for very small movements (since not enough momentum is imparted to overcome friction). Furthermore, when trying to move away from something in close proximity, there is a chance of hitting that object during the recoil. The stage can also be moved in the z-axis direction, which is perpendicular to the plane of rotation using a similar set of motors.

The left probe (Probe-1) and right probe (Probe-2) are made of electropolished tungsten wire, and are moved by a similar set of slip disc motors to those of the stage. Probe-1 can

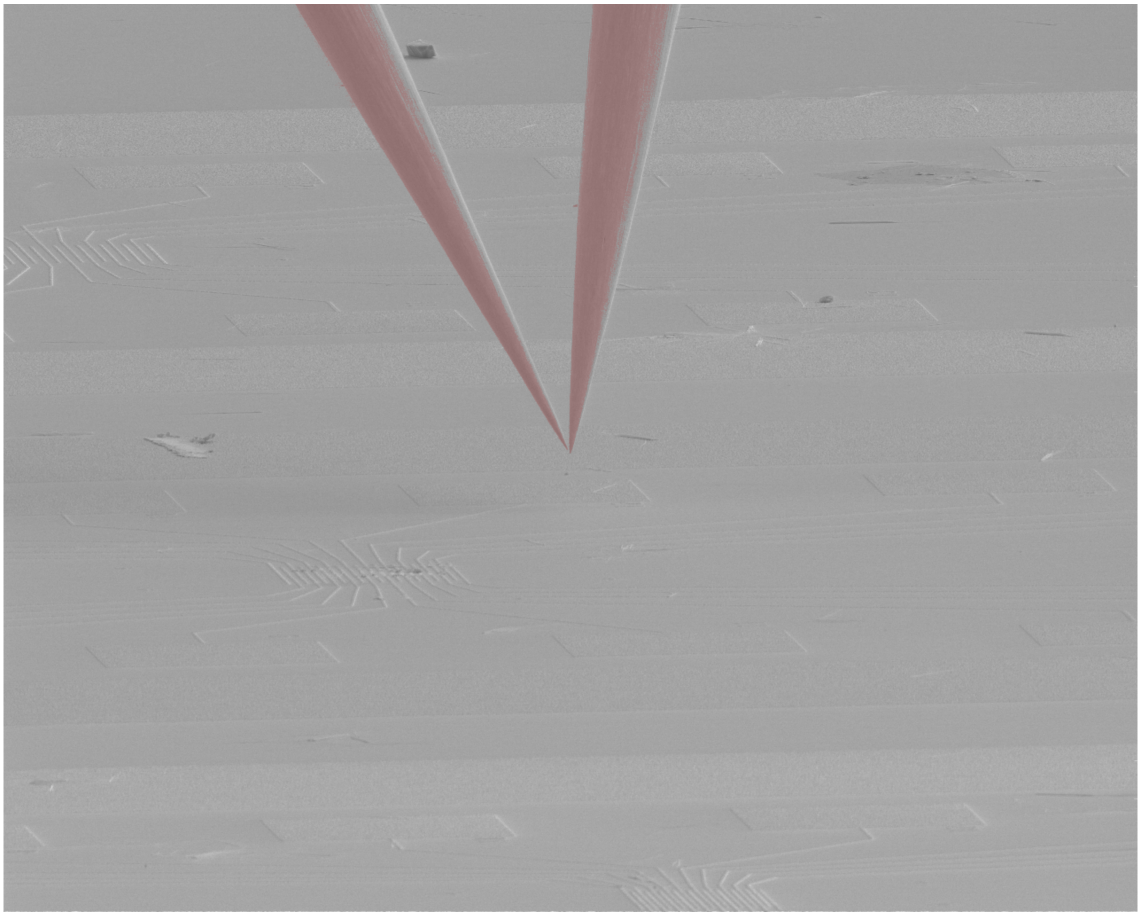

Figure 4.10: SEM image of nanomanipulator probes (falsely colored red) above the sample stage

move along the z-axis, as well as the x-axis (which is generally viewed as left/right on the screen); however, Probe-1 is unable to move along the y-axis (genarally in/out on the screen). Probe-2 has 3-degrees of freedom and can move along the x-axis, y-axis, and z-axis. Unlike the stage, the probes also have piezoelectric motors which allow for small movement. These motors have the added benefit of moving smoothly, without recoil, since they do not use a slip-disc; however, their range is very limited, so they are only useful once the probes are well positioned by using the slip-disc motors. Finally, the probes are put under a slight bias which can be controlled for doing crude resistance measurements. This bias is also useful for confirming that spot welding has been successful, as explained in section 4.4.

4.4.4 Contacting Wires by Spot welding

For large nanowires, a spot welding technique can be used to make contacts. This spot welding will be described below; however, as will also be discussed, a new method needed to be developed for our very thin wires.

If we want to take measurements on a wire, a drop of suspended wires is placed on a substrate with many leads pre-patterned on it (figure 4.11a). The pattern is made by using a mask and exposing photoresist, and then sputtering a conductive layer of platinum followed by a second conductive material with a low melting point.

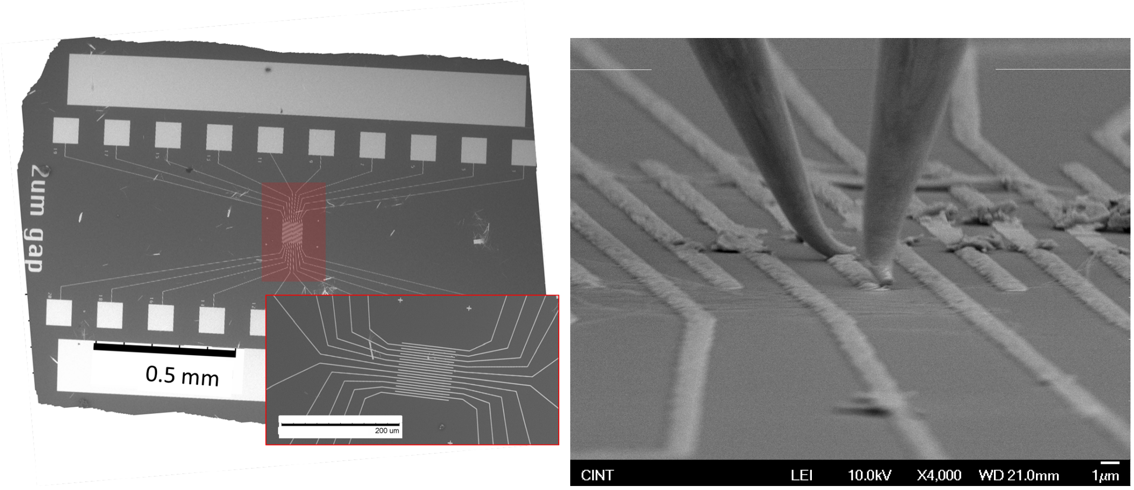

(a) SEM of metal pattern for contacting single nanowires

(b) SEM image of an attempted spot weldinging of a single wire which can be seen just in front of the right probe

Figure 4.11

The disperesed wires will be randomly distributed, but the large number of leads means that for any pattern, many wires will fall across multiple leads.

Contacts are made by bringing one probe into contact with only the wire, while the other lead is contacting the lead somewhere nearby. A current is passed between the probes, which causes the wire to heat up. This in turn causes the material (indium for example) around the wire to heat up and melt. A quick electrical pulse of this nature will spot weld the wire into the indium, creating a good electrical contact. This is done for every point of contact; success at spot welding can be confirmed by placing the probes on two different leads to which the wire has been spot welded, if an open circuit is observed, the contacting on at least one end was unsuccessful. If instead a closed circuit is observed, the contacting was successful on both ends.

When doing the spot welding, it is crucial to have the probe that is on the wire touching the wire and nothing else. If the probe touches the indium, heating will occur in a large portion of the patterned lead and cause the indium to ball up. This will not create a contact to the wire, and will likely make subsequent attempts at touching the probe to just the wire more difficult.

The nanowires that we have grown are purposefully quite small in diameter, and in fact the probe tips are relatively massive in comparison. Couple the relatively large size of the probes with the skill required to move the probes (and their limited range of motion) and you begin to create a very difficult task. To further complicate matters, the material selected for the leads is often times not a flat film, but has a very rough surface on these length scales (figure 4.11b).

Using this method, a bundle of clumped wires (this is easier since the bundle is like a thicker wire) were spot welded; however, this method failed when attempted with single wires (although many were seen in SEM correctly positioned to do so). This bundle happened to fall across a part of the pattern that was not intended for use, but which is just as functional (figure 4.12a).

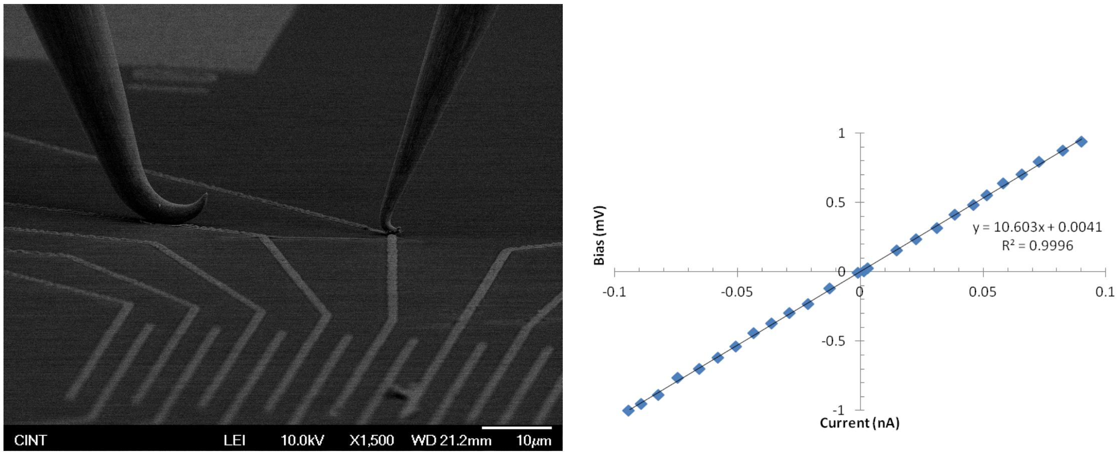

(a) SEM of probes being used to measure resistance of the wire bundle

(b) I-V data for wire bundle contacted using spot welding technique

Figure 4.12: The slope of the I-V curve gives a measured resistance of around 10kΩ, including contact resistance

It was confirmed that the spot welding was successful by touching the probe tips to the metal leads and measuring the current as the bias between the probes was changed. The linearity of the I-V curve, and that it goes through zero support that an ohmic 2-point contact was made across the wire bundle (figure 4.12b). Unfortunately further measurements were not taken as the bundle broke during preparation for resistance measurements at different temperatures (figure 4.13). Based on this I-V data, a resistance of 10.6 kΩ was measured for this 17.5μm bundle.

This resistance corresponds to a bundle of 12 wires which span from the unbroken end to the broken end (figure 4.13), each with a diameter between $50 - 60nm$. Assuming an average wire radius of $27.5nm$, and a length of 17.5μm, and a measured resistance of 10.6kΩ, a resistivity of 1.73x$10^{-5}\Omega$-m; the bulk resistivity value for bismuth telluride at 293 Kelvin is 1.403x$10^{-5}\Omega$-m[90] along the planes, and 3.785x$10^{-5}\Omega$-m[90] between the planes. Considering that contact resistance is not accounted for, these values match quite well with good values for bulk crystalline bismuth telluride. We hypothesize that at these diameters, the thermal conductivity will drop without altering the electrical properties; seeing bulk-like electrical conductivity is the first step in confirming this, as well as for determing the ZT of our wires.

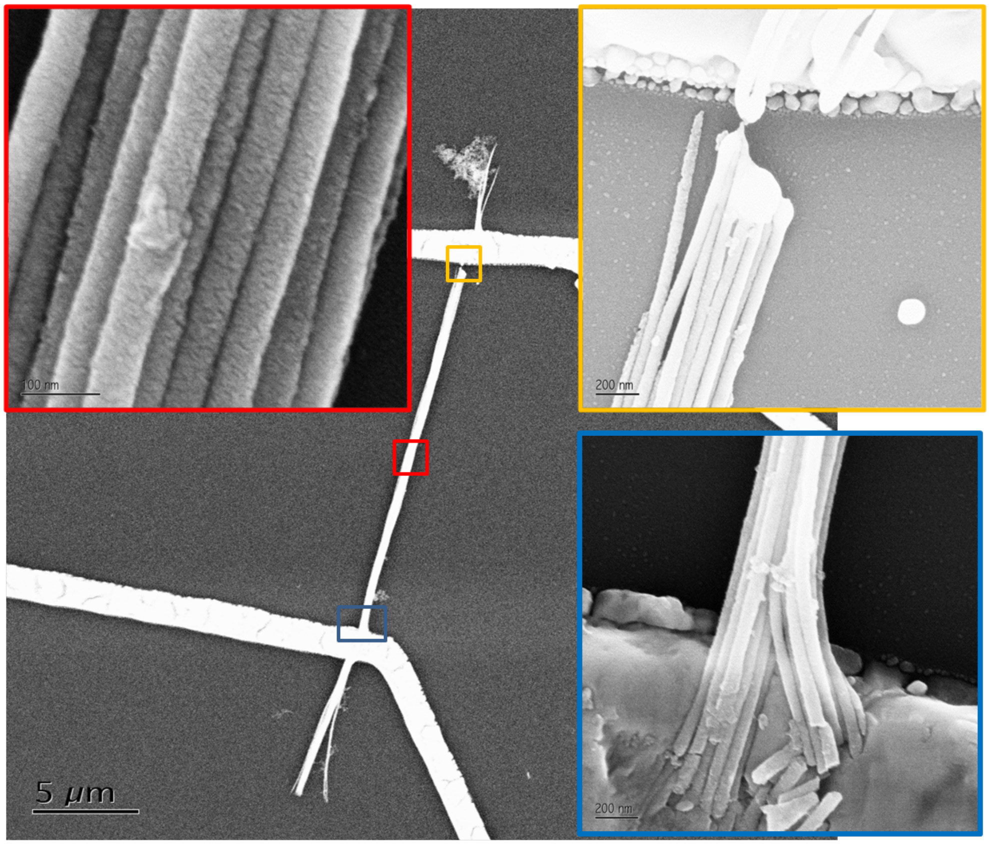

Figure 4.13: SEMs showing the fracture point for a spot welded bundle. Also the size and number of wires is easily discerned

Although this method was arguably successful there are two issues which require addressing. First is the difficulty of spot welding a single wire (verus a bundle), and the second is the difficulty of getting measurements for which the wire needs to be in a particular part of the metal pattern.

4.4.5 Moving Wires for Contacting

In order to measure the Seebeck coefficient, a more complicated patter, which incorporates a heater, is needed; this heater pattern also requires very specific placement of a wire. The wire must be placed so that it spans all four leads without laying on the heater, as shown in figure 4.14b.

Whereas in the prior case, a random dispersion of wires was sufficient, it is improbable that any single wire would arrange itself in the specific orientation and position desired. To get around this problem a different sample preparation is required. The wires are first dispersed somewhere off of the substrate (i.e. a TEM grid). Next, a single wire is located

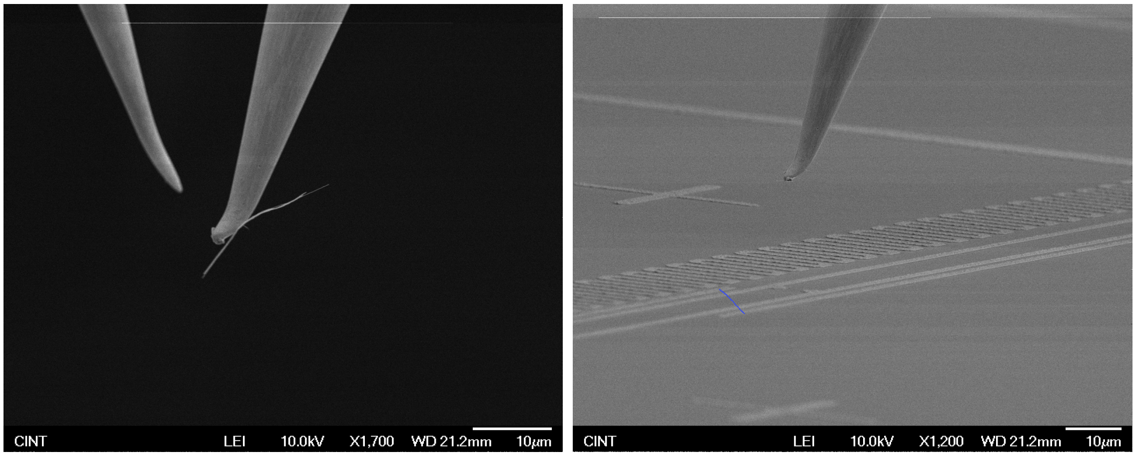

(a) A bundle of wires picked up with a probe

(b) SEM image the heating element pattern, with a cartoon of a correctly positioned wire added in blue

Figure 4.14

and picked up using one or both probes (fig 4.14a). The stage is then lowered and rotated so the probes are now above a patterned substrate. The stage is raised close to the probes, and then the probes are used to place the wire in the desired place and orientation. There is only a very small part of the pattern where all four leads are found, and so the wire must fall within this 10 μm zone. This zone can be seen in figure 4.14b, a cartoon of a wire in one such position. Although straightforward in theory, this is a very demanding set of tasks. At this point you can now begin spot welding the wire onto the pattern as explained in section 4.4.4.

As should be clear by now, the skill and luck required for comprehensive measurements done in this way is beyond expectation, let alone if such a method were used to anaylze many samples of wires to study slight changes in composition, crystallinity, orientation, etc. Luckily we have developed a new and better method for measurements.

4.4.6 Novel Method for Single Wire Contacts

The methods so far described deviate from the traditional method for single wire measurements. In this approach most of the pattern except for the leads is made by sputtering metal on a patterned substrate, the wires are then dispersed, and a second photoresist/exposure/sputter sequence is performed where just the leads are patterned on. When wires are dispersed on top of metal contacts they will adhere due to van der waals forces, but they do not form an ohmic electrical contact with the pattern; on the other hand when metal is sputtered on top of the wires, the metal-wire interface is quite conductive. The two patterning steps are separated to avoid shorting by a vagrant wire that spans some leads that should not be connected. However, in order to prevent this wire, one is put in the same situation presented in section 4.4.5; A single wire must fall in the correct orientation and position, with the added caveat that and nearby wires must not end up in such a way that the short any of the contact leads themselves.

Although the nanomanipulator was not designed as a bulldozer, it can advertantly (and often inadvertently) break wires. Dispersing wires first, patterning our full pattern (which can be aligned for any wire), and then decimating any wires that could potentially cause a short allows for a novel straightforward and reproducible way to make contact to a nanowire! Figure 4.4.7LABEL CHANGE, shows how interfering wires can be removed from the circuit by cutting with a probe tip. Furthermore, the efficacy of this method is seen in measurements taken before and after the errant wire has been cut (figure 4.15).

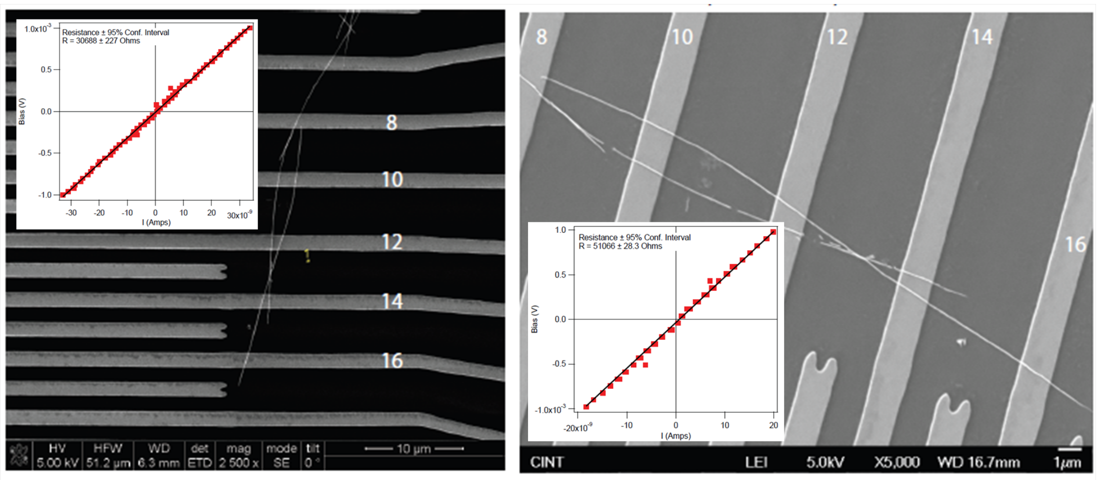

Figure 4.15: SEMs of a device before and after cutting of a nanowire with the nanomanipulator probes. The remaining fragments of the wire can be seen in the second image. Insets are of 4-point electrical conductivity measurements taken between the leads labeled 10 and 16. Despite appearances, the nickel layer is on top of the wires anywhere that they intersect.

Ignoring the differences in length we can treat this system as a series of two pairs of parrallel resistors, of equal resistance, with a third resistor in series. The resistance for such a system would be

$$R_{total,uncut} = 2 * \frac{1}{\frac{1}{R} + \frac{1}{R}} + R = \frac{2 * R}{2} + R = 2 * R \tag{4.3}$$

Once cut, the system is now just three similar resistors in series

$$R_{total,cut} = 3 * R = \frac{3}{2} * R_{total,uncut} \tag{4.4}$$

This matches well with the measured values, as $R_{total,cut} = \frac{3.3}{2} * R_{total,uncut}$. There is a 10% discrepancy between this very simplified estimation, and the experimentally determined values. This discrepancy is likely due to a combination of factors; the non-uniform length for each segment and the differences in contact resistance. Although contact resistance is taken into account for these 4-point measurements, difference in specific contact resistance between the wires and nickel at each lead is not; even the fact that the angle of the wire makes it have a larger surface in contact with the nickel than the cut wire, would produce a deviation from this highly simplified circuit model. Even so, these measurements confirm that this method can be used to take measurements on a specifically targeted nanowire, irrespective of nearby wires that could potentially short the circuit.

4.4.7 Bismuth Telluride

The wires studied in section 4.4.6 were from arrays of bismuth telluride. As shown in figure 1.9, bismuth telluride is highly anisotropic; the conductivity of bismuth telluride is higher along the planes, and lower between the planes. For a crystalline sample the in plane resistivity at room temperature is $R_{xy} = 1.403*10^{-5}\Omega$ m[90], and the cross plane resistivity at room temperature is $R_z = 3.785*10^{-5}\Omega$ m[90].

If the wires used to take measurements in section 4.4.6 are looked at under SEM, their diameter and segment lengths can be calculated. 4-pt measurements from different segments of this bismuth telluride wire gave resistivities of $1.37*10^{-5}$ and $1.47*10^{-5}$. This resistivity is right around that of pure tellurium, exactly what we would hope for for wires of this size ($\sim$60nm).

This contact method showed that from a collection of randomly dispersed wires, a pattern can be positioned around a chosen wire, and all other wires can be removed. The measurements described are limited to electrical conductivity; at these diameters, electrical properties should be comparable to those of bulk, with thermal properties showing a notable change. In particular, thermal conductivity for wires below the phonon mean free path ($\sim$ 100nm[97]) should drop significantly.

Bismuth telluride in bulk has an anisotropic thermal conductivity. For a room temperature, bulk sample, the in plane thermal conductivity gets as low as $\sim 1.8\frac{W}{m-K}$, while between the planes this can be as low as $\sim 0.75\frac{W}{m-K}$[34, 35, 36]. For ball-milled samples which, to date, have the highest ZT for bismuth telluride based materials, the thermal conductivity is at minimum $1.0\frac{W}{m-K}$[77, 105, 62].

Thermal conductivity measurements were taken on individual bismuth telluride wires using a pattern similar to the one shown in figure 4.14, but with the leads spaced further apart. As expected a relatively low thermal conductivity was observed, down to below $1.0\frac{W}{m-K}$. It is encouraging that a seemingly highly crystalline sample, with electrical conductivity matching bulk for an ideal geometry, would also have a thermal conductivity matching that of the least thermally conductive bismuth telluride samples. This information is not enough to make any claims on potential performance, however, as the Seebeck coefficient has yet to be measured due PPMS down time. Nevertheless, the thermal and electrical conductivities are as we would hope.

4.5 Conclusions

Measurements were attempted on whole arrays, sparse arrays, and single nanowires. Contacting to nanowires embedded in alumina continues to prove difficult; measured resistance values for whole arrays are often orders of magnitude higher than expected, and unreliability between different preparations of the same sample persist. Sparse arrays proved equally difficult to measure, though the reason for an inability to take measurements is still unclear.

Despite these problems, much was gained from each of these approaches. Inconsistent measurements on whole arrays of antimony doped tellurium were, nonetheless, consistent in their n-type character; this n-type assignment helped support prior characterization by CV and XRD. Failure to take measurements on wires in sparse arrays was only possible expanding this method to depositions in DMSO. This opens up the possibility for electrodeposition of sparse arrays of other compounds, from DMSO or even other non-aqueous solvents. It seems likely that with further study, measurements can be taken on these sparse arrays, as was done for sparse arrays grown from aqueous solutions.

Finally, a new, straightforward method for contacting and measuring properties of single nanowires has been developed. This method has been applied to measure promising electrical conductivity and thermal conductivity measurements for bismuth telluride nanowires. Further study of bismuth telluride will continue in the near term, in order to determine temperature dependence of all three key thermoelectric properties (electrical conductivity, thermal conductivity, and Seebeck coefficient) for these bismuth telluride wires, as well as wire of varying diameter. Likewise, this new method is not material specific, and so it will be used to analyze nanowires of other thermoelectrics, including (though not limited to) tellurium, antimony doped tellurium, bismuth antimony and lead telluride.

Chapter 5

Conclusion

One dimensional nanowires of good bulk thermoelectrics are predicted to show unprecedented performance. Electrodeposition into porous anodic alumina is an attractive method for growing nanowire arrays. This method is cheap and scalable, and the wires that are grown are electrically insulated. Bulk tellurium, when optimally doped with antimony, can achieve a quite respectable ZT of up to 0.5. Growing nanowires of tellurium has previously been achieved in aqueous solutions, but doping has been precluded by the formation of binary compounds such as antimony telluride. Electrodeposition in non-aqueous solvents is an under utilized technique; in the case of tellurium, it can afford benefits which are otherwise unattainable in water. By substituting DMSO as the solvent, antimony can be interstitially added into tellurium. By controlling solution concentrations and potential profiles, the antimony doping concentration can be adjusted. It was found that doping levels which exceeded limits found by other methods could even be achieved.

Electrodeposition of these antimony doped tellurium nanowires required a strong understanding of antimony-tellurium system. Antimony has previously been studied, for electrodeposition of bismuth-antimony, and was found to resemble its analog in aqueous solutions. Tellurium on the other hand was found to act quite differently from aqueous solutions. The odd and unique features of cyclic voltammograms of tellurium in DMSO were investigated until each could be identified; both the electrochemical reaction and an explanation of its shape and appearance. Furthermore, the binary system of antimony and tellurium together in DMSO was studied, and the concentration dependencies for each reductive peak was determined. This information proved invaluable towards the aforementioned growth of antimony doped tellurium nanowire arrays.

Once grown, nanowire arrays of doped and undoped tellurium were studied, and found to have ZT as high as 0.092. Low ZT values are linked to poor and unreliable contacting, evidenced by the differences in ZT measured on different preparations of the same sample. Further investigation into successful contacting methods are needed, not only for antimony doped tellurium arrays, but for all types of nanowires grown in porous alumina.

Another approach, for making property measurements on nanowires grown in porous alumina was to contact individual nanowires grown through a non-traditional method. This method used partially processed anodic alumina in order to limit nanowire growth. Sparse arrays grown in this way had previously been limited to acidic aqueous solutions, and based on the proposed mechanism this process would seemingly be limited to only these conditions. Moving to DMSO proved viable, however, and sparse arrays of tellurium, antimony doped tellurium, and bismuth antimony were all grown using DMSO as a solvent. The mechanism of this deposition still requires investigation, and it would be of interest to see if non-aqueous solvents besides DMSO could also be used. Apart from these investigations, further study is also needed to understand why measurements on these sparse arrays consistently generated only open circuits.

While measurements on wires embedded in alumina were not performed reliably, an innovative method was developed for easier and more reliable measurements of single wires. This method was initially applied to nanowires of bismuth telluride, but in the near plans are to also measure the properties of undoped tellurium, antimony doped tellurium, bismuth antimony, and lead telluride nanowires. For bismuth telluride wires, it was found that electrical conductivity matched in plane bulk (the most conductive geometry) values. Thermal conductivity appeared to be lower than those for bulk, matching the thermal conductivity of ball-milled samples, and falling somewhere between bulk in plane and cross plane conductivities. A ZT has yet to be determined, as no Seebeck coefficient was measured. This measurement will be done once the appropriate equipment is back online.

It is possible to grow nanowires with even smaller diameters, using porous alumina that is anodized under slightly different conditions. Analysis of the diameter dependence of bismuth telluride and other materials remains to be investigated, but should show further enhancement of thermoelectric performance, via further decrease of thermal conductivity.

Bibliography

[1] Z. A. Adzhimuradov, E. Yu Banyulis, R. M. Idrisova, and N. G. Polikhronidi. Influence of antimony impurities on the lattice and properties of tellurium. *Izvestiya Vysshikh Uchebnykh Zavedenii, Fizika—Izvestiya Vysshikh Uchebnykh Zavedenii, Fizika—Soviet Physics Journal*, 9(9):ISSN 0021–3411—0038–5697, 1969.

[2] Mahmut Aksit, David P. Toledo, and Richard D. Robinson. Scalable nanomanufacturing of millimetre-length 2d naxcoo2 nanosheets. *J. Mater. Chem.*, 22:5936–5944, 2012.

[3] Larry R. Faulkner Allen J. Bard. *Electrochemical Methods - Fundamentals and Applcations*. John Wiley & Sons, Inc., 2001.

[4] Mohammad Asim Ansari and James A. Ibers. Soluble selenides and tellurides. *Coordination Chemistry Reviews*, 100(0):223 – 266, 1990.

[5] S. A. Awad. Electrochemical evidence for diatomicity of tellurium. *Journal of the Electrochemical Society*, 109(9):865–870, 1962.

[6] A. Bailini, F. Donati, M. Zamboni, V. Russo, M. Passoni, C. S. Casari, A. L. Bassi, and C. E. Bottani. Pulsed laser deposition of bi2te3 thermoelectric films. *Applied Surface Science*, 254(4):1249–1254, 2007. Symposium on Laser Synthesis and Processing of Advanced Materials held at the E-MRS 2007 Spring Meeting 2007 Strasbourg, FRANCE.

[7] T. Balasubramaniam, S. K. Narayandass, and D. Mangalaraj. Electrical properties of thermally evaporated tellurium thin films. *Bulletin of Materials Science*, 20(1):79–92, 1997.

[8] M. E. H. Bergmann and A. S. Koparal. Kinetic studies on electrochemical antimony removal from concentrated sulfuric acid systems. *Chemical Engineering & Technology*, 30(2):242–249, 2007.

[9] K. G. Biswas, T. D. Sands, B. A. Cola, and X. F. Xu. Thermal conductivity of bismuth telluride nanowire array-epoxy composite. *Applied Physics Letters*, 94(22), 2009.

[10] D. A. Borca-Tasciuc and G. Chen. Anisotropic thermal properties of nanochanneled alumina templates. *Journal of Applied Physics*, 97(8), 2005.

[11] D. A. Borca-Tasciuc, G. Chen, A. Prieto, M. S. Martin-Gonzalez, A. Stacy, T. Sands, M. A. Ryan, and J. P. Fleurial. Thermal properties of electrodeposited bismuth telluride nanowires embedded in amorphous alumina. *Applied Physics Letters*, 85:6001–6003, 2004.

[12] A. I. Boukai, Y. Bunimovich, J. Tahir-Kheli, J. K. Yu, W. A. Goddard, and J. R. Heath. Silicon nanowires as efficient thermoelectric materials. *Nature*, 451(7175):168–171, 2008.

[13] L. J. Brogan and A. M. Stacy. Sparse nanowire arrays for facile transport measurements. *Materials Letters*, 64(15):1674–1676, 2010.

[14] A. Brown and B. Lewis. Systems bismuth-tellurium and antimony-tellurium and synthesis of minerals hedleyite and wehrlite. *Journal of Physics and Chemistry of Solids*, 23(11):1597–&, 1962.

[15] T. Caillat, M. Carle, D. Perrin, H. Scherrer, and S. Scherrer. Study of the bi-sb-te ternary phase-diagram. *Journal of Physics and Chemistry of Solids*, 53(2):227–232, 1992.

[16] C. H. Cartwright and M. Haberfeld. Conductivity of tellurium. *Nature*, 134:287–288, 1934.

[17] E.A. Chavez-Urbiola, Yu.V. Vorobiev, and L.P. Bulat. Solar hybrid systems with thermoelectric generators. *Solar Energy*, 86(1):369 – 378, 2012.

[18] Gang Chen. Theoretical efficiency of solar thermoelectric energy generators. *JOURNAL OF APPLIED PHYSICS*, 109(10), MAY 15 2011.

[19] Y. Cheng, X. D. Han, X. Q. Liu, K. Zheng, Z. Zhang, T. Zhang, Z. T. Song, B. Liu, and S. L. Feng. Self-extrusion of te nanowire from si-sb-te thin films. *Applied Physics Letters*, 93(18), 2008.

[20] V. D. Das, N. Jayaprakash, and N. Soundararajan. Thermoelectric-power of tellurium thin-films and its thickness and temperature-dependence. *Journal of Materials Science*, 16(12):3331–3334, 1981.

[21] D. Del Frari, S. Diliberto, N. Stein, C. Boulanger, and J. M. Lecuire. Pulsed electrodeposition of (bi1-xsbx)(2)te-3 thermoelectric thin films. *Journal of Applied Electrochemistry*, 36(4):449–454, 2006.

[22] Doriane Del Frari, Sbastien Diliberto, Nicolas Stein, Clotilde Boulanger, and Jean-Marie Lecuire. Comparative study of the electrochemical preparation of bi2te3, sb2te3, and (bixsb1-x)2te3 films. *Thin Solid Films*, 483(1-2):44–49, 2005. doi: DOI: 10.1016/j.tsf.2004.12.015.

[23] D. W. Deng, P. Li, and Y. Q. Gu. Synthesis and structural analysis of angled te nanocrystals. *Crystal Research and Technology*, 44(6):629–635, 2009.

[24] S. Dennison and S. Webster. An electrochemical and optical microscopic study of the reduction of hteo2+ in aqueous acid solution. *Journal of Electroanalytical Chemistry and Interfacial Electrochemistry*, 314(1-2):207–222, 1991. doi: 10.1016/0022-0728(91)85438-U.

[25] Li Deyu, A. L. Prieto, Wu Yiying, M. S. Martin-Gonzalez, A. Stacy, T. Sands, R. Gronsky, Yang Peidong, and A. Majumdar. Measurements of bi/sub 2/te/sub 3/ nanowire thermal conductivity and seebeck coefficient. *Proceedings ICT'02. 21st International Conference on Thermoelectrics (Cat. No.02TH8657)*, pages 333–6—xiii+573, 2002. 21st International Conference on Thermoelectrics.

[26] M. S. Dresselhaus, G. Dresselhaus, X. Sun, Z. Zhang, S. B. Cronin, and T. Koga. Low-dimensional thermoelectric materials. *Physics of the Solid State*, 41(5):679–682, 1999.

[27] M. S. Dresselhaus, G. Dresselhaus, X. Sun, Z. Zhang, S. B. Cronin, T. Koga, J. Y. Ying, and G. Chen. The promise of low-dimensional thermoelectric materials. *Microscale Thermophysical Engineering*, 3(2):89–100, 1999.

[28] Z.H. Dughaish. Lead telluride as a thermoelectric material for thermoelectric power generation. *Physica B: Condensed Matter*, 322(12):205 – 223, 2002.

[29] S. Dutta, V. Shubha, T. G. Ramesh, and F. D'Sa. Thermal and electronic properties of bi1-xsbx alloys. *Journal of Alloys and Compounds*, 467(1-2):305–309, 2009.

[30] L. R. Faulkner. Understanding electrochemistry - some distinctive concepts. *Journal of Chemical Education*, 60(4):262–264, 1983.

[31] Wei Wang Feihui Li. Electrochemical reduction process of sb(iii) on au substrate. Department of Applied Chemistry, School of Chemical Engineering and Technology, Tianjin University, 2007.

[32] R. C. Furneaux, W. R. Rigby, and A. P. Davidson. The formation of controlled-porosity membranes from anodically oxidized aluminum. *Nature*, 337(6203):147–149, 1989.

[33] G. Ghosh, H. L. Lukas, and L. Delaey. A thermodynamic assessment of the sb-te system. *Zeitschrift Fur Metallkunde*, 80(10):731–736, 1989.

[34] H. J. Goldsmid. The thermal conductivity of bismuth telluride. *Proceedings of the Physical Society of London Section B*, 69(2):203–209, 1956. Times Cited: 44.

[35] H. J. Goldsmid. The thermal conductivity of bismuth telluride. *Report of the Meeting on Semiconductors—Report of the Meeting on Semiconductors*, pages 127–131—153, 1957. Times Cited: 0 Meeting on Semiconductors Rugby UK.

[36] H. J. Goldsmid. Heat conduction in bismuth telluride. *Proceedings of the Physical Society of London*, 72(463):17–26, 1958. Times Cited: 41.

[37] P. Grosse. Die festkiirpereigenschaften von tellur. In *Die Festkiirpereigenschaften von Tellur*, volume 48 of *Springer Tracts in Modern Physics*, pages 1–204. Springer Berlin / Heidelberg, 1969.

[38] R. Haakenaasen, E. Selvig, S. Foss, L. Trosdahl-Iversen, and J. Tafto. Segmented nanowires of hgte and te grown by molecular beam epitaxy. *Applied Physics Letters*, 92(13), 2008.

[39] J. Ham, W. Shim, D. H. Kim, S. Lee, J. Roh, S. W. Sohn, K. H. Oh, P. W. Voorhees, and W. Lee. Direct growth of compound semiconductor nanowires by on-film formation of nanowires: Bismuth telluride. *Nano Letters*, 9(8):2867–2872, 2009.

[40] T. C. Harman. Special techniques for measurement of thermoelectric properties. *Journal of Applied Physics*, 29(9):1373–1374, 1958.

[41] P. Heo, K. Hagiwara, R. Ichino, and M. Okido. Electrodeposition and thermoelectric characterization of bi2te3. *Journal of the Electrochemical Society*, 153(4):C213–C217, 2006.

[42] J. Heremans and C. M. Thrush. Thermoelectric power of bismuth nanowires. *Physical Review B*, 59(19):12579–12583, 1999.

[43] L. D. Hicks and M. S. Dresselhaus. The effect of quantum well structures on the thermoelectric figure of merit. *Semiconductor Heterostructures for Photonic and Electronic Applications Symposium—Semiconductor Heterostructures for Photonic and Electronic Applications Symposium*, pages 821–6—xvii+836, 1993. Semiconductor Heterostructures for Photonic and Electronic Applications Symposium.

[44] L. D. Hicks and M. S. Dresselhaus. Effect of quantum-well structures on the thermoelectric figure of merit. *Physical Review B*, 47(19):12727–12731, 1993.

[45] L. D. Hicks and M. S. Dresselhaus. Thermoelectric figure of merit of a one-dimensional conductor. *Physical Review B*, 47(24):16631–16634, 1993.

[46] A. I. Hochbaum, R. K. Chen, R. D. Delgado, W. J. Liang, E. C. Garnett, M. Najarian, A. Majumdar, and P. D. Yang. Enhanced thermoelectric performance of rough silicon nanowires. *Nature*, 451(7175):163–U5, 2008.

[47] Allon I. Hochbaum and Peidong Yang. Semiconductor nanowires for energy conversion. *Chemical Reviews*, 110(1):527–546, 2010. PMID: 19817361.

[48] Lim Jae-Hong, Park Mi Yeong, Lim Dong Chan, Yoo Bongyoung, Lee Jung-Ho, N. V. Myung, and Lee Kyu Hwan. Electrodeposition of p-type sbxtey thermoelectric films. *Journal of Electronic Materials*, 40(5):1321–1325, May 2011.

[49] C. G. Jin, X. Q. Xiang, C. Jia, W. F. Liu, W. L. Cai, L. Z. Yao, and X. G. Li. Electrochemical fabrication of large-area, ordered bi2te3 nanowire arrays. *Journal of Physical Chemistry B*, 108(6):1844–1847, 2004.

[50] G. Joshi, H. Lee, Y. C. Lan, X. W. Wang, G. H. Zhu, D. Z. Wang, R. W. Gould, D. C. Cuff, M. Y. Tang, M. S. Dresselhaus, G. Chen, and Z. F. Ren. Enhanced thermoelectric figure-of-merit in nanostructured p-type silicon germanium bulk alloys. *Nano Letters*, 8(12):4670–4674, 2008.

[51] J. Keyani, A. M. Stacy, and J. Sharp. Assembly and measurement of a hybrid nanowire-bulk thermoelectric device. *Applied Physics Letters*, 89(23), 2006.

[52] Jenny Keyani. *Electrodeposition and Device Incorporation of Bismuth Antimony Nanowire Arrays*. PhD thesis, UC Berkeley, Berkeley, Spring 2007 2007.

[53] M. Y. Kim, K. W. Park, and T. S. Oh. Thermoelectric characteristics of the sb2te3 compound semiconductor electrodeposited for nanowire applications. *Journal of the Korean Physical Society*, 53(1):266–270, 2008. 13th International Conference on II-VI Compounds.

[54] Charles Kittel. *Introduction to solid state physics*. Wiley, Hoboken, NJ, 8th edition, 2005. 2004042250 Charles Kittel. ill. ; 25 cm. "Chapter 18, Nanostructures, was written by Professor Paul McEuen ..." Includes bibliographical references and index.

[55] F. Klaiber, W. Petter, and F. Hulliger. The structure type of re2te5, a new [m6x14] cluster compound. *Journal of Solid State Chemistry*, 46(1):112 – 120, 1983.

[56] Jeremy Cuellar Klitzke. *Electrodeposition of Cobalt-Antimony Films and Nanowires from Aqueous Electrolytes*. PhD thesis, University of California Berkeley, Berkeley, Spring 2009 2009.

[57] D. Kraemer, L. Hu, A. Muto, X. Chen, G. Chen, and M. Chiesa. Photovoltaic-thermoelectric hybrid systems: A general optimization methodology. *APPLIED PHYSICS LETTERS*, 92(24), JUN 16 2008.

[58] Y. F. Li, B. Yao, Y. M. Lu, C. X. Cong, Z. Z. Zhang, Y. Q. Gai, C. J. Zheng, B. H. Li, Z. P. Wei, D. Z. Shen, X. W. Fan, L. Xiao, S. C. Xu, and Y. Liu. Characterization of biaxial stress and its effect on optical properties of zno thin films. *Applied Physics Letters*, 91(2):–, Jul 9 2007. 189VS Times Cited:26 Cited References Count:12.

[59] Cai ling Xu, Li Zhang, Hao li Zhang, and Hu lin Li. Well dispersed gold nanowire suspension for assembly application. *Applied Surface Science*, 252(4):1182 – 1186, 2005.

[60] D. W. Liu and J. F. Li. Electrocrystallization process during deposition of bi-te films. *Journal of the Electrochemical Society*, 155(7):D493–D498, 2008.

[61] W. F. Liu, W. L. Cai, and L. Z. Yao. Electrochemical deposition of well-ordered single-crystal pbte nanowire arrays. *Chemistry Letters*, 36:1362–1363, 2007.

[62] Yi Ma, Qing Hao, Bed Poudel, Yucheng Lan, Bo Yu, Dezhi Wang, Gang Chen, and Zhifeng Ren. Enhanced thermoelectric figure-of-merit in p-type nanostructured bismuth antimony tellurium alloys made from elemental chunks. *NANO LETTERS*, 8(8):2580–2584, AUG 2008.

[63] P. Magri, C. Boulanger, and J. M. Lecuire. Synthesis, properties and performances of electrodeposited bismuth telluride films. *Journal of Materials Chemistry*, 6(5):773–779, 1996.

[64] R. S. Makala, K. Jagannadham, and B. C. Sales. Pulsed laser deposition of bi2te3-based thermoelectric thin films. *Journal of Applied Physics*, 94(6):3907–3918, 2003.

[65] M. Martin-Gonzalez, A. L. Prieto, R. Gronsky, T. Sands, and A. M. Stacy. Insights into the electrodeposition of bi2te3. *Journal of the Electrochemical Society*, 149:C546–C554, 2002.

[66] M. Martin-Gonzalez, A. L. Prieto, R. Gronsky, T. Sands, and A. M. Stacy. High-density 40 nm diameter sb-rich bi2-xsbxte3 nanowire arrays. *Advanced Materials*, 15(12):1003–+, 2003.

[67] M. Martin-Gonzalez, A. L. Prieto, M. S. Knox, R. Gronsky, T. Sands, and A. M. Stacy. Electrodeposition of bi1-xsbx films and 200-nm wire arrays from a nonaqueous solvent. *Chemistry of Materials*, 15:1676–1681, 2003.

[68] S. Michel, S. Diliberto, N. Stein, B. Bolle, and C. Boulanger. Characterisation of electroplated bi-2(te1-xsex)(3) alloys. *Journal of Solid State Electrochemistry*, 12(1):95–101, 2008.

[69] A. Miner. The compatibility of thin films and nanostructures in thermoelectric cooling systems. *Journal of Heat Transfer-Transactions of the Asme*, 129(7):805–812, 2007.

[70] R. S. Nicholson and Irving. Shain. Theory of stationary electrode polarography. single scan and cyclic methods applied to reversible, irreversible, and kinetic systems. *Analytical Chemistry*, 36(4):706–723, 1964.

[71] G.S. Nolas, J. Sharp, and H.J. Goldsmid. *Thermoelectrics: Basic Principles and New Materials Developments*. Springer, 2001.

[72] US Department of Energy. Us energy use in 2010: Contribution of major energy sources. Online, November 2011.

[73] Kanji Omura and Daniel Swern. Oxidation of alcohols by activated? dimethyl sulfoxide. a preparative, steric and mechanistic study. *Tetrahedron*, 34(11):1651 – 1660, 1978.

[74] R. Patschke and M. G. Kanatzidis. Polytelluride compounds containing distorted nets of tellurium. *Physical Chemistry Chemical Physics*, 4(14):3266–3281, 2002.

[75] N. Peranio, O. Eibl, and J. Nurnus. Structural and thermoelectric properties of epitaxially grown bi2te3 thin films and superlattices. *Journal of Applied Physics*, 100(11), 2006.

[76] N. G. Polikhronidi. Influence of antimony impurity on the high-temperature conductivity of tellurium. *Izvestiya Vysshikh Uchebnykh Zavedenii, Fizika Izvestiya Vysshikh Uchebnykh Zavedenii, Fizika Soviet Physics Journal*, 4(4):ISSN 0021–3411—0038–5697, 1978.

[77] B. Poudel, Q. Hao, Y. Ma, Y. C. Lan, A. Minnich, B. Yu, X. A. Yan, D. Z. Wang, A. Muto, D. Vashaee, X. Y. Chen, J. M. Liu, M. S. Dresselhaus, G. Chen, and Z. F. Ren. High-thermoelectric performance of nanostructured bismuth antimony telluride bulk alloys. *Science*, 320(5876):634–638, 2008.

[78] A. L. Prieto, M. Martin-Gonzalez, J. Keyani, R. Gronsky, T. Sands, and A. M. Stacy. The electrodeposition of high-density, ordered arrays of bi1-xsbx nanowires. *Journal of the American Chemical Society*, 125(9):2388–2389, 2003.

[79] O. Rabin, Lin Yu-Ming, S. B. Cronin, and M. S. Dresselhaus. Thermoelectric nanowires by electrochemical deposition. *Thermoelectric Materials 2001 - Research and Applications. Symposium (Materials Research Society Symposium Proceedings Vol.691)*, pages 257–62—xiv+467, 2001. Thermoelectric Materials 2001 - Research and Applications. Symposium Boston, MA USA.

[80] A. Rauf, F. J. Ahmad, and R. S. R. Murthy. Comparative evaluation of different techniques of taste masking and their release profile for a water-soluble bitter drug. *Journal of Pharmacy and Pharmacology*, 61:A3–A3, 2009.

[81] F. Z. Ren, Y. X. Wang, and G. B. Zhang. Pressure-induced phase transition of ruthenium diboride. *Chinese Physics Letters*, 26(1):–, Jan 2009. 400KI Times Cited:3 Cited References Count:21.

[82] Y. Rheem, C. H. Chang, C. M. Hangarter, D. Y. Park, K. H. Lee, Y. S. Jeong, and N. V. Myung. Synthesis of tellurium nanotubes by galvanic displacement. *Electrochimica Acta*, 55(7):2472–2476, 2010.

[83] M. Rusu. On thickness dependence of electrical and optical properties of te thin films. *Applied Physics a-Materials Science & Processing*, 66(3):357–361, 1998.

[84] M. S. Sander, R. Gronsky, T. Sands, and A. M. Stacy. Structure of bismuth telluride nanowire arrays fabricated by electrodeposition into porous anodic alumina templates. *Chemistry of Materials*, 15(1):335–339, 2003.

[85] S. A. Sapp, B. B. Lakshmi, and C. R. Martin. Template synthesis of bismuth telluride nanowires. *Advanced Materials*, 11(5):402–404, 1999.

[86] S. Sen, U. M. Bhatta, V. Kumar, K. P. Muthe, S. Bhattacharya, S. K. Gupta, and J. V. Yakhmi. Synthesis of tellurium nanostructures by physical vapor deposition and their growth mechanism. *Crystal Growth & Design*, 8(1):238–242, 2008.

[87] Jeff Sharp. Personal communication, 2009.

[88] G. Stan, S. Krylyuk, A. V. Davydov, M. Vaudin, L. A. Bendersky, and R. F. Cook. Surface effects on the elastic modulus of te nanowires. *Applied Physics Letters*, 92(24), 2008.

[89] N. G. Stoltz and G. J. Snyder. Effects of annealing electrodeposited bismuth telluride films. *Proceedings ICT'02. 21st International Conference on Thermoelectrics (Cat. No.02TH8657)*, pages 28–30—xiii+573, 2002.

[90] M. Stordeur and W. Khnberger. Nichtparabolizitt des valenzbandes von bi2te3 gefolgert aus transporteigenschaften. *physica status solidi (b)*, 69(2):377–387, 1975.

[91] Z. X. Su, G. Hahner, and W. Z. Zhou. Investigation of the pore formation in anodic aluminium oxide. *Journal of Materials Chemistry*, 18(47):5787–5795, 2008.

[92] Fukuroi Tadao, Tanuma Seiichi, and Tobisawa Shotaro. Electrical properties of antimony-doped tellurium crystals. *Science reports of the Research Institutes, Tohoku University. Ser. A, Physics, chemistry and metallurgy*, 4(

[93] M. T. Tang and M. S. Dresselhaus. A band structure phase diagram calculation of 2d bisb films. *Materials and Technologies for Direct Thermal-to-Electric Energy Conversion. Symposium (Materials Research Society Symposium Proceedings Vol.886)*, pages 129–34—xvi+512, 2006. Materials and Technologies for Direct Thermal-to-Electric Energy Conversion.

[94] G. E. Thompson and G. C. Wood. Porous anodic film formation on aluminum. *Nature*, 290(5803):230–232, 1981.

[95] L. Trahey, C. R. Becker, and A. M. Stacy. Electrodeposited bismuth telluride nanowire arrays with uniform growth fronts. *Nano Letters*, 7(8):2535–2539, 2007.

[96] V. I. Veraksa, V. N. Lange, and T. I. Lange. Effect of small additions of subgroup-v elements on some properties of tellurium monocrystals. *Zhurnal Fizicheskoi Khimii*, 37(10):2308–2310, 1963. Times Cited: 8.

[97] P. A. Walker. The thermal conductivity and thermoelectric power of bismuth telluride at low temperatures. *Proceedings of the Physical Society of London*, 76(487):113–126, 1960. Times Cited: 27.

[98] W. Wang, Q. H. Huang, F. L. Jia, and J. Zhu. Electrochemically assembled p-type bi2te3 nanowire arrays. *Journal of Applied Physics*, 96(1):615–618, 2004.

[99] C. J. Warren, R. C. Haushalter, and A. B. Bocarsly. Electrochemical synthesis of a pseudo-two-dimensional polytelluride containing te-12(2-) anions: Structure of [(c2h5)(4)n](2)te-12. *Journal of Alloys and Compounds*, 233(1-2):23–29, 1996.

[100] F. Xiao, C. Hangarter, B. Yoo, Y. Rheem, K. H. Lee, and N. V. Myung. Recent progress in electrodeposition of thermoelectric thin films and nanostructures. *Electrochimica Acta*, 53(28):8103–8117, 2008.

[101] H. Yan, N. Sada, and N. Toshima. Thermal transporting properties of electrically conductive polyaniline films as organic thermoelectric materials. *Journal of Thermal Analysis and Calorimetry*, 69(3):881–887, 2002. 2nd International Symposium on the New Frontiers of Thermal Studies of Materials.

[102] L. Q. Yang, X. L. Ren, F. Q. Tang, and L. Zhang. A practical glucose biosensor based on fe3o4 nanoparticles and chitosan/nafion composite film. *Biosensors & Bioelectronics*, 25(4):889–895, Dec 15 2009. 528JI Times Cited:9 Cited References Count:43.

[103] J. Yao, T. Zhang, J. H. Ren, M. X. Yu, and G. G. Wu. Effect of cd133/prominin-1 antisense oligodeoxynucleotide on in vitro growth characteristics of huh-7 human hepatocarcinoma cells and u251 human glioma cells. *Oncology Reports*, 22(4):781–787, Oct 2009. 493VO Times Cited:4 Cited References Count:19.

[104] B. Y. Yoo, C. K. Huang, J. R. Lim, J. Herman, M. A. Ryan, J. P. Fleurial, and N. V. Myung. Electrochemically deposited thermoelectric n-type bi2te3 thin films. *Electrochimica Acta*, 50(22):4371–4377, 2005.

[105] B. Yu, Q. Y. Zhang, H. Wang, X. W. Wang, H. Z. Wang, D. Z. Wang, G. J. Snyder, G. Chen, and Z. F. Ren. Thermoelectric property studies on thallium-doped lead telluride prepared by ball milling and hot pressing. *Journal of Applied Physics*, 108(1), 2010. Times Cited: 0.

[106] H. Yu, P. C. Gibbons, and W. E. Buhro. Bismuth, tellurium, and bismuth telluride nanowires. *Journal of Materials Chemistry*, 14(4):595–602, 2004.

[107] Genqiang Zhang, Benjamin Kirk, Luis A. Jauregui, Haoran Yang, Xianfan Xu, Yong P. Chen, and Yue Wu. Rational synthesis of ultrathin n-type bi2te3 nanowires with enhanced thermoelectric properties. *Nano Letters*, 12(1):56–60, 2012.

[108] A. Zhao, L. Zhang, Y. Pang, and C. Ye. Ordered tellurium nanowire arrays and their optical properties. *Applied Physics a-Materials Science & Processing*, 80(8):1725–1728, 2005.

[109] A. W. Zhao, C. H. Ye, G. W. Meng, L. D. Zhang, and P. M. Ajayan. Tellurium nanowire arrays synthesized by electrochemical and electrophoretic deposition. *Journal of Materials Research*, 18(10):2318–2322, 2003.